PHYSICS OF LUMINESCENCE NANOMATERIALS

by

BOON KUAN WOO

Presented to the Faculty of the Graduate School of

The University of Texas at Arlington in Partial Fulfillment

of the Requirements

for the Degree of

DOCTOR OF PHILOSOPHY

THE UNIVERSITY OF TEXAS AT ARLINGTON

DECEMBER 2010

“All changes must correspond to inner truth.”

Revolution Hexagram, I-Ching

ACKNOWLEDGEMENTS

I would like to thank Dr. Chen Wei for being my supervisor and also to my committee members, Dr. Yang Jian, Dr. Yaowu Hao, Dr. Liu Ping and Dr. Alex Weiss for their useful guidance and comments. I would also like to extend my grateful thanks to my collaborators, Dr. Zhiping Luo, Dr. Yang Li, Dr. Surinder P. Singh and Dr. Alan Joly for their kind advices and assistance in helping me in navigating the journal publications' obstacles. I would like to thank and acknowledge the contributions and supports from my colleagues, Yao Mingzhen, Lun Ma, Zhang Xing, Yuebin Li and Dr. Marius Hossu (X-ray PL measurements). I also would like to thank Dr. Jiechao Jiang and Dr. David from UTA Characterization Center for Materials and Biology for their technical supports. I would like to express my gratitude to Dr. Zhang Qiming for giving me the research opportunity here at UT-Arlington and also to Dr. Asok K. Ray for being my mathematics instructor.

Many heartful thanks too to William Sospropartono and Anton Chong for their camera photography supports. I cherished the treasure times that I enjoyed spending in 2009 with Jose Barona, Hande Demirkiran, Kok Leong Ng and Jack Teoh. They really helped to cheer me up and to boost my research morals. Special thanks should also go to Margie, Frances, Stacey, Bethany, Victor and Doug for all their supports. Many thanks too, go to all my friends for their encouragements.

Finally, I would like to thank my family, my mother, my sisters, my brother and my uncle for their moral supports and patience. I really miss them very much!

December 3, 2010

ABSTRACT

PHYSICS OF LUMINESCENCE NANOMATERIALS

by

Boon Kuan Woo

Luminescence oxide nanoparticles have tremendous potential in revolutionizing many interesting applications in today's emerging cutting-edge optical technology such as solid state lighting, biomedical labeling, imaging, photodynamic activation and radiation detection. In the early parts of this thesis, we synthesized two types of luminescence oxide nanoparticles, namely zinc oxide and gadolinium oxide in the hope of investigating their optical properties and to gain a deeper understanding in determining the relationship in between the ZnO's surface defect emission and its excitonic emission. We also investigated the luminescence properties of rare-earth dopants such as Ce^{3+} and Eu^{3+} doped into the host gadolinium oxide nanoparticles, in the hope of utilizing them as multi-color phosphor for radiation detection with fast response time, high energy resolution and sensitivity.

Fluorescence and phosphorescence or persistent luminescences are two fascinating optical phenomena that have attracted the attention of many optical scientists and material researchers world-wide. The most puzzling of them all, the persistent luminescence phenomena remains a mystery unsolved since the mechanism to explain them remain unclear. Of so many vast research publications available on persistent luminescence materials, little attention has been given to the role of the host phosphor material.

In the later parts of this thesis, we studied deeply the roles of luminescence oxide nanoparticles such as ZnO nanoparticles in preparing luminescence material or long afterglow phosphor material. The host phosphor chosen in our study is $CaZnGe_2O_6$, in which

we measured their optical properties under UV and X-ray illuminations. Our extensive investigations cover a wide variety of dopants from rare-earth elements, transition metals and cations from group IIA, IIIA and VA. A whole myriad of interesting optical observations have been uncovered ranging from UVA, visible light and infra-red emission as we seek to uncover the deepest truth about the electrons migration between the host phosphor and the dopants' luminescence centers that have been elusively hidden and guarded by the internal lattice structure of this phosphor material.

TABLE OF CONTENTS

LIST OF FIGURES

Figure Page

CHAPTER 1

FLUORESCENCE AND PERSISTENT LUMINESCENCE

It has been over 800 years since the second emperor of Song Dynasty (960-1279 A.D), Tai Zong asked his ministers to explain on the phosphorescent effect observed on his luminescence painting. Since then, mankind has studied phosphorescence materials in order to uncover its secrets. The ancient Chinese and Japanese, both have the oldest historical records on phosphorescence materials that dated over 2000 years while the Europeans have their well-documented history of persistent luminescence materials that dated back to early 17^{th} century.

Beginning in the 1980s, mankind has entered the age of nanotechnology with the introduction of fullerenes, carbon nanotubes and quantum dots semiconductor. As nanotechnology marches on, its impacts are felt everywhere, contributing to application in electronics, energy, automobiles, domestic appliances, sports and toys, cosmetics, biotechnology and medical field.

This dissertation is about mankind's efforts and endeavors to tame, wrestle down and unlock the host phosphor material's secrets, in order to do so, demands true mastery over the host phosphor's internal lattice structure down to nano-volume region, such that every single electrons are accounted for photon emission, be it either in UVA, visible light and infra-red emission.

1.1 History of phosphors

The word “Phosphor” came from Greek word fosfor which means a substance that gives out light. The luminescence phenomena have always been associated with fluorescence and phosphorescence. For fluorescence, the light emission mechanism involves a two level-system. These two energy level system are a stable lower energy state called ground state and a non-stable higher energy state called excited state. Normally, electrons will stay at the excited state for a short period of time and this is called the lifetime of the state, before returning to ground state, emitting photons. Figure 1.1 shows us the various photoluminescence schemes, a) Band-edge recombination, b) Defect recombination and c) Auger recombination.

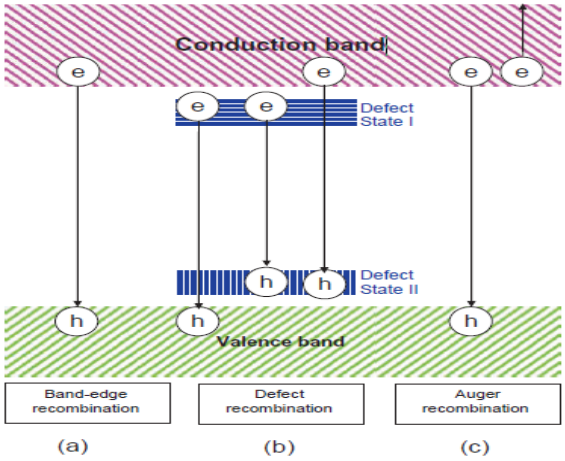

Figure 1.1 Various photoluminescence schemes

Fluorescence happens when an orbital electron of a molecule, atom or nanostructure relaxes to its ground state by emitting a photon of light after being excited to a higher quantum state by some type of energy.

Excitation: $S_0 + h\nu_{exc} \rightarrow S_1$

Fluorescence (emission): $S_1 \rightarrow h\nu_{emi} + \text{heat}$

The fluorescence lifetime refers to the average time the atom stays in its excited state before emitting a photon. A typical fluorescence equation is as follows:

$$[C_1]=[C_1]_o \, Exp(-\Gamma t)$$

where $[C_1]$ is the concentration of excited state molecules at time t, $[C_1]_o$ is the initial concentration and Γ is the decay rate or the inverse of the fluorescence lifetime.

Phosphorescence or persistent luminescence generally has a longer lifetime and it has a three-level system. The mechanism behind persistent luminescence goes like this, when an electron is excited to excited state, it will go into another energy level called trapping state and stays there until detrapping back to excited state occurs [1]. The returning electron will then follow the normal decaying processes to return back to ground state causing the emission of photons which is observed as persistent luminescence. Figure 1.2 shows us the comparison of energy levels diagram between a) fluorescence and b) phosphorescence.

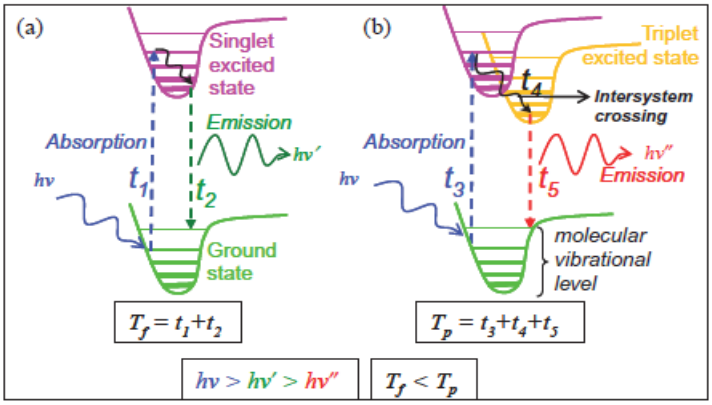

Figure 1.2 Energy diagram levels for fluorescence and phosphorescence

Phosphor material has a long history of over 2000 years. The Chinese has the earliest recorded history of phosphor paintings that dated back to Han and Song Dynasty. The Japanese has records of making phosphor paintings using sulfur from volcano and pearl shells gathered from seashore for about 1000 years ago. In Europe, the first phosphor material was discovered by Vincenzo Casciarolo and it was called the Bologna Stone in 1602. A journal “De Phenomenis in Orbe Lunae” published in 1612, stated that in order to

obtain a phosphor material, the raw materials has to be calcined. This was the first record of a method that is close to the current high temperature solid-state reaction for synthesizing phosphor material.

Modern phosphor research era started in the late 19^{th} century, with the discovery of ZnS phosphor which was first discovered by the French chemist, Theodore Sidot in 1866. Later on, the German scientist, Philip E. A. Lenard and his colleagues did a lot of pioneering work in phosphor research by establishing the basic governing principles for phosphors such as doping of metallic cations into host materials to make them more luminescence efficient [2]. Many alkaline chalcogenide phosphors were developed by Lenard's group and they are now commonly known as Lenard phosphors. The first modern phosphor developed for commercial application is $ZnS:Cu^{+}$ which was developed in 1920-30s [3,4]. It was later discovered that by co-doping ZnS phosphor with Co^{2+} and Cu^{+}, the afterglow decay curve could be doubled. On August 1996, Matsuzawa published an article that sent a shockwave through the phosphor research community by announcing that by co-doping $SrAl_2O_4:Eu^{2+}$ with Dy^{3+}, a high green brightness and long-lasting afterglow phosphor (over 16 hours) could be obtained [5]. This phosphor is based on the same $SrAl_2O_4:Eu^{2+}$ material synthesized by Abbruscato in 1971 [6]. A short time later, another long-lasting blue afterglow phosphor, $CaAl_2O_4:Eu^{2+}:Nd^{3+}$ was reported too [7,8]. The discovery of these two long afterglow phosphor has greatly revived the scientists' attention world-wide since the long afterglow duration greatly boosted the phosphor's commercial values.

Many new long afterglow phosphors have been discovered and developed since Matsuzawa's paper. In the 21^{st} century, phosphor research activities boomed and they were very application- oriented. In general, there are two directions in which the phosphor research is concentrated. First, is the identification of the trapping-detrapping mechanism leading to the long persistence luminescence. The second direction is in discovery and

development of new long afterglow phosphors that provide a wider spectral range from visible wavelengths to infra-red.

1.2 Method of preparation

There are many methods in preparing phosphor material such as high temperature solid-state reaction, sol-gel method, hydrothermal, co-precipitation and combustion method [9-22]. The most widely used method even nowadays in the industry is the solid-state reaction. This technique was well-established by Lehmann group. In this method, the necessary host material ingredients, usually in powder form, are mixed together with the dopant impurities. All these raw materials are mixed accordingly to certain stoichiometric proportions. In order to obtain final, high quality phosphor, careful steps are taken to ensure that mixing is thorough, therefore certain techniques were developed such as ball-milling and slurry method. The mixed ingredients are then placed in a furnace for sintering at high temperature, usually over 1000℃. This method relies on the diffusion process of solid species in which the temperature is the most critical factor. Firstly, the high temperature ensures that the raw solid species have the necessary thermal energy to cause reaction at solid phase and secondly, it can assist the diffusions among the raw material to happen with ease. In cases of low diffusion rates among the raw materials, a flux material is used. This flux material has a low melting point but with a high boiling point. The melted flux material creates a reaction zone for other raw materials to break down their boundary grain size so that fusion could occur among them to form the final phosphor material. In other words, flux material is used to reduce the sintering temperature and to increase reaction rate. However for this high temperature solid state method, the dopant impurities may suffer further oxidation, for example dopant Ce^{3+} could become Ce^{4+}. In order to avoid this, the furnace is built with flowing reducing gas such as 95% N_2 and 5% H_2 to create a reductive environment. Long lasting phosphor such as $SrAl_2O_4:Eu^{2+},Dy^{3+}$ and $CaAl_2O_4:Eu^{2+},Nd^{3+}$ are

fabricated in such environment. Other gases too can be utilized such as O_2 to create an oxidizing environment in case of $Y_2O_3:Eu^{3+}$ phosphor preparation and H_2S for sulfurizing oxides to become sulfides phosphor material. The final quality of phosphor material prepared through high temperature solid-state reaction depends largely on the sintering temperature and sintering time. Particle size's uniformity is a big issue for this method since the raw materials powder is large to begin with. The final phosphor's quality may also suffer from concentration gradient in which a non-uniform of doping concentration being spread out among the host lattice material. Figure 1.3 shows us the final sintered particle with oriented grains obtained through the high temperature solid-state reaction.

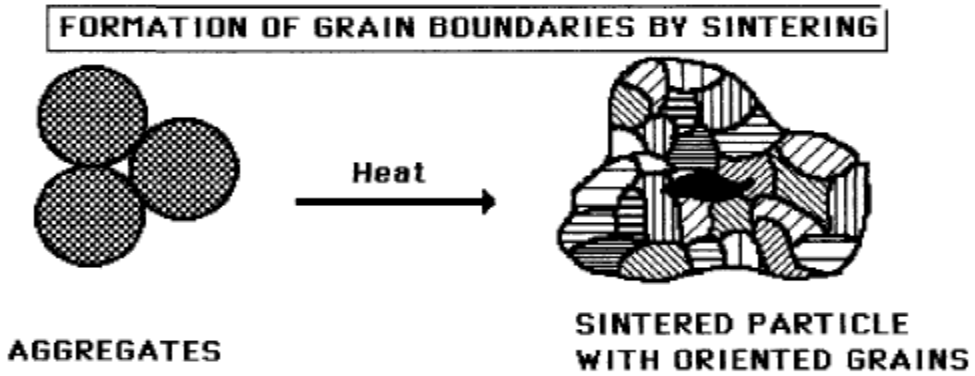

Figure 1.3 High temperature solid-state reaction route

1.3 Persistent luminescence mechanism

It has been almost 15 years since Matsuzawa's paper announcing the long lasting $SrAl_2O_4:Eu^{2+}:Dy^{3+}$ phosphor but the mechanism to explain persistent luminescence still elude the effort of many scientists who have tried to unravel it. The mankind's progress to solve this mystery is slow but after intense efforts; the consolation gained was only the discovery of a handful of phosphors that are bright enough for practical application. The general agreements reached among the afterglow phosphor research community that there are existence of long-lived trap levels and the main charge carriers are electrons but the details concerning the nature and origin of the traps and the charge carriers were still

unclear. The Matsuzawa model proposed in 1996 in which the persistent luminescence is due to hole carriers and involving Eu^{2+}/Eu^{+} and Dy^{3+}/Dy^{4+}, however, has lost its appeal due to certain flaws as pointed out later by other researchers. Figure 1.4 shows us the energy level diagram for $SrAl_2O_4:Eu^{2+},Dy^{3+}$ phosphor as proposed by Matsuzawa.

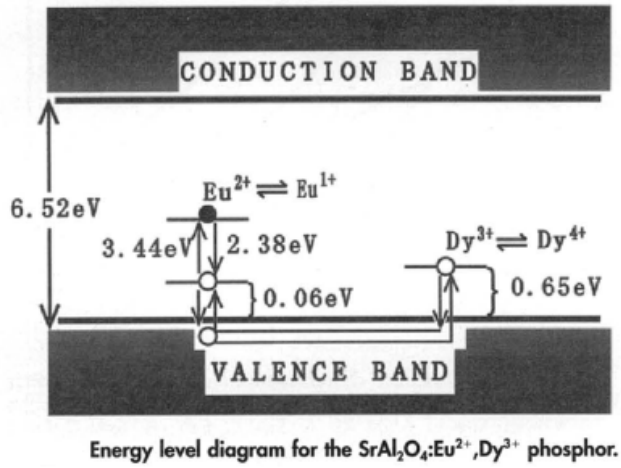

Figure 1.4 Matsuzawa model for $SrAl_2O_4:Eu^{2+},Dy^{3+}$ phosphor

Since every afterglow phosphor known tend to share the same characteristics, in which it always involve a host lattice material and dopant impurities then the general methods to design long persistent phosphors will have to take into consideration from these two aspects. By doing so, it appears to be two general explanations offered to describe the long persistent luminescence mechanism. We will discuss both viewpoints in the following section.

1.3.1. Co-dopant

It has been defined that traps play an important role in long persistent luminescence phenomena and there are two type of traps, one being the electron traps which capture electrom below the conduction band and the other being the hole traps which capture holes above the valence band. Certain host material exhibits defects due to charge compensation. For example, $CaS:Bi^{3+}$, in which two Bi^{3+} ions will replace three Ca^{2+} ion sites, resulting in a Ca^{2+} vacancy which is a site capable of trapping hole. But if instead two Bi^{3+} ions simply

replacing two Ca^{2+} ion sites, then an interstitial S^{2-} is needed to maintain the charge balance, leading to a host lattice environment that is able to trap electrons. However if a Na^{+} ion is co-doped together with Bi^{3+}, these two ions replace two Ca^{2+} ion sites, resulting in reduced charge-related defect centers , hence reducing the afterglow persistence time. Figure 1.5 shows us the various point defects that can occur in the heterogeneous ionic solid material.

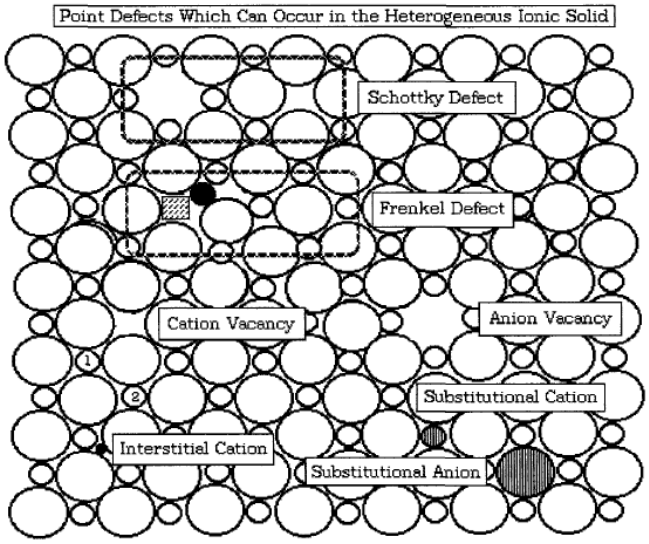

Figure 1.5 Point defects in the heterogeneous ionic solid material phosphor

The persistent luminescence mechanism proposed by Matsuzawa in 1996 for $SrAl_2O_4:Eu^{2+}:Dy^{3+}$ long afterglow phosphor is based largely on earlier measurements by Abbruscato on non-co-doped $SrAl_2O_4:Eu^{2+}$ which also shows a weak afterglow. From the Hall measurements obtained, Abbruscato concluded that holes in valence band had to be main charge carriers. The Matsuzawa model explains that when an Eu^{2+} ion is excited by an incident photon, there is a possibility that a hole escapes to the valence band, creating a Eu^{+} ion. This hole is then captured by a trivalent rare earth ion such as Dy^{3+}, thus creating a Dy^{4+} ion. After a short while, thermal energy causes the trapped hole to be released into the valence band again in which recombination occurs with Eu^{+}, creating back Eu^{2+} ground state with emission of a photon. This photon is observed as persistent luminescence. Various

experimental techniques were employed to test this model such as thermoluminescence, photoconductivity and electron paramagnetic resonance. However, the data of these experiments were often inconclusive and this raised questions on the validity of this model. In 2006, Aitasalo [23] proposed a mechanism for persistent luminescence that includes suggestions from Clabau [24] and Dorenbos [25]. Figure 1.6 shows us the persistent luminescence mechanism proposed in 2006 by Aitasalo et al for $CaAl_2O_4:Eu^{2+},Dy^{3+}$ phosphor.

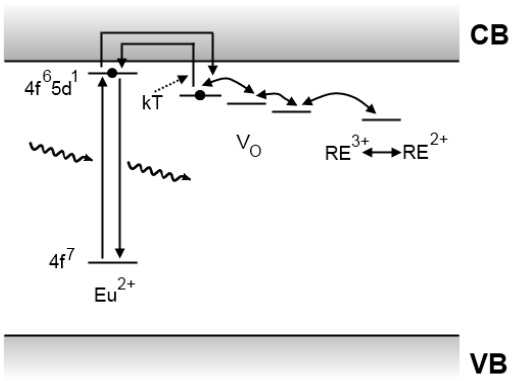

Figure 1.6 Aitasalo model for afterglow in $CaAl_2O_4:Eu^{2+},Nd^{3+}$ phosphor

It said that electrons that are excited in the Eu^{2+} luminescent centers can easily escape into the conduction band. Both the oxygen vacancies and trivalent co-dopant ions act to introduce trap levels but their exact nature were still sketchy because these defects could interact among each others to form complex aggregates. Presently, there have not been any exact mechanisms governing persistent luminescence materials that can really clarify the experimental findings. Many research groups have tried, each proposing their own version but none of them have enough experimental data to be identified as the true afterglow mechanism. The best model offered to explain persistent luminescence in co-dopant materials with Eu^{2+} as the luminescent center is that the co-dopant such as Dy^{3+} acts as electrons trap, holes trap or both electrons and holes traps or to induce charge-related defects or as energy transfer media.

1.3.2. Host lattice material

Of so many published papers on persistent luminescence materials, there is only a small number of scientific papers that focused on the role of host lattice material on afterglow phenomena. For example, the host material $Sr_4Al_{14}O_{25}:Eu^{2+}:Dy^{3+}$ have been investigated by other research groups with the following findings. In 2004, Zhao et al [26] reported that by changing the host composition, there is no observed influences on the emission peak's position but aluminium-rich host material exhibited better afterglow than strontium-rich host material. Based upon the thermoluminescence data, they explained that this is due to different trap levels and trap concentrations formed in the hosts. In 2008, Suriyamurthi et al [27] investigated the same $Sr_4Al_{14}O_{25}:Eu^{2+}:Dy^{3+}$ phosphor compound, in which they confirmed that Sr-deficient host material has enhanced afterglow intensity. In 2009, Luitel et al [28] published their findings that alumina grain size of 0.05 m being used in synthesizing $Sr_4Al_{14}O_{25}:Eu^{2+}:Dy^{3+}$ phosphor has yielded samples with higher initial brightness and longer persistent luminescence than alumina grain size of 0.1 m and 1 m. They also noticed that there is a slight blue shift in emission peak of phosphor samples made from 0.05 m alumina, in which they explained that the decrease in particle size and increase in the surface state energy causes the distortion of atomic structure around Eu^{2+}.

$M_2MgSi_2O_7:Eu^{2+}:Dy^{3+}$ (M=Ca,Sr, Ba) is another popularly studied long afterglow phosphor in which Lin et al [29] reported in 2003 that host material strontium has the best afterglow properties followed by host material barium and then calcium. Their report was confirmed in 2004 by Qin et al [30] in which they did a comparison study between $Sr_2MgSi_2O_7$ phosphor and $Ca_2MgSi_2O_7$ doubly doped with Eu^{2+} and Dy^{3+}. However their explanations is simple and crude, in which they stated that this is due to higher trap concentration generated by the co-doped rare earth cations in host material strontium than calcium. In 2007, Dongdong Jia et al [31] took up the same investigations on this phosphor compound. They did a vigorous study and concluded that $Sr_nMgSi_2O_{5+n}$ ($1 \leq n \leq 2$)

compounds have the same crystal structure as $Sr_2MgSi_2O_7$ with a defective phase and again, based upon thermoluminescence measurements, that co-dopant Nd^{3+} created much larger number of traps and hence improved the afterglow. At the same time, Hirotoshi, Holsa et al [32] decided to investigate the same phosphor compound but from a different perspective. They utilized TEM to scan and probe for lattice defects for three $Sr_2MgSi_2O_7$ phosphor compounds: undoped, doped with Eu^{2+} and doubly-doped with Eu^{2+}/Dy^{3+}. They discovered that sample co-doped with Dy^{3+} tends to have large number of small lattice domains created by discontinuities in the crystal structure. They also found out that these traps tend to get deeper with the presence of co-dopant Dy^{3+}.

In 2001, Yuanhua et al [33] did a study on $MAl_2O_4:Eu^{2+}/Dy^{3+}$ (where M:Ca, Sr, Ba) phosphor materials. They found out that the afterglow decay curve lifetime has the following order: $SrAl_2O_4$ > $CaAl_2O_4$ > $BaAl_2O_4$ which they claimed corresponded nicely to thermoluminescence data where the maximum glow peak are in the following order: $BaAl_2O_4$ > $CaAl_2O_4$ > $SrAl_2O_4$. They explained further that the trap depth is directly proportional to the maximum glow peak therefore the trap depth of Dy^{3+} in descending order is $BaAl_2O_4$ host > $CaAl_2O_4$ host > $SrAl_2O_4$ host. In 2003, T. Aitasalo et al [34] published their findings on effect of stoichiometry on the persistent luminescence lifetimes of $SrAl_2O_4:Eu^{2+}/Na^{+}$. They plotted a graph showing that the afterglow lifetimes in descending order is: $Sr_{0.97}Al_2O_4$ > $SrAl_2O_4$ > $Sr_{1.03}Al_2O_4$. They explained that for compound with strontium deficit, the quenching of Na^{+} is not significant but this may be due to the high amount of crystal defects which enhance the persistent luminescence.

In 2007, Guo et al [35] reports that they found out that the values of the decay times of $Ca_{0.9}Mg_{0.1}Ga_2S_4$: Eu^{2+},Ho^{3+} to be larger than of original phosphor $CaGa_2S_4$: Eu^{2+},Ho^{3+}, illustrating that the former phosphor had a superior afterglow than the original phosphor. Even though they did not offer detailed explainations but they stressed the importance of increasing the phosphorescence through a slow decay process.

In 2010, Zhang et al [36] reports that by substituting Ti with Zr in $CaTiO_3:Pr^{3+}$ phosphors, they found out that there is an enhancement of red fluorescence and phosphorescence at 613 nm originating from the $^1D_2$ to $^3H_4$ transition of Pr^{3+} and increases the lifetime for the $^1D_2$ state. They claimed that by adding Zr^{4+}, induces a lattice symmetry change from orthorhombic to pseudocubic , which can significantly enhance the red fluorescence intensity and the afterglow duration. They elaborated that the enhancement of the afterglow could be due to the increase of $[Pr_{Ca}]^0$ trapping centers because the number of Pr^{4+} reduced from Pr^{3+} decreased when unstable Ti^{4+} was replaced by stable Zr^{4+}.

In this thesis, we study and attempt and explain persistent luminescence mechanism or afterglow from host lattice material's point of view by fabricating phosphor material using organic coated luminescence ZnO nanopowder. This route has not been reported before and there are two major fundamental differences in our approach as compared to traditional high temperature solid-state reaction. First, one of our raw starting ingredients, the organic coated luminescence ZnO nanopowder has already been in nano-sized initially and remains so within the cooled, final obtained phosphor material. While as, in the conventional high temperature solid-state reaction approach, the raw starting ingredients has already been in bulk powder form and will always yield a final phosphor material in bulk form. Second, we did not include any rare-earth co-dopants such as Eu^{2+}, Dy^{3+} to prolong the afterglow duration when we fabricated our phosphor samples by changing the host material constituents, zinc oxide, in $CaZnGe_2O_6:Tb^{3+}$ long afterglow phosphor. We just devoted our attention to using single dopant Tb^{3+} as the main luminescence centers.

CHAPTER 2

ZINC OXIDE NANOPARTICLES

2.1 Zinc Oxide nanoparticles

ZnO is a II-VI semiconductor compound. ZnO material is an interesting material to study because of its optoelectronics properties [37,38]. This material has tremendous potential to be used in applications such as ultraviolet laser devices, thin-film transistors, additives in paint industry and biomedical label [39,40]. ZnO has a wide 3.37 eV [41] band gap at room temperature which is higher than other popularly known quantum dots such as CdSe (1.7eV) and CdTe (1.5eV) which made it ideal host material for doping. This wide-band energy gap's property enable ZnO to be transparent in the visible part of electromagnetic spectrum. ZnO nanomaterial are cheap to produce, has low toxicity, exhibits strong stability under ultraviolet light and its UV emission peak are narrow and symmetric. Due to its large exciton binding energy (60 meV) [42], the excitons in ZnO material are thermally stable at room temperature. It also have high electromechanical coupling constant and piezoelectric properties. ZnO material also has good heat capacity, heat conductivity, low thermal expansion and high melting temperature and this made them ideal for ceramics applications. The photoluminescence of ZnO material has two components, excitonic emission and surface state or defect emission [43]. The sharp excitonic emission (380 nm) [44] is believed to be due to photogenerated electrons that recombine with holes in valence band. The surface state or defect emission ranging in visible ranges from blue to red, which is not fully understood but is highly thought to be due to oxygen vacancies state at the

material's surfaces. ZnO has ionicity that resides in between covalent and ionic semiconductor. ZnO powder has white physical appearance and is insoluble to water, and it crystallizes in hexagonal wurzite, cubic zinc blende and the rare cubic rocksalt form. However little literature is reported on ZnO nanomaterial that is modified to be in water-soluble form, since for biological applications, a nanomaterial dispersed in water-solvent is a crucial condition. The characteristics of ZnO nanoparticles synthesized is hugely dependant on their size and the preparation methods. In this thesis, we synthesized our ZnO nanoparticles by using a wet-chemistry method in which an organic stabilizer is used to form a stable reverse micelle [45] , thus creating nano-reactors environment in which the Zn^{2+} and OH^- react to create the ZnO nanoparticles. Figure 2.1 shows us a typical reverse micelle method to synthesize ZnO nanoparticles.

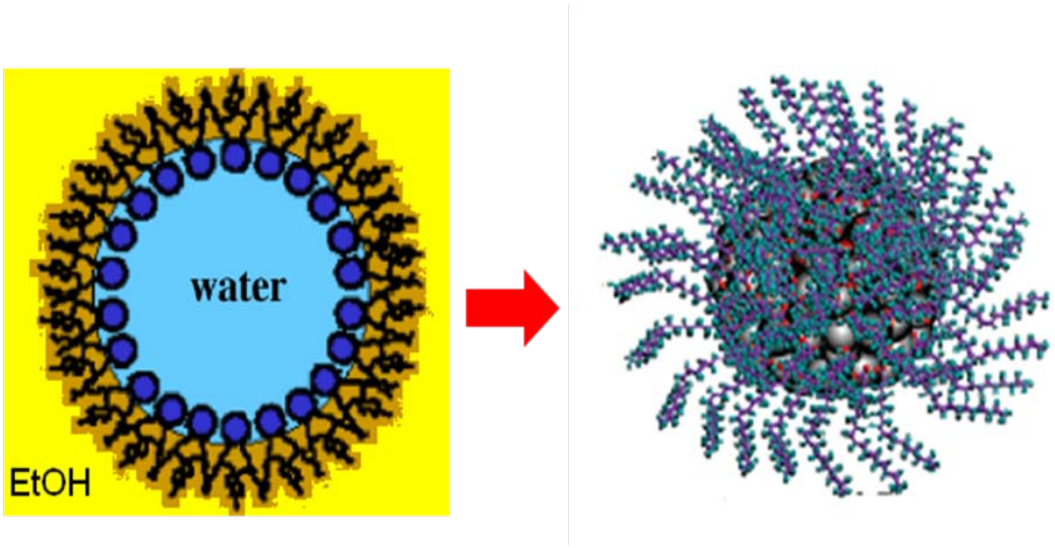

Figure 2.1 Reverse micelle method to synthesize ZnO nanoparticles

2.2 Synthesis of Zinc Oxide nanoparticles

The preparation of ZnO nanopowder is a simple approach that have been reported previously in many scientific literature [46,47] . A 2.2945 gm (8.7 mmole) sample of zinc acetylacetonate hydrate powder ($Zn(ACAC)_2$) was dissolved into 30 ml of ethanol and 10 ml of deionized water (DI). The prepared solution was subjected to ultra-sonification and then

placed into a flask that was connected to a water condenser. This solution was then heated to the boiling point of ethanol (~80℃) under vigorous magnetic stirring. A solution of 0.5 gm of NaOH pellets (12.5 mmole) dissolved in 30 ml of ethanol, which was kept at about 0℃, was then added to the heated solution. A white precipitate was observed and then collected after heating for 45 minutes. The white precipitate was washed with acetone and cool DI water to remove any impurities and then left to dry at room temperature for 2 days. The procedures for making ethanol-soluble ZnO nanoparticles were similar to the nanopowder preparation except that the nanoparticles were coated with polyethylene glycol biscarboxymethyl ether ($PEG(COOH)_2$). The heated solution was modified to 1.4129 gm (5.36 mmole) of zinc acetylacetonate hydrate powder and 40 ml of ethanol solvent. The cooled solution consisted of 0.3 gm of NaOH pellets (7.5 mmole) dissolved in 40 ml of ethanol. A 0.8491 gm (3.3 mmole) sample of polyethylene glycol biscarboxymethyl ether ($PEG(COOH)_2$) was added to water resulting in a total volume percentage of DI water of 0.003% for both complete solution mixtures. The cooled solution was added carefully and slowly into the heated solution at about 80℃. After a heating time of 30 minutes under vigorous magnetic stirring, the final ethanol-soluble luminescence ZnO nanoparticles solution was obtained.

2.3 Results and Discussions

Figure 2.2 shows us the TEM of the obtained ZnO nanoparticles. The nanoparticles appear spherical in shape and are quite uniform in size. The ZnO nanoparticles' size is found to be ranging around 5-10 nm. The lattice spacing is found to be 0.264 nm which is in agreement with other ZnO nanoparticles reported by other research group [48-50].

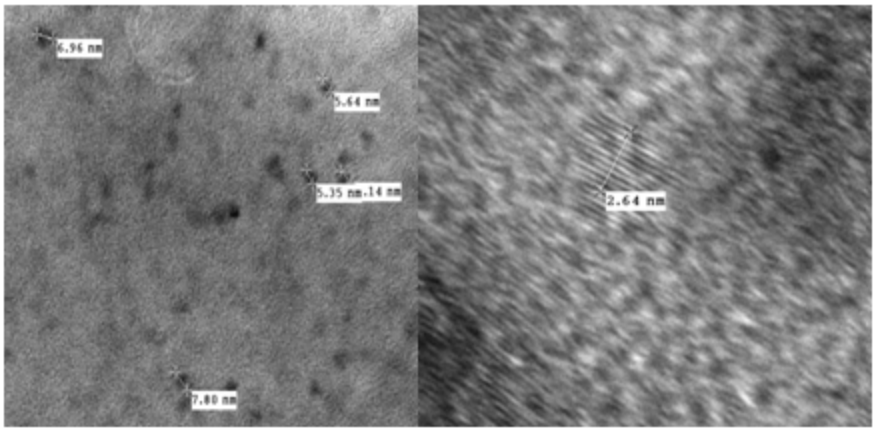

Figure 2.2 TEM of ZnO nanoparticles

Figure 2.3 shows us the XRD pattern of both organic coated luminescence ZnO nanopowder and its annealed sample. Most of the diffracted peaks seen with the organic coated sample are due to the PEG organic layer that has the tendency to diffract the X-ray beams. But once the organic coated sample is annealed at 700℃ for two hours thus removing the protective organic layer, the obtained annealed sample's XRD profile is clearly in agreement with the hexagonal zincite (JCPDS card no:36-1451). By using the Debye-Scherrer equation, $t=0.89\ /\ \cos\ $, where t is the average crystalline size, is the X-ray wavelength (0.154505 nm), and and are the diffraction angle and full-width at half-maximum respectively, the ZnO nanopowder's crystalline size is estimated to be about 14 nm.

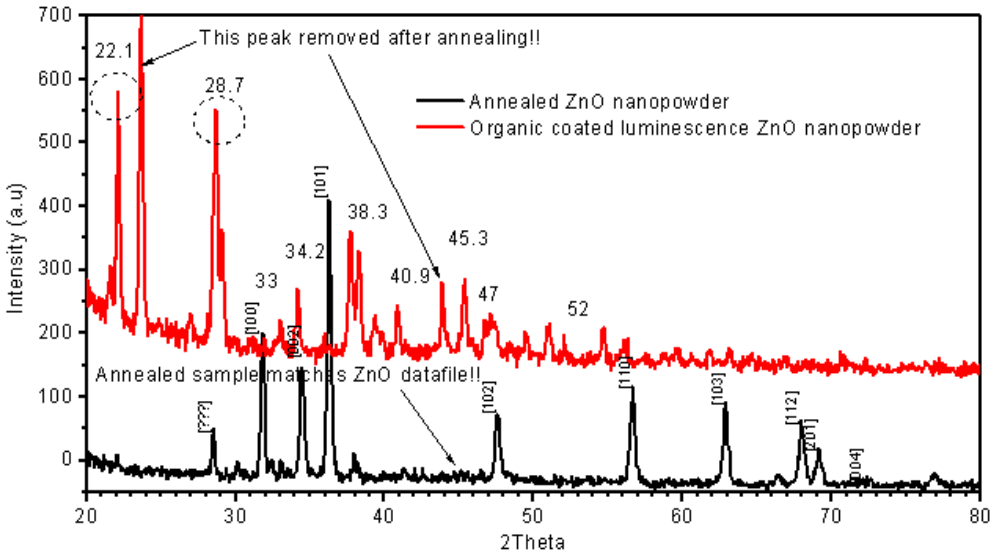

Figure 2.3 XRD of organic coated luminescence ZnO nanopowder

Figure 2.4 shows us the optical properties of the obtained ZnO nanoparticles in ethanol solvent. The strong absorption peak around 350 nm is a clear indication of ZnO's intrinsic property which is a strong UV light absorbant. A simple step in which small amount of DI water is to be added in or decreased during the wet-chemistry process, we could shift the broad green-yellow emission or the surface defect emission of ZnO nanoparticles. This is due to adjusting volume size of the water micelle being surrounded by the hydrophilic part of the stabilizer $PEG(COOH)_2$. The bigger the water micelle's volume is, the more red-shifted the ZnO nanoparticles' surface defect emission. This final ZnO-ethanol nanosolution can be converted into ZnO/silica nanoparticles water solution by adding some amount of TEOS and DI water.

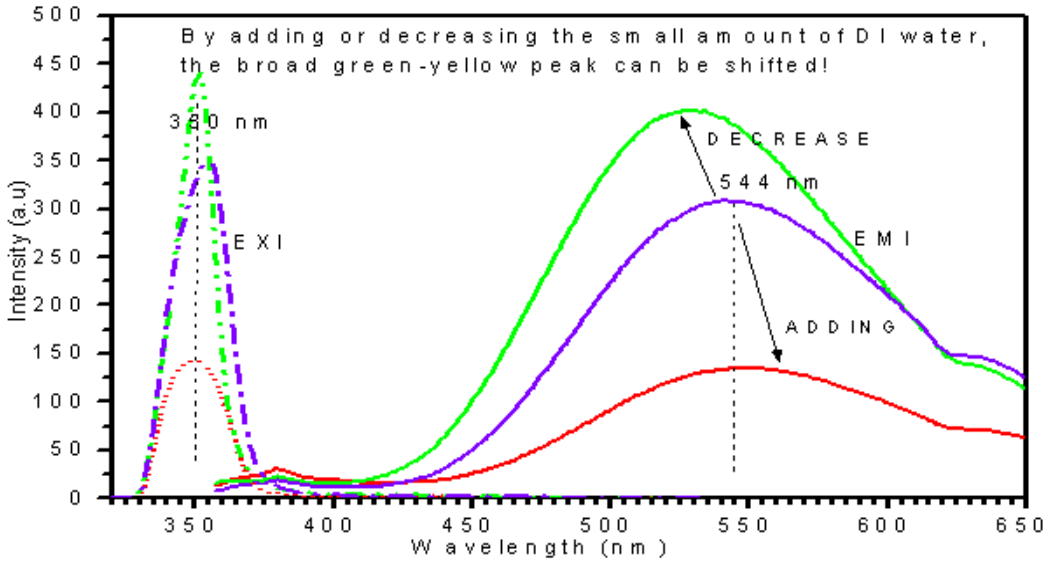

Figure 2.4 Excitation and Emission spectras of luminescence ZnO nanosolution

However we observed some interesting phenomena that took place once we diluted further the ZnO nanosolution with absolute proof ethanol until its absorbance peak in UV range down to 0.675. The absorbance 0.675 is achieved only through experimental approach with the goal of bringing the absorbance value for the mother solution down to below 1. Figure 2.5 shows the metamorphosis of the ZnO nanoparticles in the diluted ethanol solvent over a length of 23 days. In the beginning there is a very weak excitonic 380 nm emission from the ZnO nanoparticles, but as the days went by, it began to strengthen until a sharp excitonic emission profile emerged on the 23rd day since the dilution process. With the additional of more ethanol solvent, this caused the breakdown of the ZnO nanoparticles that aggregated during their initial formation process through nano-reactors that are encapsulated by PEG molecules (Figure 2.1) into smaller clumps since there are more volume for the ZnO nanoparticles to spread around. This made the as-obtained surface defect green-yellow defect emission in mother solution to shift into shorter wavelength or the excitonic emission becomes more distinct. . Figure 2.6 shows us the changing process that took place when the sample was excited by 238 nm. It shows that PEG(COOH)$_2$ molecules are hard at work in

doing surface passivation to change the surface state of the ZnO nanoparticles from day 1 to day 3 where its 331 nm emission is most intense. The surface defect emission 550 nm is no longer visible due to the dilution process. Once the surface passivation process is done, the $PEG(COOH)_2$ 331 nm emission began to reduce and the excitonic emission of the ZnO nanoparticles become more dominant.

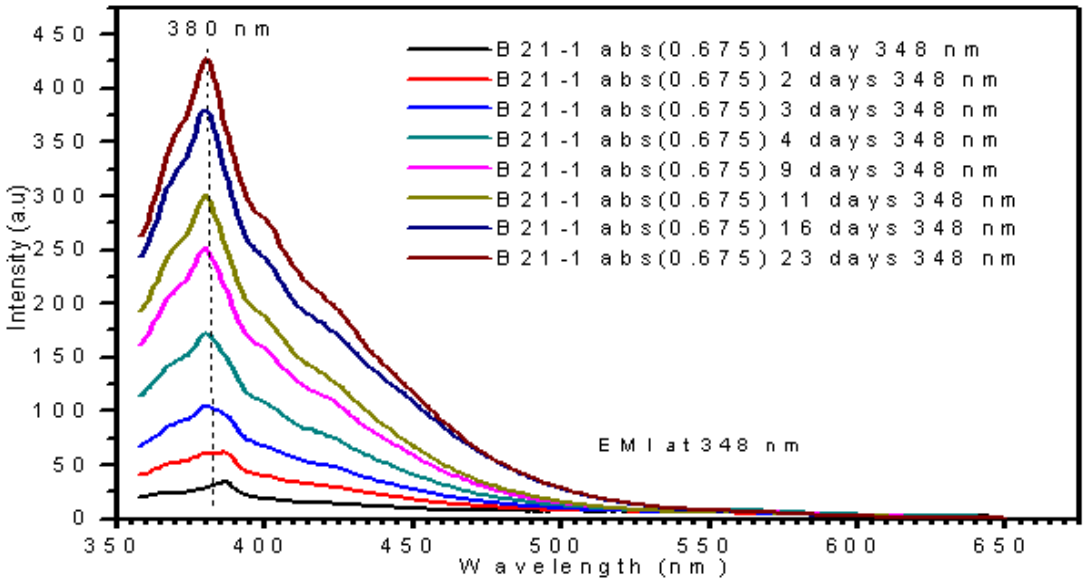

Figure 2.5 Emission spectras at 348 nm for diluted sample from 1 day to 23 days

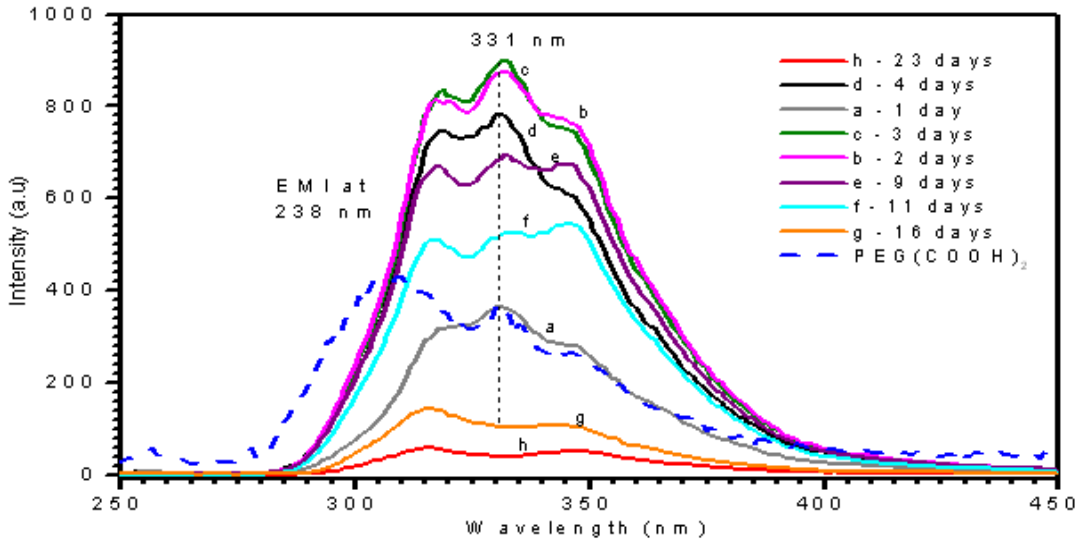

Figure 2.6 Emission spectras at 238 nm for diluted sample from 1 day to 23 days

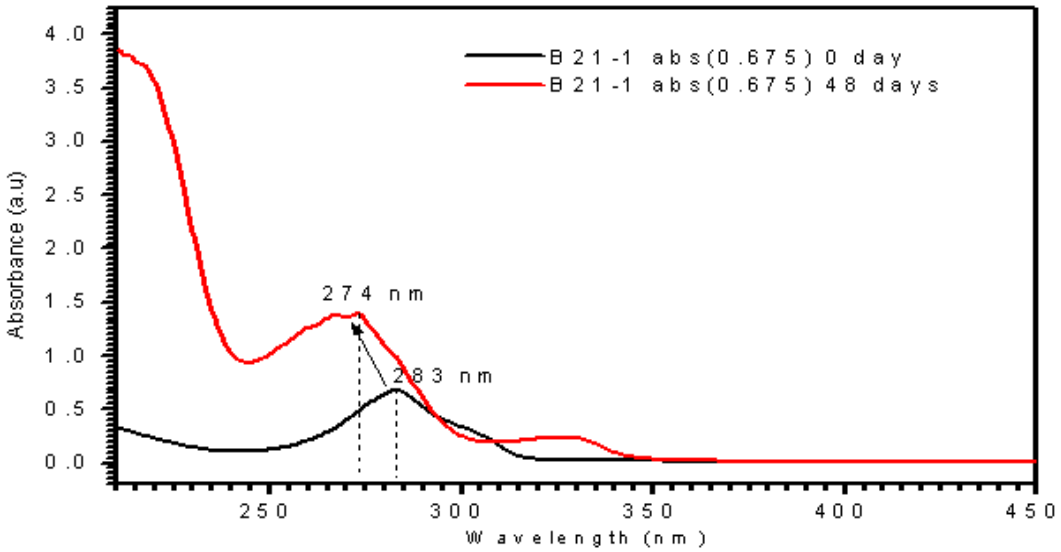

Figure 2.7 Absorbance spectras for diluted samples

Figure 2.7 shows us the absorbance spectra of both same sample after diluting at 0 day and after 48 days. The onset of the absorption is in consistent with ZnO nanoparticles of size 10 nm which is in agreement from the XRD data.

2.4. Conclusions

ZnO-PEG$(COOH)_2$ nanosolution in ethanol solvent has been successfully synthesized. The ZnO nanoparticles have a hexagonal structure with an average size of 10 nm. The mother solution has a strong luminescence of 545 nm due to surface defects but a weak excitonic emission. Upon dilution in ethanol, the green defect-related emission decreases and the excitonic 380 nm emission increases in intensity over the course of several weeks. This is due to surface passivation processes by PEG$(COOH)_2$ and other associated organic ligand such as CH_3COO^-.

CHAPTER 3

GADOLINIUM OXIDE NANOPARTICLES

3.1 Gadolinium Oxide nanoparticles

Gadolinium oxide is one unique rare-earth oxide material that has many advanced technological applications [51-54]. There are many approach to fabricate Gd_2O_3 materials such as solid-state reaction, sol-gel and flame spray pyrolysis [55-57] . This material has two common lattice structure which are monoclinic and cubic crystal structure. It appears as white odorless powder and is insoluble in water. Gadolinium oxide has a wide band gap of 5.4 eV and high thermal stability on silicon. Beside possessing a high permittivity (k=10-16), this material has found its usages as high index optical film material, infra-red absorbing automotive glass, microwave applications and catalyst in oil industry. Optical properties studies of this material reveals that when doped with Tb^{3+} or Ce^{3+}, this material becomes an efficient green-emitting phosphors that can be used as color TV tube phosphors. Due to its paramagnetic properties and symmetric electronic ground state, Gd^{3+} is also widely used as contrast agent for magnetic resonance imaging.

With the event of 9/11, radiation detection for potential nuclear weapons and radiological dispersal devices (dirty bombs) has become a top priority for United States government. In order to achieve efficient radiation detection, these criteria must be met, namely, the sensitivity, response time and energy resolution. An optimal scintillator must have high quantum efficiency, a short luminescence decay time and high stopping power. Ce^{3+}-doped scintillators provide an interesting option since it has an allowed 5d-4f transition

that has high luminescence quantum efficiency and has nanoseconds lifetime decay curve. However, these Ce^{3+}-doped scintillators tend to have their emission in UV-blue wavelengths.

This created limitations for radiation detection as UV-blue emissions are absorbed strongly by water and organic compounds. By combining both gadolinium oxide nanoparticles doped with Ce^{3+}, a scintillating nanoparticles system can be realized with enhanced detection capabilities as compared to bulk crystal scintillators. This chapter is devoted to report such findings because we observed and studied the green emission in Ce^{3+}-doped gadolinium oxide nanoparticles coated with PEG layer.

3.2 Synthesis of Gadolinium Oxide nanoparticles

The procedure to prepare nanopowder samples is as follows: 0.65 g (1.42 mmole) of gadolinium acetylacetonate hydrate powder was dissolved into 40 ml ethanol with the help of ultra-sonification. Next 2 ml deionized (DI) water was added to the mixture followed by 0.679 gm of polyethylene glycol biscarboxymethyl ether (PEG-COOH). The prepared solution was then placed into a flask that was connected to a water condenser. This solution was heated to the boiling point of ethanol (~80 ºC) under vigorous magnetic stirring. A solution of 0.2 g NaOH pellets (5 mmole) dissolved in 40 ml ethanol which was kept at about 0 ºC was then added to the heated solution. A white precipitate was observed and the heated solution became cloudy.After a heating time of 30 minutes, the solution was separated from the solid by filtration. The precipitate was washed with cold deionized water and acetone and then left to dry in ambient conditions for several days before subjected to heat treatment at 700℃ for 4 hours.

3.3 Results and Discussions

Figure 3.1 shows a TEM image of the $Gd_2O_3:Ce^{3+}$ nanoparticles. The average size of the Gd_2O_3 nanoparticles was found to be 3-5 nm. The nanoparticles appear with regular crystalline lattices with lattice spacing of D_{222}=3.2 Angstrom which is in agreement with results reported by Bazzi and Mahajan.

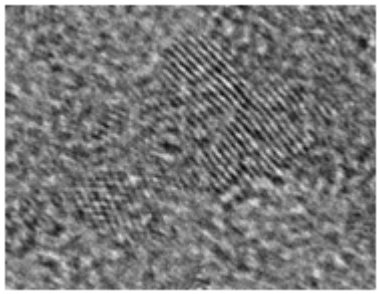

Figure 3.1 TEM of $Gd_2O_3:Ce^{3+}$ nanoparticles

The X-ray diffraction (XRD) patterns of all annealed doped gadolinium oxide nanoparticle samples, $Gd_2O_3:Eu^{3+}$, $Gd_2O_3:Ce^{3+}$ and $Gd_2O_3:Eu^{3+}:Ce^{3+}$ are shown in Figure 3.2. The XRD peak signatures of all annealed samples match well with gadolinium oxide (ICSD card #033652) with cubic features and body-centered lattice. No impurities were observed in the XRD measurements.

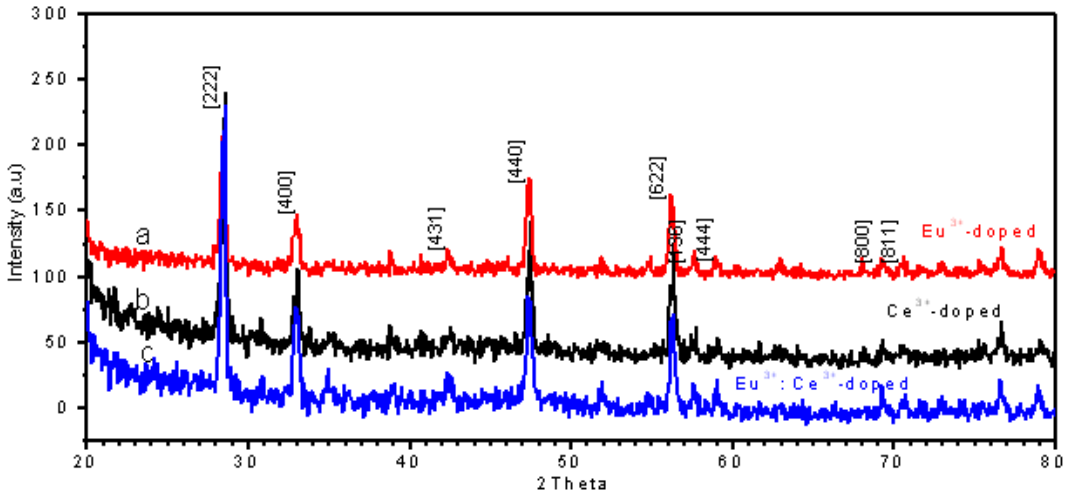

Figure 3.2 XRD of doped gadolinium oxide nanoparticles

Figure 3.3 shows us the green emission that is observed from the organic coated gadolinium oxide nanopowder. In order to probe deeply the origin of the green emission, samples with different Ce^{3+} concentrations were synthesized and their excitation and emission spectras recorded. The optimal Ce^{3+} doping is at 3.3% and any higher Ce^{3+} doping concentration will result in concentration quenching. The same undoped organic coated gadolinium oxide nanopowder was prepared in same condition and this sample exhibited a weak blue emission around 423 nm as shown in Figure 3.4. This weak blue emission is likely due to $PEG(COOH)_2$ stabilizer as its emission spectra are similar (Figure 3.4). As time passes by, we note that the undoped organic coated gadolium oxide nanopowder's emission shifts to 500 nm and is virtually identical to the emission from the organic coated Ce^{3+}-doped gadolinium oxide nanopowder.

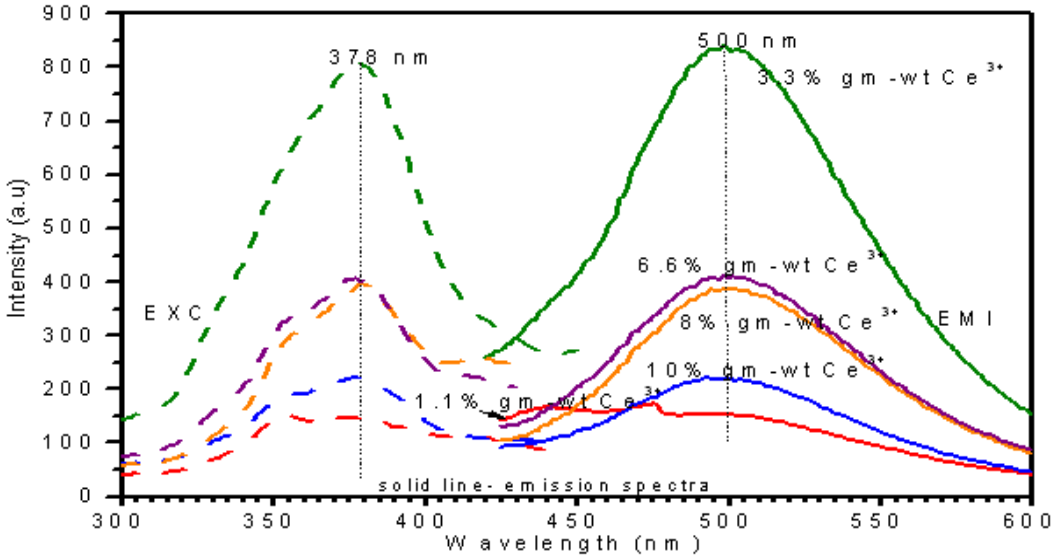

Figure 3.3 Excitation and Emission spectras of Ce^{3+}-doped gadolinium oxide nanoparticles

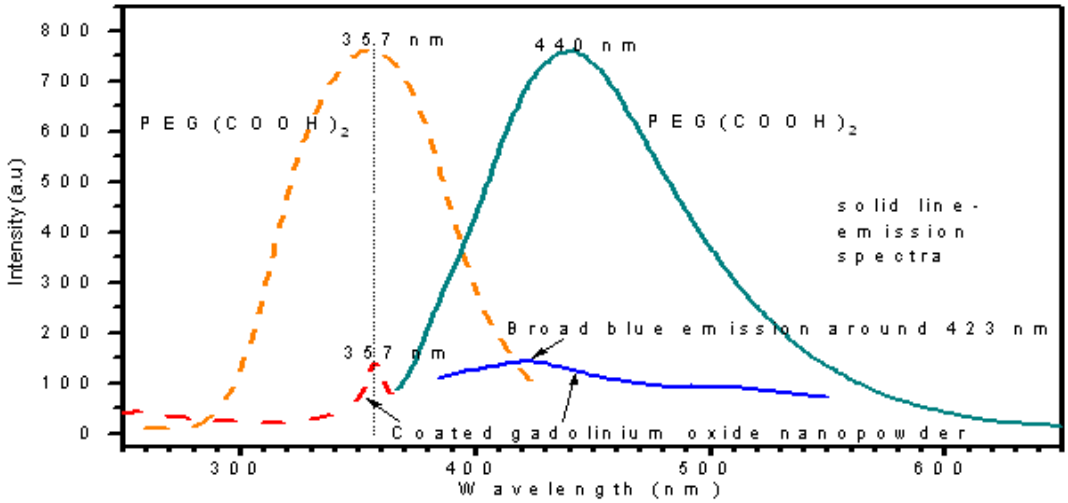

Figure 3.4 EXC and EMI spectras of $PEG(COOH)_2$ and gadolinium oxide nanoparticles

This changes could be due to changes in defect species or concentration or could be from oxidation of the surface ligands. The organic coated Ce^{3+}-doped gadolinium oxide nanopowder's excitation spectra for 500 nm has a shoulder peak around 352 nm and a pronounced peak at 378 nm. By comparison with the excitation spectra of $PEG(COOH)_2$ and

undoped organic coated gadolinium oxide nanopowder, we clarify that the shoulder peak at 352 nm is due to the stabilizer $PEG(COOH)_2$ and the main peak at 378 nm originates from the Ce^{3+}-doped gadolinium oxide nanoparticles.

The Ce^{3+}-dopant remains a possible root cause of the 500 nm emission as it is similar to the green emission from YAG:Ce^{3+} nanoparticles. In order to solve this riddle, we carefully measured the luminescence lifetime of the 500 nm emisison. We found out after detailed inspection that this emission has lifetime components on predominantly two time scales, the picoseconds and miliseconds time scales. Time-resolved spectra following excitation at 395 nm are shown in Figure 3.5 for the 3.3% Ce^{3+}-doped sample. The two spectra correspond to the emission produced in the first microsecond and the emission produced from first microsecond to final 2 miliseconds. This result clearly shown the early time emission is blue-shifted relative to the slower, milisecond time scale luminescence. Figure 3.6 shows us the monitoring of the green 520 nm at excitation 395 nm which yields a 1 milisecond lifetime and at excitation 285 nm which yields a 350 picoseconds lifetime. It is extremely unlikely that the miliseconds component originates from Ce^{3+} as the lifetime is significantly longer than the luminescence lifetime of nanoseconds of the Ce^{3+}'s 4f-5d transitions. In bulk phosphors. This emission is likely orignates from trap states within the band gap, which is commonly known to produce broad featureless luminescence. The faster time scale luminescence that has predominant lifetime of about 350 picoseconds is significantly shorter than a typical Ce^{3+} luminescence lifetime. However upon aging, the undoped organic coated gadolinium oxide nanopowder displays the same identical lifetimes as the Ce^{3+}-doped organic coated gadolinium oxide nanopowder. Therefore it is

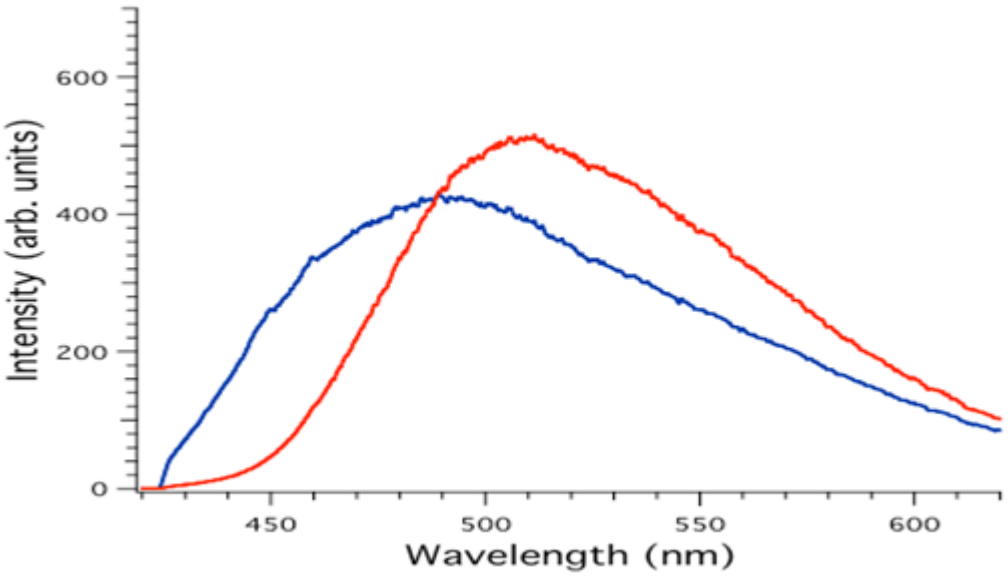

Figure 3.5 Time resolved spectra at 395 nm for Ce^{3+}-doped gadolinium oxide nanoparticles

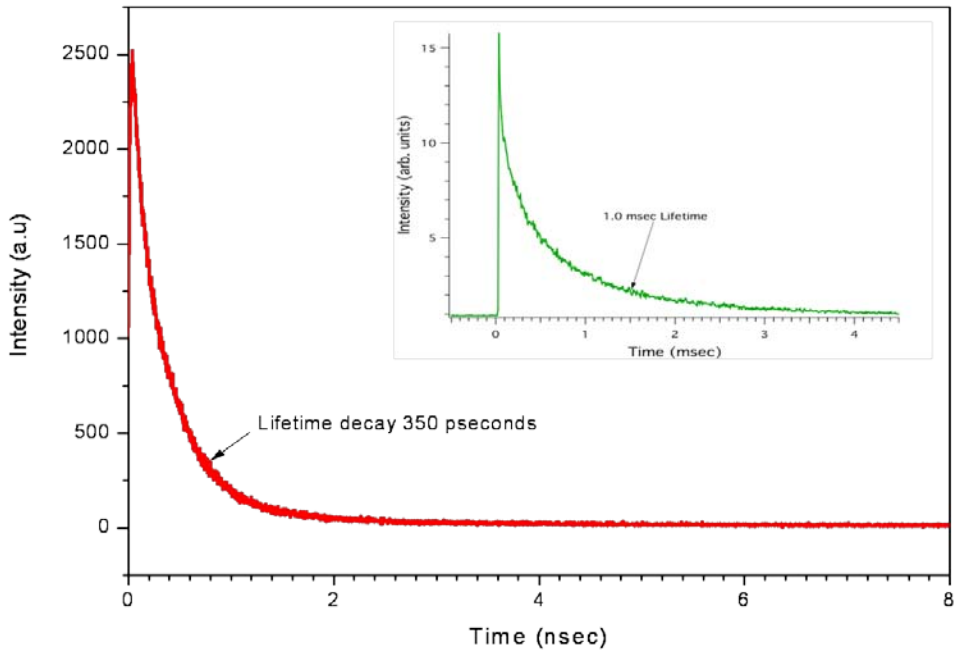

Figure 3.6 Lifetime decay curves of Ce^{3+}-doped gadolinium oxide nanoparticles

unlikely that this emission originates from Ce^{3+} as well. It is likely that this faster time scale emission also originates from the surface defect states of the gadolinium oxide nanoparticles. These defect states are presumed different from those responsible for slower time scale emission as the lifetime and the spectrum are significantly changed. Furthermore, we annealed the samples in air at 700℃ for 2 hours and the green emission either decreased in intensity or completely disappeared. The disappearance of the green emission could be due to the oxidation of surface ligands or changes in the defect state type or concentration.

Blue, green and red are the basic colors required for solid-state ligthning and displays. In order to obtain these three colors, dopant Eu^{3+} can be co-doped into the gadolinium oxide nanoparticles with Ce^{3+} ions. The obtained samples exhibited very weak blue emission from the stabilized $PEG(COOH)_2$ but the green emission from Ce^{3+} associated defects and the red emission from Eu^{3+} are intense. The excitation and emission spectra of this organic coated $Gd_2O_3:Eu^{3+}:Ce^{3+}$ nanopowder are shown in Figure 3.7. The emission peaks at 592 nm and 612 nm are from the $^5D_0$-$^7F_1$ and $^5D_0$-$^7F_2$ transitions of Eu^{3+} ions. The emission at 502 nm is similar to the defect-related emission observed in the single doped nanoparticles. When the green emission at 500 nm is monitored, the excitation spectrum has only one peak at 377 nm which is in agreement with the organic coated $Gd_2O_3:Ce^{3+}$ nanoparticles excitation spectra. When the red emission of Eu^{3+} at 612 nm is monitored, the excitation spectra has two sharp peaks at 462 nm and 547 nm, two broad peaks at 330 nm and 377 nm as well as a long tail from 225 nm to 300 nm. The excitation spectra at 377 nm is attributed to the absorption of Ce^{3+} ions. The shoulder from 225 to 300 nm is likely frm the band-band transition of the gadolinium oxide host as reported in the literature but could also contain some Ce^{3+} contribution. The excitation peak at 330 nm is attributed to charge transfer states (CTS) from oxygen (O^{2-}) to Eu^{3+} as it is similar to the CTS reported in other oxides doped with Eu^{3+}. The two sharp peaks at 462 nm and 547 nm are from the $^7F_0$-$^5D_2$

and $^7F_0$-$^5D_1$ transitions of Eu^{3+}, respectively. When the sample is excited at 330 nm, only the emission from Eu^{3+} ions are observed.

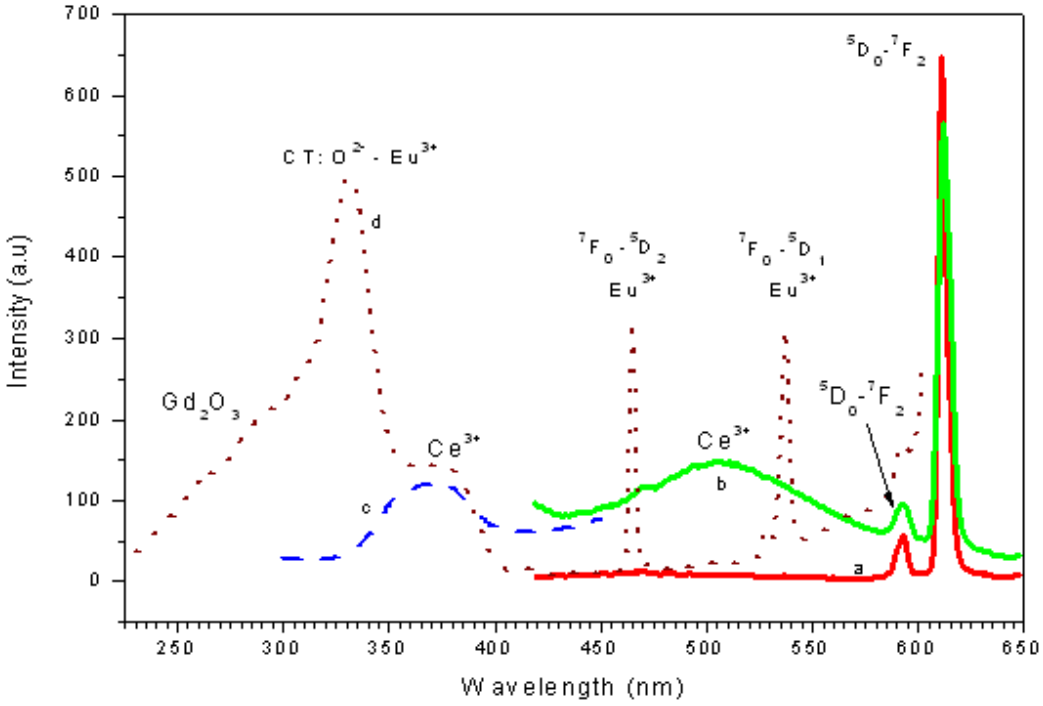

Figure 3.7 EXC and EMI spectras of Eu^{3+}-Ce^{3+} doped gadolinium oxide nanoparticles

This also indicates that the excitation peak at 330 nm is due to Eu^{3+} ions. At this excitation wavelength, the gadolinium oxide nanoparticles show little excitation as shown in Figure 3.7. When the sample is excited at 377 nm , both the green emission from the defects and the red emissions from Eu^{3+} ions are observed as this wavelength excites both Eu^{3+} and the defect states in the gadolinium oxide nanoparticles. By combining both green and red emission provide a key approach for the design and synthesis of multicolor phosphors, which will be investigated more in the near future.

3.4 Conclusions

In summary, green emission near 500 nm is observed in Ce^{3+}-doped organic coated gadolinium oxide nanopowder which has contributions from different types of defect states. The intensity of this green emission is highly dependent on the concentration of Ce^{3+} in the nanoparticles. The luminescence lifetime of this peak shows multiple time scales ranging from picoseconds to milliseconds. The lifetimes of this emission do not match typical Ce^{3+} lifetimes, and are nearly identical in undoped organic coated gadolinium oxide nanopowder. This leads to the conclusion that the green emission originates from a different types of surface defect states, possibly induced by presence of Ce^{3+} dopants.

CHAPTER 4

$CaZnGe_2O_6$ LONG AFTERGLOW PHOSPHOR

4.1 Introduction

We choose the host material $CaZnGe_2O_6$ long afterglow phosphor for our study mainly because this material has low synthesis temperature ~1100℃, stronger physical hardness attribute, high chemical stability and finally it has the zinc oxide compound in which we could substitute them with our organic coated luminescence ZnO nanopowder. This material is a member of pyroxene group of minerals which have a mononoclinic crystal structure. The word “Pyroxene” comes from the greek words for “Fire” and “Stranger” since this material is commonly found as crystals embedded in volcanic glass. This calcium clinopyroxenes exhibit isomorphous and isostructural with their space group C2/c being able to crystallize with ease at room temperature.

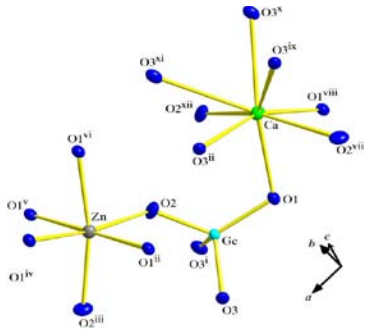

Compound (II)

Crystal data

$CaZnGe_2O_6$
$M_r = 346.63$
Monoclinic, $C2/c$
$a = 10.1659\ (8)$ Å
$b = 9.0096\ (7)$ Å
$c = 5.4369\ (4)$ Å
$\beta = 105.181\ (4)°$
$V = 480.59\ (6)$ Å^3
$Z = 4$

$D_x = 4.791$ Mg m^{-3}
Mo $K\alpha$ radiation
Cell parameters from 1520 reflections
$\theta = 2.1–28.2°$
$\mu = 18.40$ mm^{-1}
$T = 298\ (2)$ K
Cuboid, colourless
$0.15 \times 0.12 \times 0.11$ mm

Figure 4.1 Crystal structure and data of $CaZnGe_2O_6$ phosphor

Figure 4.1 shows us part of the $CaZnGe_2O_6$ structure and its crystal lattice parameters. Pyroxenes generally come in chemical composition of $AB(Si,Al)_2O_6$ in which A represents

calcium, sodium, magnesium and B represents cations of smaller size such as aluminium, scandium, titanium and vanadium.

4.2 Experimental Details

The afterglow phosphor powder samples were prepared according to stoichiometric proportions with the following amounts of Germanium oxide [0.878 gm, 8.4 mmole] Calcium oxide [0.235 gm, 4.2 mmole], Bulk Zinc oxide powder and/or organic coated luminescence ZnO nanopowder [Total mass of 0.342 gm, 4.2 mmole or 100% gm-weight] and Terbium (III, IV) oxide [0.03 gm, 0.04 mmole]. All chemicals were obtained from Sigma-Aldrich with the exception of the organic coated luminescence ZnO nanopowder. All powders were thoroughly mixed together, placed in a covered crucible and annealed at 1100℃ for 90 minutes under normal atmospheric condition. Approximately 1.3 gm of hardened white samples in shallow bowl shape was obtained and then crushed into powder form using the mortar and pestle. These afterglow phosphor powder samples were then subjected for further characterizations.

4.3 Results and Discussions

4.3.1. $CaZnGe_2O_6$ long afterglow phosphor

We start off by discussing the results of the afterglow phosphor samples without any dopant presence. Figure 4.2 shows us the optical properties of 3 samples for comparison studies. They are samples made of 100% gm-weight bulk ZnO, 100% gm-weight nano ZnO and 70%:50% gm-weight bulk and nano ZnO.

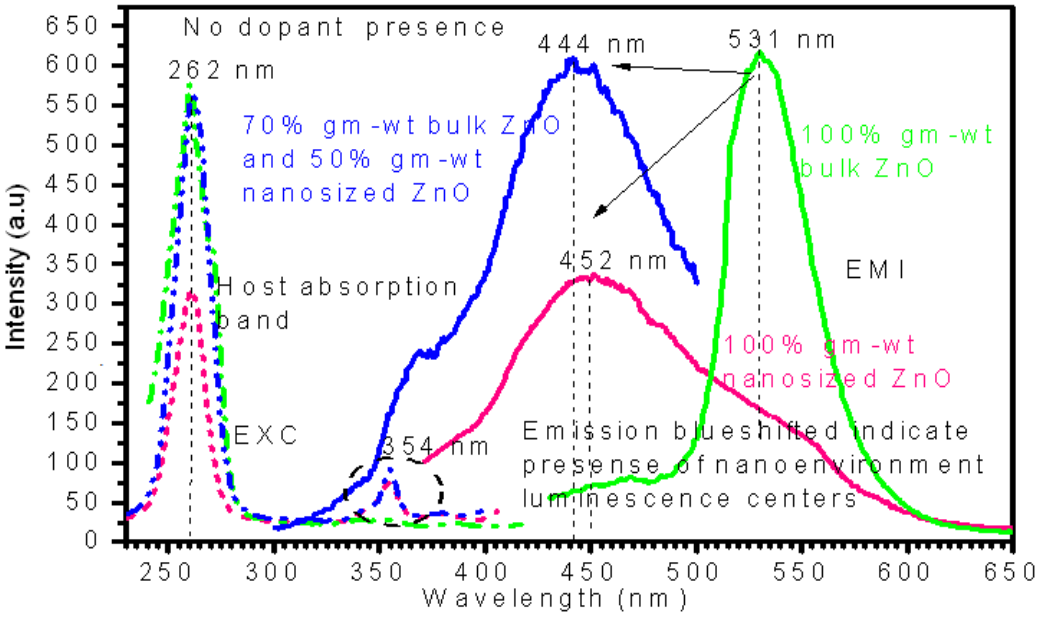

Figure 4.2 EXC and EMI spectras of 3 $CaZnGe_2O_6$ samples with different host compositions

From the optical spectras, it can be clearly seen that with the presence of organic coated luminescence ZnO nanopowder, the obtained phosphor samples have their emission blue-shifted, an indication of presence of nano-environment luminescence centers. The 531 nm host emission is due to presence of luminescence centers within the bulk host $CaZnGe_2O_6$ material. The excitation spectras remain consistent with the host absorption band 262 nm showing for all the three phosphor samples. Due to shallow well trap structure presence in the 100% gm-weight nano ZnO sample, the electrons within the shallow well tend to escape and experience leakage, hence a lower blue emission intensity as compare to the optimized sample made from 70%:50% gm-weight bulk and nano ZnO. It is believed that the optimized sample is a middle-size depth well trap structure with better capacity to entrap more energetic electrons, therefore its blue emission is of higher intensity and matched considerably with the sample made from 100% gm-weight bulk ZnO. The deep well trap structure or sample made from 100% gm-weight bulk ZnO has good electrons trapping storage but its luminescence centers tend to be near the valence band of the host

$CaZnGe_2O_6$ material as compared to the optimized sample, therefore it gives off green emission instead of blue emission. The small protruding 354 nm excitation peak which are only observable from samples made with organic coated luminescence ZnO nanopowder is believed due to the presence of ZnO nanoparticles that have already diffused into the host $CaZnGe_2O_6$ material.

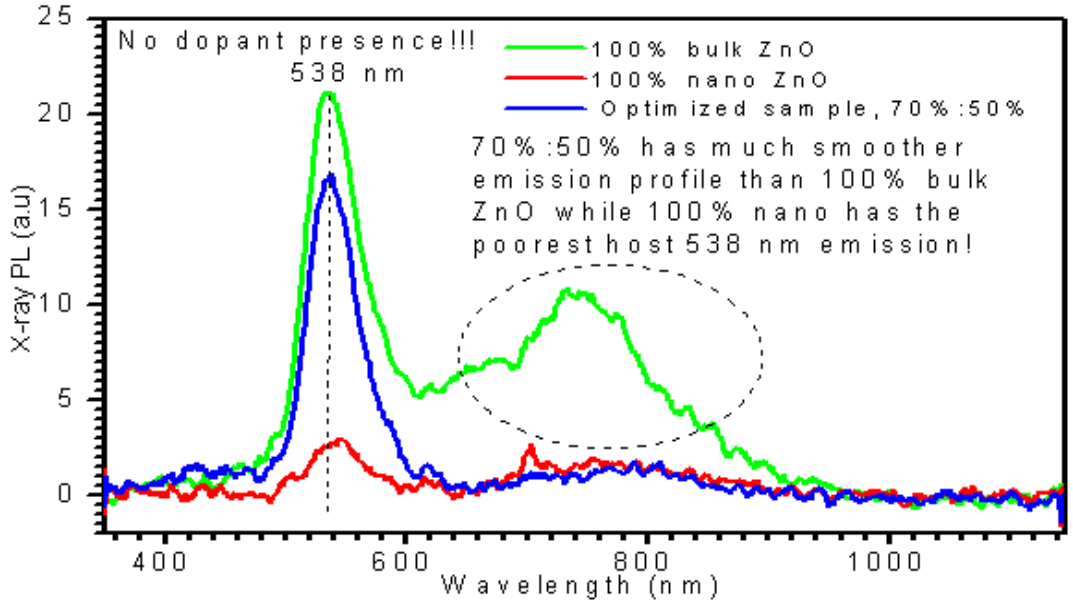

Figure 4.3 X-ray PL of 3 undoped $CaZnGe_2O_6$ phosphor with different host compositions

Figure 4.3 shows us the X-ray photoluminescence data of all 3 undoped samples made from 100% bulk, 100% nano and the optimized 70%:50% bulk and nano ZnO. It is clearly shown that the phosphor sample made from the 100% nano ZnO has the poorest green 538 nm emission, this led us to conclude that the 538 nm emission is due to host material believed to be coming from bulk ZnO. Emission profile from the optimized sample has a better smoother profile than the sample made from 100% bulk ZnO which led us to believe that the optimized sample has minimized lattice defects or impurities that could give rise to the broad infra-red emission as shown by the sample made from 100% bulk ZnO.

4.3.2 $CaZnGe_2O_6:Tb^{3+}$ long afterglow phosphor

In this section, we discuss the experimental results of doping Tb_4O_7 into the host $CaZnGe_2O_6$ material. Figure 4.4 shows us the TEM and EDS data of the sample made from 100% gm-weight nano ZnO. From the TEM images, we could estimate the lattice spacing is ~1 nm which corresponds to [100] and [010] planes. Figure 4.4(e) is the electron diffraction pattern of the [001] zone axis, where the reflection conditions are: $h = 2n$ for $h00$, and $k = 2n$ for $0k0$, where n is an integer. The reflection conditions are consistent to its space group $C2/c$. The EDS data in Figure 4.4(f) clearly shows that terbium atoms have been successfully doped into host $CaZnGe_2O_6$ material.

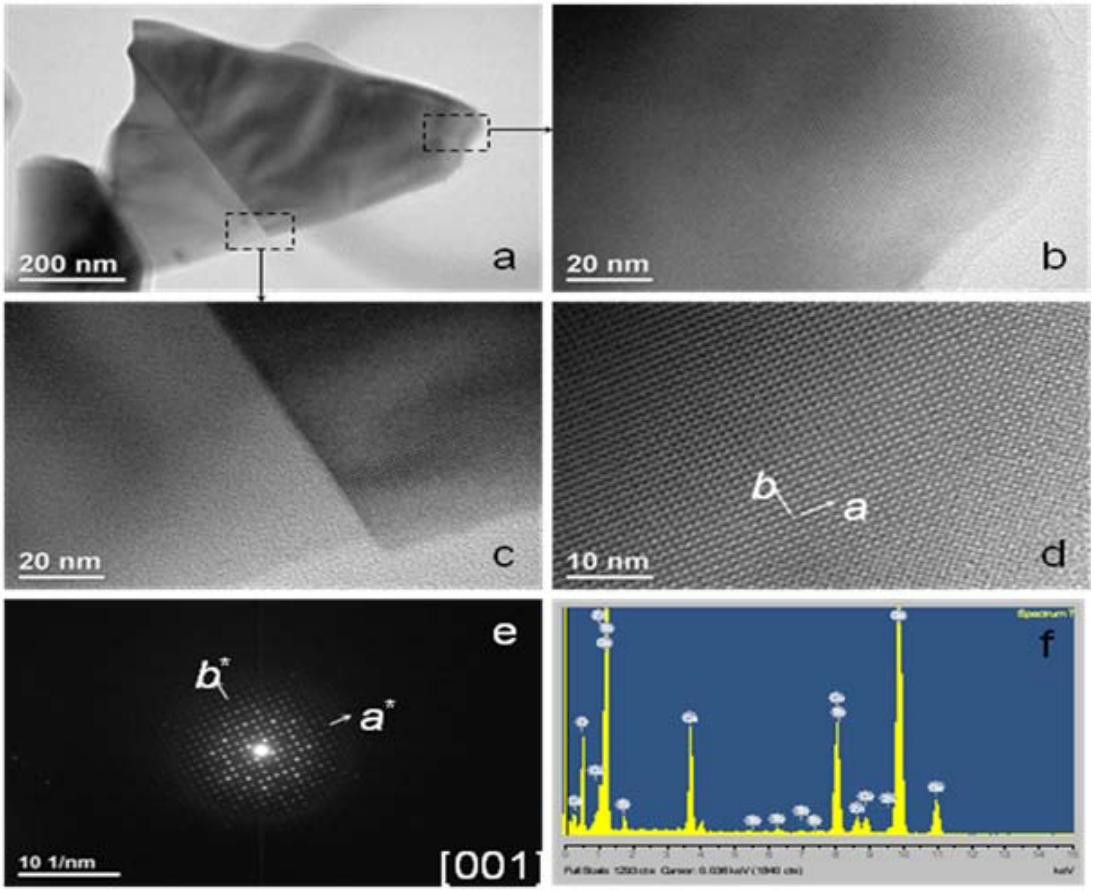

Figure 4.4 TEM/EDP/EDS of $CaZnGe_2O_6:Tb^{3+}$ phosphor with 100% nano ZnO

Figure 4.5 shows us the SEM images of the phosphor sample made from 100% gm-weight nano ZnO in low magnification. It is estimated that the average particle grain size to be around150 m and the largest grain size to be around 250 m.

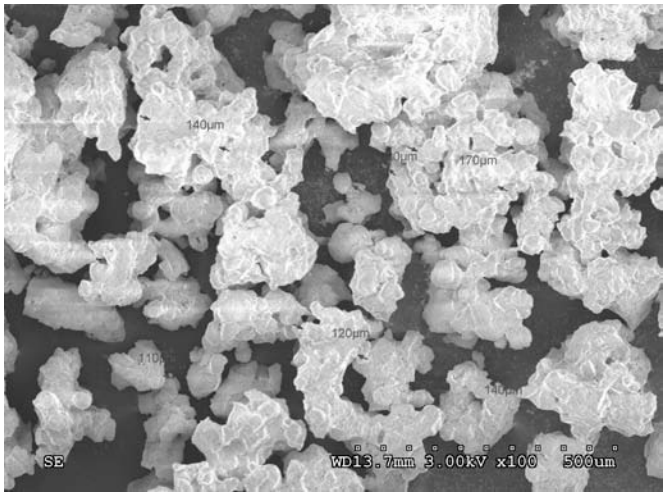

Figure 4.5 SEM of $CaZnGe_2O_6:Tb^{3+}$ phosphor with 100% nano ZnO

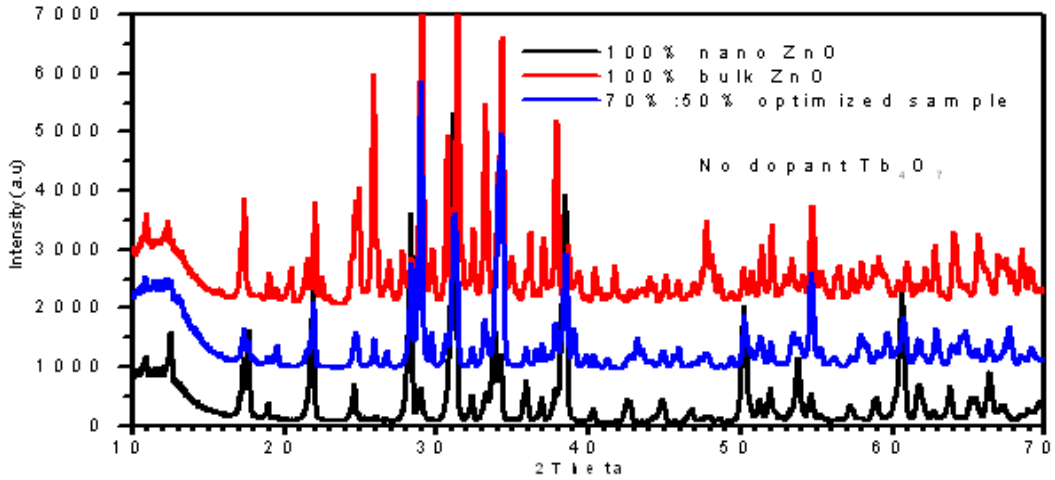

Figure 4.6 XRD of 3 undoped $CaZnGe_2O_6$ phosphor with different host compositions

Figure 4.6 shows us all 3 $CaZnGe_2O_6$ undoped samples, one is made of 100% bulk ZnO, another is made from 100% nano ZnO and finally the 70%:50% gram-weight bulk and nano ZnO optimized host $CaZnGe_2O_6$ material. The data clearly shown that the sample made from 100% bulk ZnO looks messy with lots of diffraction peaks as an indication of deep well

trap structure's presence. The diffracted X-ray beam for this sample has increased path differences due to presence of deep wells' wall structures. Outcoming X-ray beam has high probability of being internally deflected by deep wells' walls, hence more diffracted peaks obtained. Sample made of 100% nano ZnO gives us orderly and clean with less diffraction peaks, an indication of of presence of shallow well trap structures. In this case, the outcoming X-ray beam has small probability of being deflected by shallow wells' walls therefore this sample exhibited much lesser diffraction peaks. The 70%:50% optimized sample shown XRD profile that matched the XRD profile of 100% nano ZnO sample but with some additional diffraction peaks from sample of 100% bulk ZnO, this XRD profile is in consistent with nanocomposite materials. Figure 3.7 shows us the optical properties of the sample made from 100% gm-weight nano ZnO and sample made from 100% gm-weight bulk ZnO.

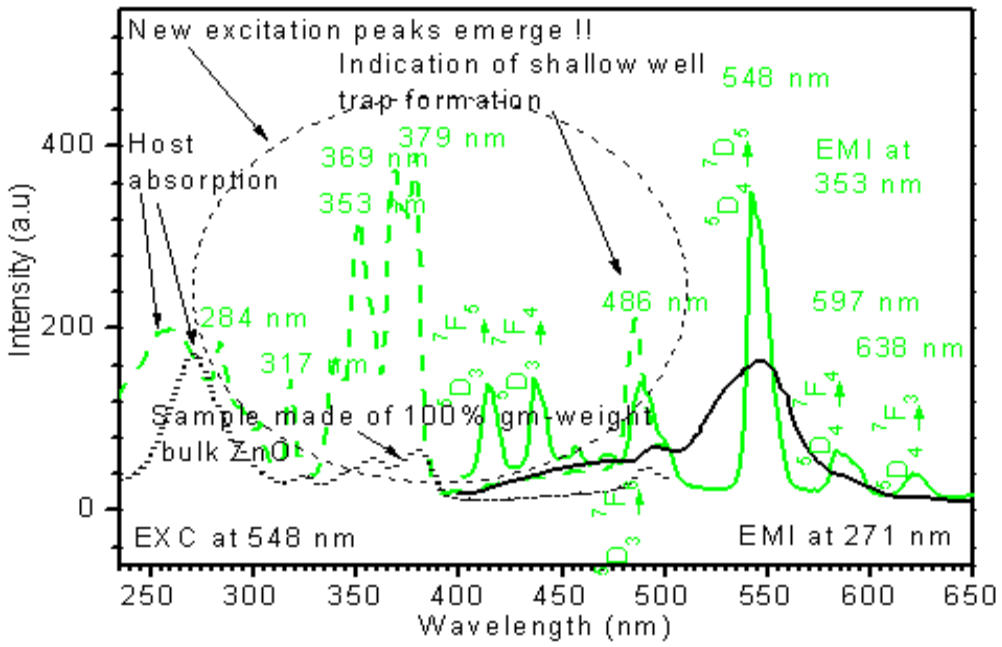

Figure 4.7 EXC and EMI spectras of $CaZnGe_2O_6:Tb^{3+}$ with different host compositions

The excitation spectra for sample made from 100% gm-weight nano ZnO clearly indicate the strongly emergence of some new excitation peaks that are not seen in the sample made

from 100% gm-weight bulk ZnO. We believed that due to the drastic change of the host environment in which the presence of ZnO nanoparticles has caused the host $CaZnGe_2O_6$ material to be more optically transparent under UVA excitation. Crystal field theory strongly dictates that with the terbium dopants being trapped in shallow well trap structure within sample made from 100% gm-weight nano ZnO, its own internal excitation peak that are associated to shallow environment becomes more dominant. The optical properties of these both samples are consistent with observations in which the sample made from 100% gm-weight nano ZnO is more optically active under UVA excitation and exhibits strong photoluminescence behavior with green Tb^{3+} 548 nm as dominant emission while as the sample made from 100% gm-weight bulk ZnO seems to be phosphorescence dominant with the green Tb^{3+} 548 nm emission being stifled by the bulk host material.

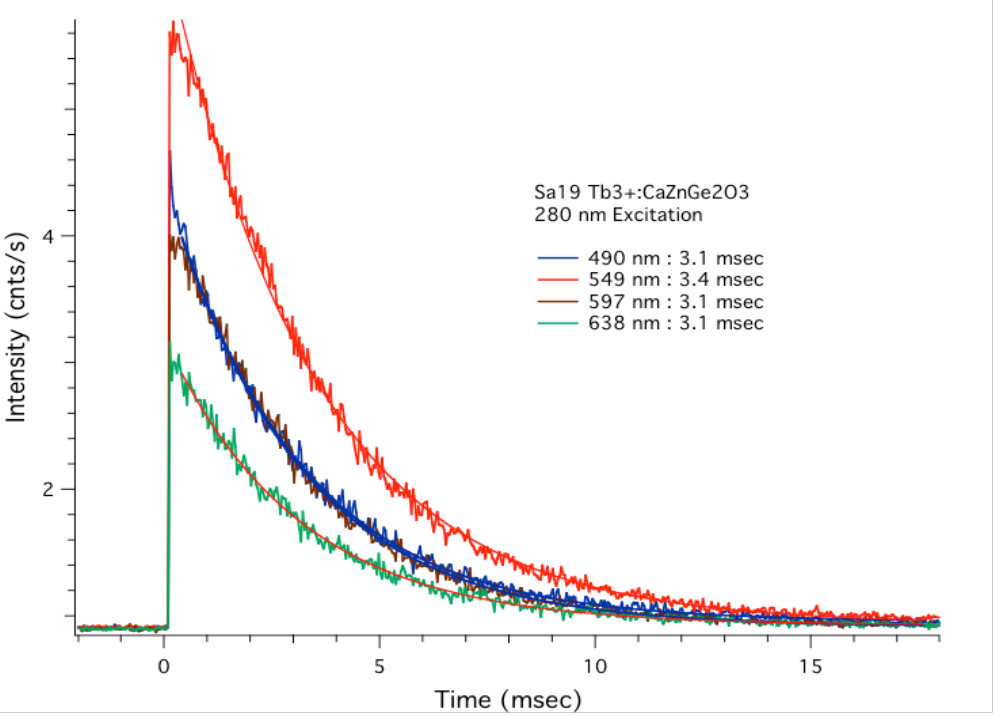

Figure 4.8 Lifetime decay spectras of $CaZnGe_2O_6:Tb^{3+}$ phosphor at 490,549,597,638 nm

Figure 4.8 shows us the lifetime decay of all the four major emission from Tb^{3+}, namely the 549 nm, 490 nm, 597 nm and 638 nm. The results show the lifetime measurements in milliseconds range are to be consistent and agreeable with other literature reported.

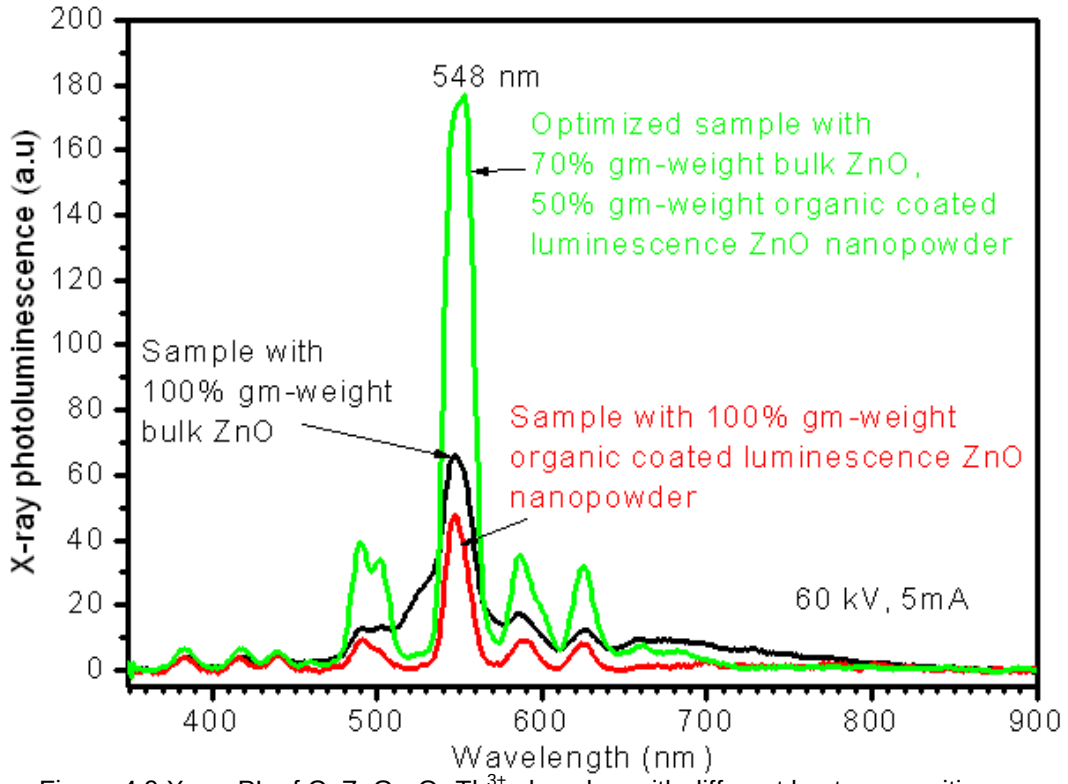

Figure 4.9 X-ray PL of $CaZnGe_2O_6:Tb^{3+}$ phosphor with different host compositions

Figure 4.9 shows us the X-ray photoluminescence for all 3 samples for comparison. The data clearly shown that the optimized sample made with 70%:50% gm-weight bulk and nano ZnO has the best green 548 nm emission and the sample made from 100% gm-weight nano ZnO has the poorest green emission. This can be explained due to the presence of different well trap structure within the samples. For the sample with the weakest green emission under X-ray irradiation, this sample is made from 100% gm-weight nano ZnO tends to have shallow well trap structures with large surface area and have lots of lattice defects, hence the probability of the X- ray light source to penetrate through the host material and exiting without exciting the terbium dopant is high. The optimized sample which has middle-size

depth well trap structures with moderate surface area and minimized lattice defects, increases the probability of X-ray light source to penetrate and excite the terbium dopant hence a far intense green emission is obtained. As for the sample made from 100% bulk ZnO, it tends to have deep well trap structure with small surface area and moderate lattice defects therefore it has a moderate green emission.

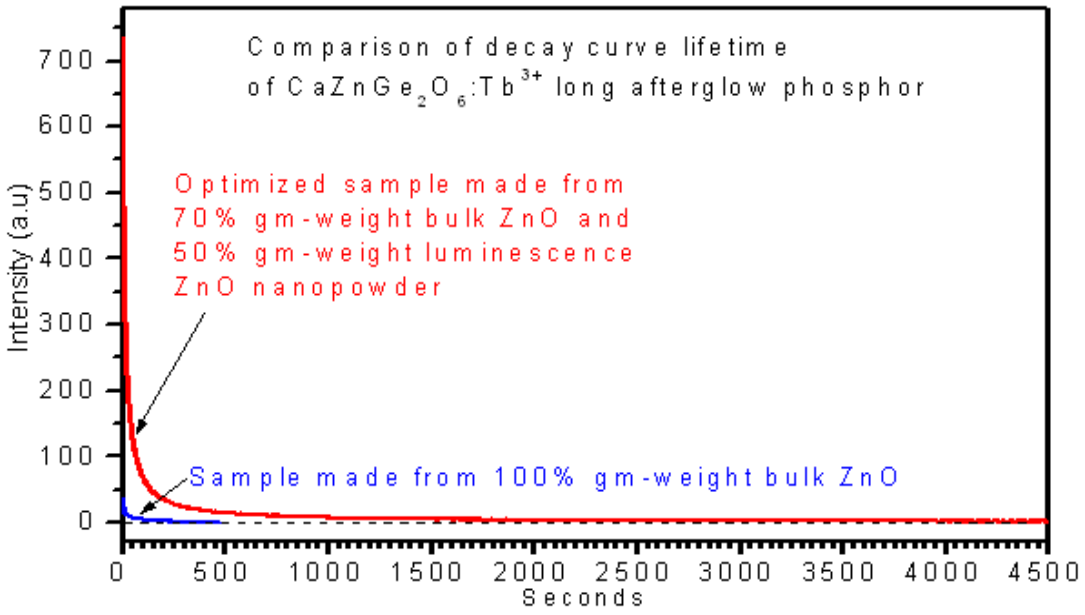

Figure 4.10 Afterglow decay curve of $CaZnGe_2O_6:Tb^{3+}$ with different host compositions

Figure 4.10 shows us the afterglow decay curve of two samples, the optimized sample and sample made from 100% gm-weight bulk ZnO under 4 minute expose of mercury lamp (254 nm). Sample made from 100% gm-weight nano ZnO is put in for comparison since it has the poorest afterglow decay curve. Under proper observation, it can be readily verified that the optimized sample may have its afterglow extends even to at least 3 hours. The results clearly shown that phosphorescence characteristics can be optimized by utilizing a combination of both bulk and nanosized ZnO materials.

4.4 Conclusions and Summary

$CaZnGe_2O_6$ phosphors were fabricated with dopant Tb_4O_7 and without dopant and their optical properties were investigated. Host $CaZnGe_2O_6$ material is believed to be a self-activated material in which it gives us, a green emission 538 nm and green afterglow. This is due to internal lattice defects built within the host material and its own luminescence centers. With the introduction of organic coated luminescence ZnO nanopowder, it makes the host material to become more optically transparent and active under UVA 350 nm excitation. The introduction of terbium dopant causes the electrons in valence pool tend to be excited through terbium's unfilled energy levels into the conduction band rather than through the host material's energy levels in which the electrons could move and get themselves entrapped in the electron traps. Upon released from the traps due to thermal agitations, the electrons tend to return ground state via terbium's unfilled energy levels, hence giving the green 543 nm emission. Figure 4.11 illustrates the phosphorescence mechanics of $CaZnGe_2O_6:Tb^{3+}$ phosphor.

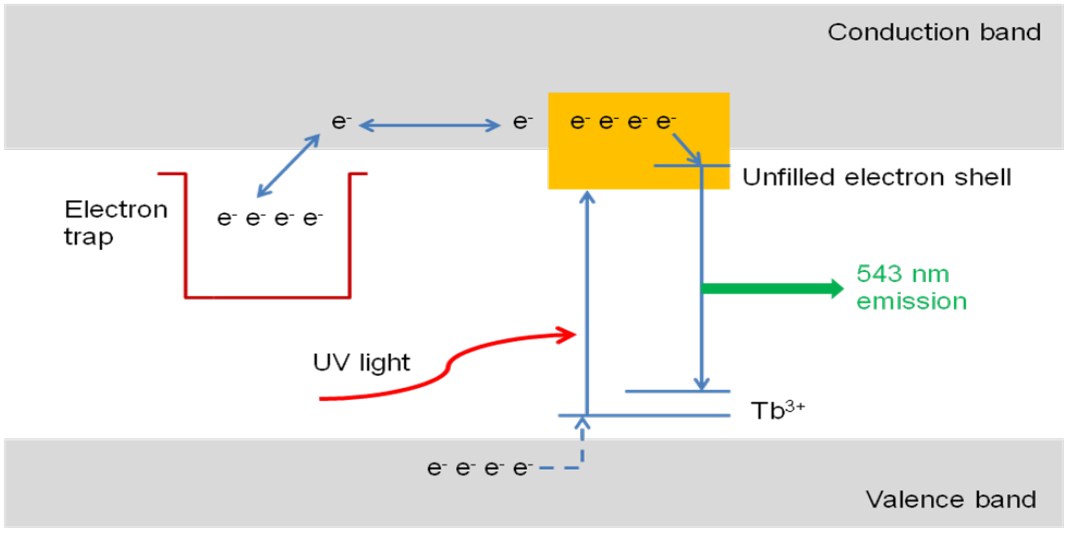

Figure 4.11 Phosphorescence mechanics of $CaZnGe_2O_6:Tb^{3+}$ phosphor

The actual ZnO mass that was used in reality for organic coated luminescence ZnO was only 25.5% of the total gm-weight in which the remaining 74.5% of the total weight comes

from the organic layer. Therefore the optimized sample consists of 70%:50% gm-weight bulk ZnO and nano ZnO has only 0.2828 gm, which is short of the proper stoichiometric value of 0.342 gm. The missing ZnO's mass (17.3%) is responsible for creating the inter-layer structure defect or minimized lattice defects that are responsible for long afterglow effects. In order to prove that the optimized sample's bottom has more nanosized ZnO than bulk ZnO material, we tested two different optimized samples annealed at 1100℃ for an hour and another at 3 hours. Figure 4.12 shows us the X-ray PL of these two samples measured from their top and bottom layers' perspective.

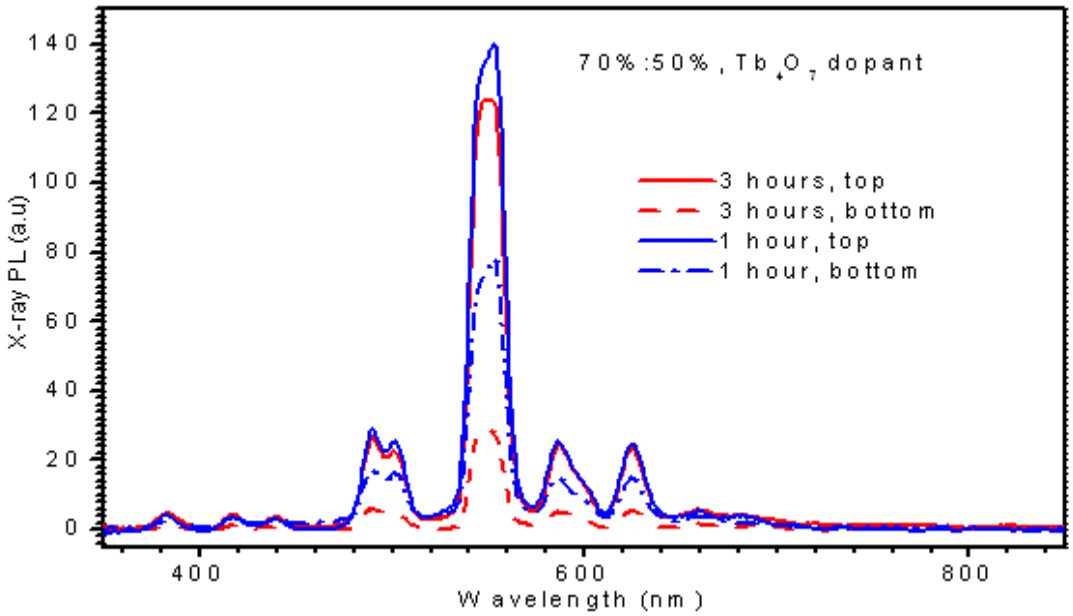

Figure 4.12 X-ray PL of $CaZnGe_2O_6:Tb^{3+}$ at different positioning and anneal duration

The results clearly shown that by introducing 50% gm-weight nano ZnO, more of these ZnO nanoparticles will find their way to settle at the bottom of the well trap structures leaving most of the bulk ZnO to form the well traps' walls and more lattice defects or void gap to form at the top of well trap structures. Therefore the X-ray PL of the top layers for both samples are more intense than the bottom layers due to the ease of X-ray light source penetrating through the void gap layers and exciting the exposed terbium dopants. Another way to visualize the internal host lattice structure of this phosphor material, is to imagine that the

sample composed of 100% bulk ZnO material has deep well trap structures, sample composed of 100% nano ZnO has shallow well trap structures, the 70% bulk :50% nano ZnO sample has middle-depth well trap structures in which most of diffused ZnO nanoparticles can be found at the bottom layers.

CHAPTER 5

SINGLY DOPANT STUDIES IN HOST $CaZnGe_2O_6$ PHOSPHOR

5.1 Introduction

In this chapter, we conducted survey studies on other singly dopants to be doped into the 70%:50% gram-weight bulk and nano ZnO optimized host $CaZnGe_2O_6$ phosphor. By doing this survey studies, we hope to understand the phosphorescence mechanism and its relation with photoluminescence observations and also the relations of the dopant's orbital electrons with its host well trap structure. The optical properties of the doped phosphor material could be easily deduced based on its ionic radius and the sites in which they occupy, either the cation vacancy sites or the interstitial sites (well trap sites).

5.2 Experimental details

The experiment parameters are as the same as in Chapter 4 but we decided to put in other singly dopants into the optimized well trap structure made from 70%:50% gram-weight bulk and nano ZnO for our survey study. The singly dopant concentration is kept at 0.16 mmole in consistent with dopant Tb_4O_7's concentration used in pinning down the 70%:50% optimized sample. The X-ray photoluminescence data are obtained at 60 kV,5 mA after a standard reference sample is measured for set-up calibration.

5.3 Results and Discussions

5.3.1 Mn^{2+}, Mn^{2+}/Mn^{3+}, Mn^{3+}, Mn^{4+}

Figure 5.1 shows us the optical properties of 70%:50% gram-weight bulk and nano ZnO optimized samples doped with Mn^{2+}. The data clearly shown that Mn^{2+} has its active 3d

orbital electrons that are responsible to be donated and avalanched onto the electron pool of the valence band which are then excited either through direct excitation (broad 314 nm band) or indirect excitation through host absorption band of 260 nm to give us the green 535 nm emission in which the luminescence centers for this emission is believed due to the host $CaZnGe_2O_6$ material. Since ionic radius for Mn is 67 pm, then it is believed that this dopant will probably occupy the interstitial sites or well trap sites. Meanwhile the $CaZnGe_2O_6$ phosphor sample composed of 100% bulk ZnO doped with Mn^{2+} will have Mn^{2+} dopants to occupy cation vacancy sites within the host matrix (Zn^{2+} and/or Ca^{2+}) as this sample exhibits a much stronger broad Mn^{2+} absorption band centering around 316 nm than the host absorption band of 264 nm.

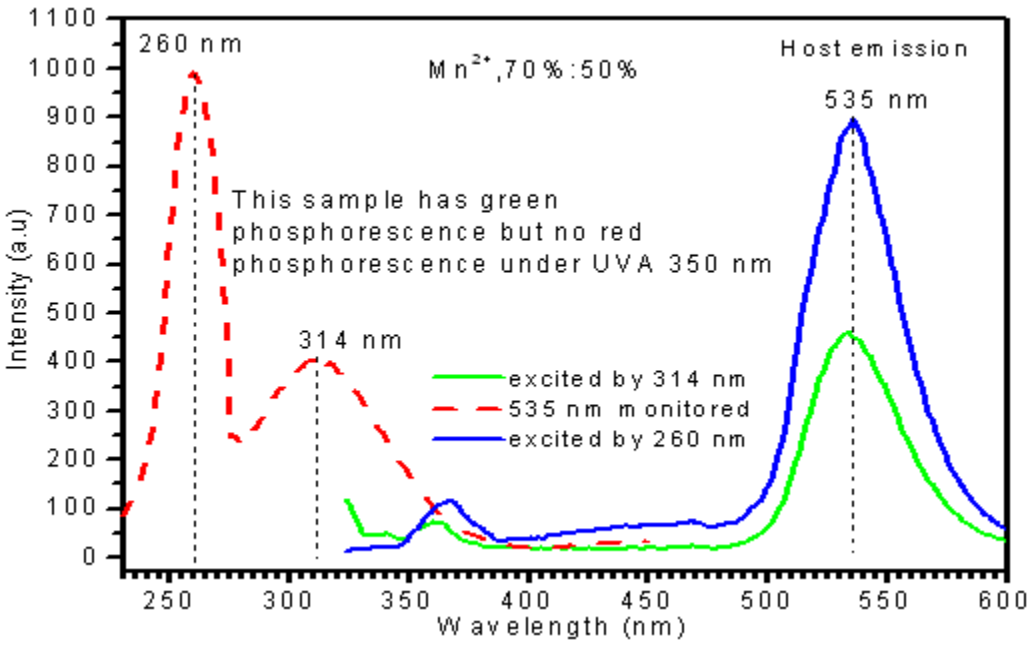

Figure 5.1 Excitation and Emission spectras of $CaZnGe_2O_6$:Mn^{2+} (70%:50% ZnO)

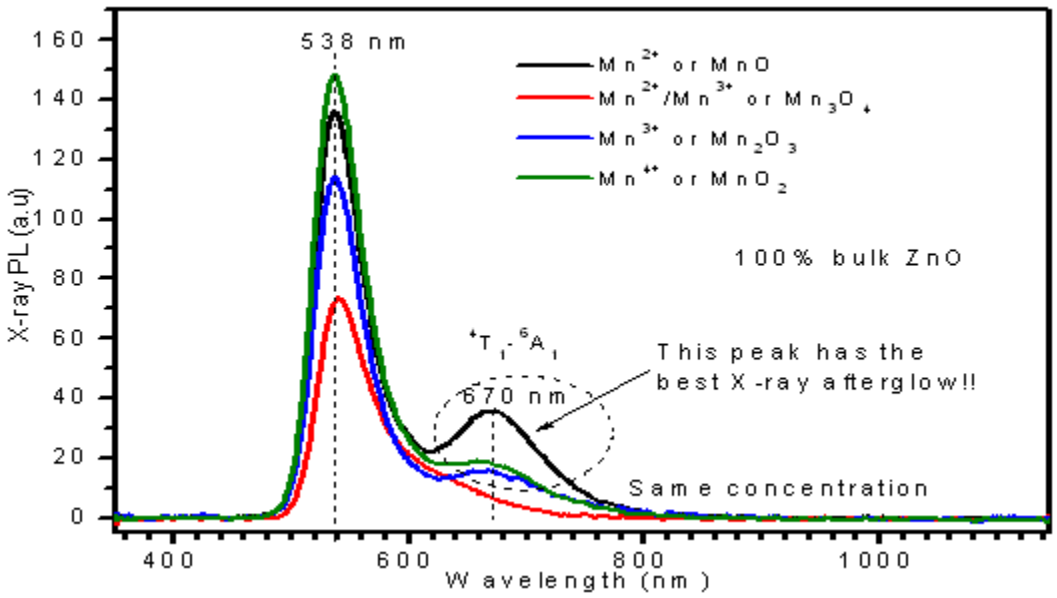

Figure 5.2 X-ray PL of Mn-doped $CaZnGe_2O_6$ (100% bulk ZnO)

Figure 5.2 shows us the X-ray PL of all manganese family as dopants into the host $CaZnGe_2O_6$ material made from 100% gram-weight bulk ZnO. The data clearly shown that Mn^{2+} is the most reactive dopant in which it has the more optically active 3d orbital electrons that are responsible for the 670 nm red emission band. Both samples doped with Mn^{2+} that are made of 100% gram-weight bulk ZnO and 70%:50% gram-weight bulk and nano ZnO exhibit green emission under UVB 250 nm illumination but only sample made of 100% gram-weight bulk ZnO exhibits green emission and red afterglow phenomena under both UVA 350 nm and UVB 250 nm illuminations. As for photoluminescence comparison, sample doped with Mn^{2+}/Mn^{3+} that is made of 100% bulk ZnO has the most intense green 538 nm emission however this sample has non-existent red afterglow as compared with samples doped with Mn^{2+}, Mn^{3+} and Mn^{4+} with host material consists of 100% gram-weight bulk ZnO. This phenomena can be explained in which Mn^{2+}/Mn^{3+} has their 3d orbital stretches out more horizontally than Mn^{2+}, Mn^{3+} and Mn^{4+}.

5.3.2 Sm^{3+}, Eu^{3+}, Dy^{3+}, Tm^{3+}

Figure 5.3, 5.4, 5.5 and 5.6 shown the optical properties of these 4 dopants doped into 70%;50% optimized sample that give us photoluminescence emission but with no phosphorescence effects. They are Sm^{3+}, Eu^{3+}, Dy^{3+} and Tm^{3+} in which red, white and blue emissions were observed. The main reason that photoluminescence emission is dominant for these dopants and not the phosphorescence is due to the fact, there is no available 4f-5d excitation peak that overlap or close to the host absorption band. Moreover, since all these 4 rare earth dopants have ionic radius greater than 100 pm, then it is believed, they all occupies the interstitial sites (well trap sites).

Figure 5.7 shown the X-ray PL of all these 4 dopants (Sm^{3+}, Eu^{3+}, Dy^{3+} and Tm^{3+}) in 70%:50% gram-weight bulk and nano ZnO optimized sample. All the host green 538 nm emission and the respective dopants' dominant emission peaks were seen with the exception of Tm^{3+}'s blue 458 nm emission. This led us to believe for host $CaZnGe_2O_6$ material, under X-ray irradiation, any dopant's blue luminescence centers is quenched completely leaving only the host green emission to be observed. The main reason is due to host material, the bulk GeO_2 material plays an important role in absorbing most of the energetic X-ray beams rather than the ZnO nanoparticles. We also investigated the influences of organic coated luminescence ZnO nanopowder on the host $CaZnGe_2O_6$ material doped with Sm^{3+}.

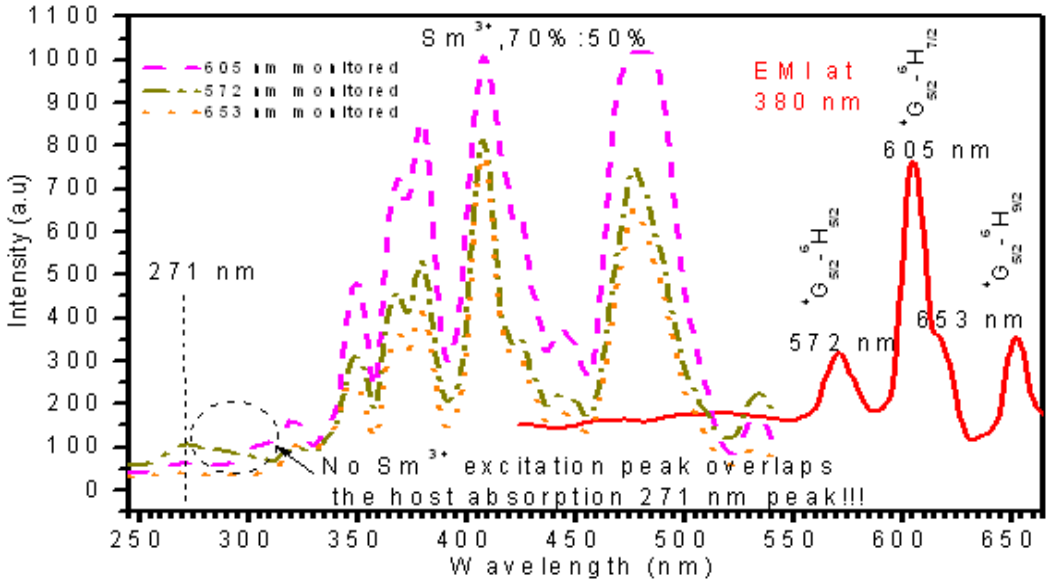

Figure 5.3 Excitation and Emission spectras of $CaZnGe_2O_6:Sm^{3+}$ (70%:50% ZnO)

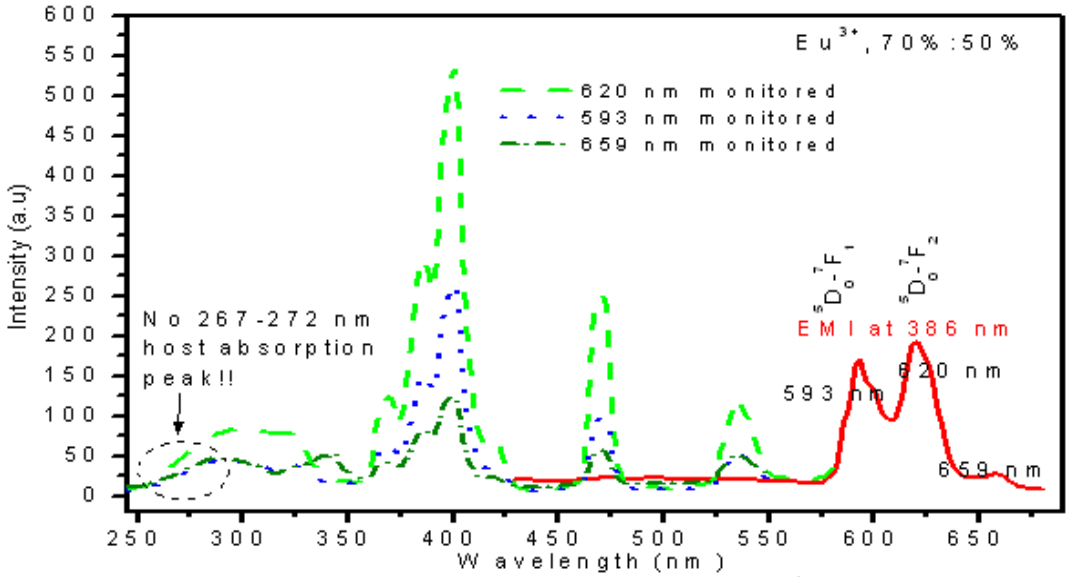

Figure 5.4 Excitation and Emission spectras of $CaZnGe_2O_6:Eu^{3+}$ (70%:50% ZnO)

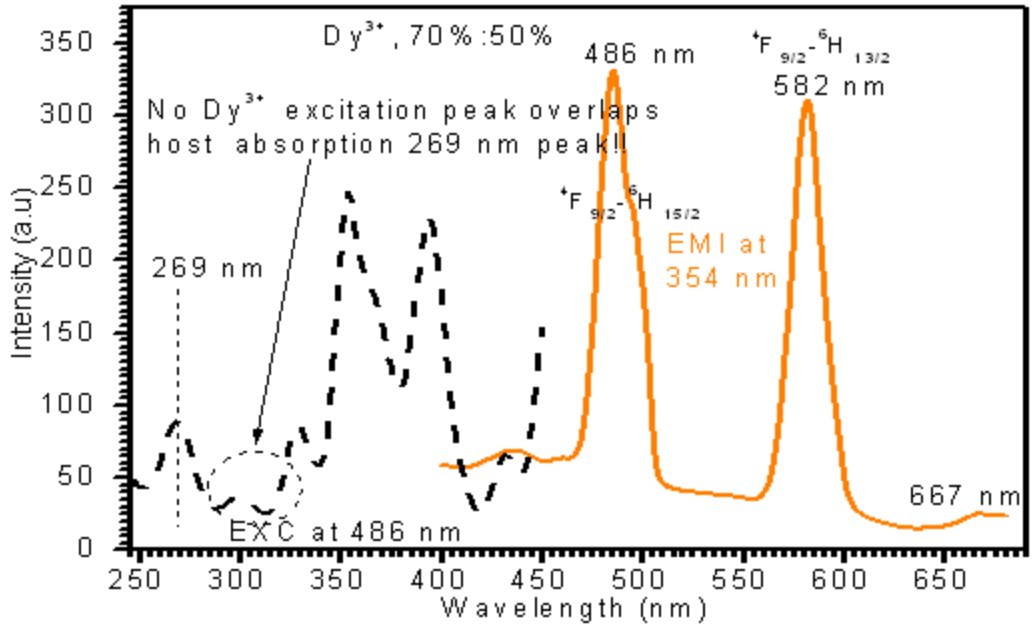

Figure 5.5 Excitation and Emission spectras of $CaZnGe_2O_6:Dy^{3+}$ (70%:50% ZnO)

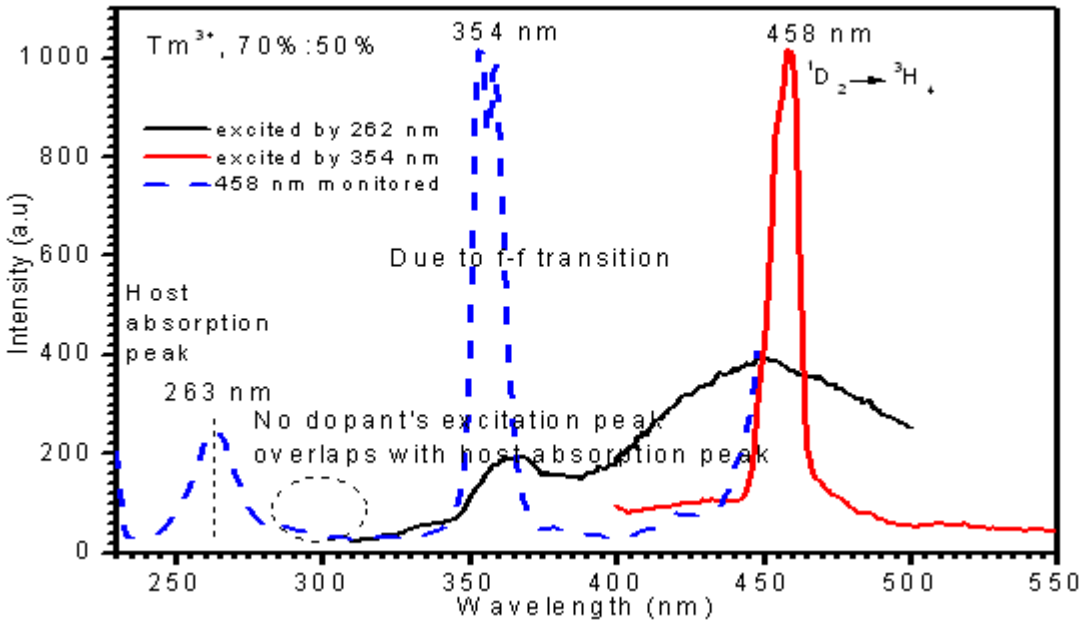

Figure 5.6 Excitation and Emission spectras of $CaZnGe_2O_6:Tm^{3+}$ (70%:50% ZnO)

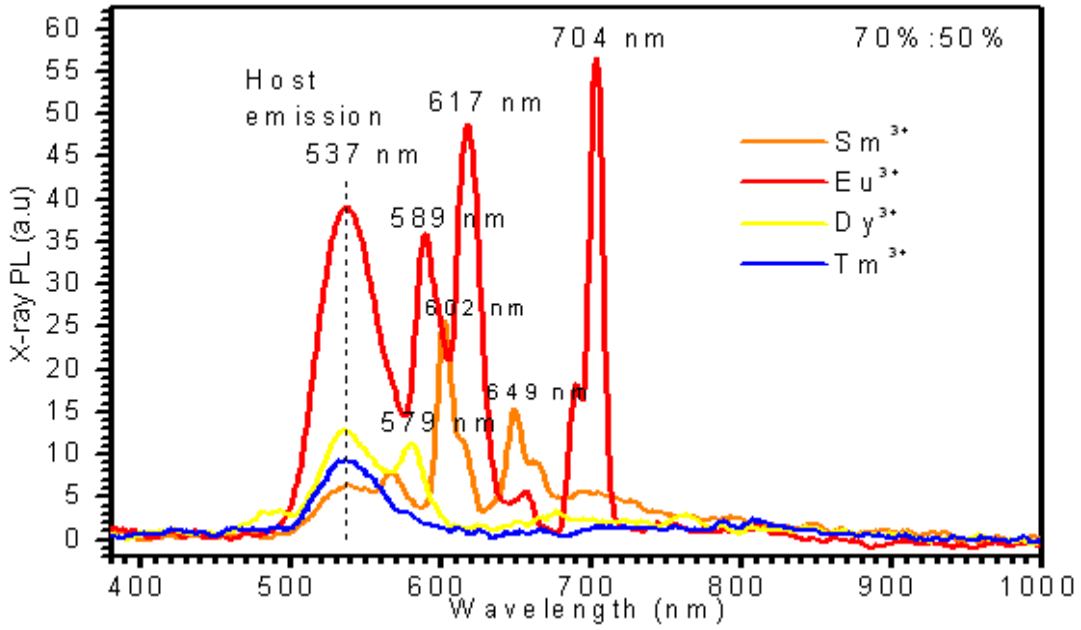

Figure 5.7 X-ray PL of Sm^{3+},Eu^{3+},Dy^{3+},Tm^{3+}-doped $CaZnGe_2O_6$ (70%:50% ZnO)

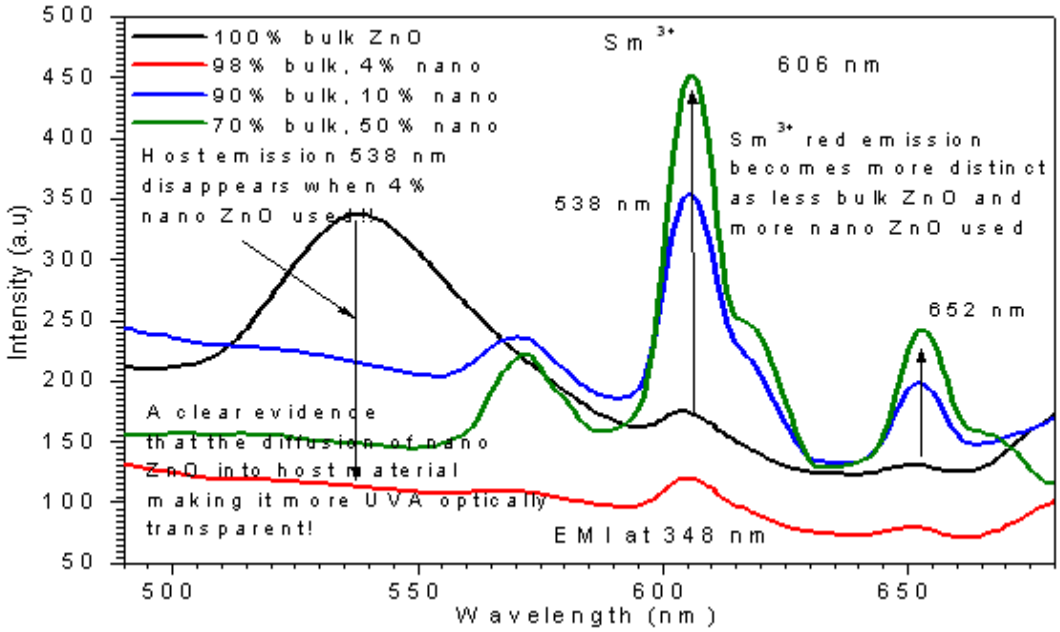

Figure 5.8 Emission spectras of $CaZnGe_2O_6$:Sm^{3+} with different host compositions

Figure 5.8 clearly shown us that by introducing a mere 4% gram-weight nano ZnO, the obtained sample changes drastically to become more optically active under UVA 350 nm illumination in which the red emission of Sm^{3+} becomes more dominant and the

disappearance of the host green luminescence centers. As more nano ZnO and less bulk ZnO are used, the samples tend to show a better distinct and re-emergence of red Sm^{3+}'s emission. This is another important experimental proof that by adding the ZnO nanoparticles, the resultant is that the bulk host material becomes more optically transparent because the original organic coated ZnO nanoparticles in mother solvent ethanol are in transparent form to start with.

5.3.3 Ce^{4+}, Pr^{3+}, Nd^{3+}, Ho^{3+}, Er^{3+}, Yb^{3+}, Lu^{3+}

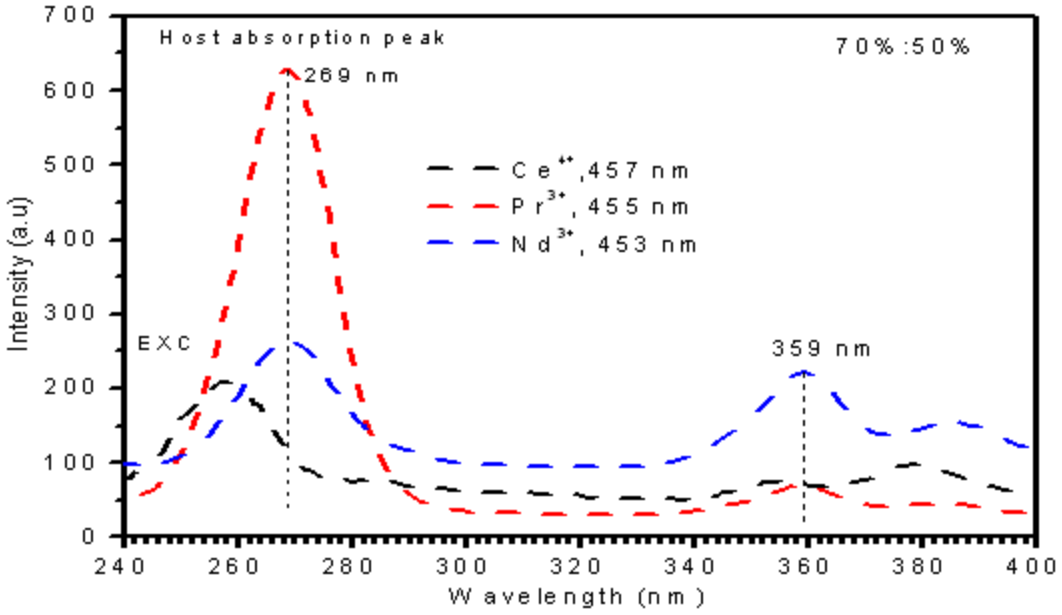

Figure 5.9 Excitation spectras of Ce^{4+},Pr^{3+},Nd^{3+} -doped $CaZnGe_2O_6$ (70%:50% ZnO)

It is well-known fact that for rare earth dopants which have their partially filled 4f shell to be shielded from surrounding influences by 5s and 5p shells. Figure 5.9 and 5.10 show us the optical properties of the host material when doped with other 7 rare-earth dopants into the optimized 70%:50% gram-weight bulk and nano ZnO optimized sample. It can be clearly seen all these 7 dopants did not contribute any special emission on its own, but retains largely the blue emission around 455 nm in which it is slightly red-shifted when compares with undoped 70%:50% gram-weight bulk and nano ZnO optimized sample in Chapter 4.

The host absorption peak remain around 265-270 nm for all 7 rare-earth dopants and strange enough, only Ho^{3+} displays two blue emissions, 442 nm and 472 nm in which one of them is believed to be due to Ho^{3+} as luminescence centers. There is also a possibility that for Ho^{3+} case, these dopants could occupy two possible sites within this phosphor material, the cation vacancy sites within the host matrix and the interstitial sites (well trap sites). However only Er^{3+} (100 pm) seems to be the least optically active in which the host luminescence centers are believed to be quenched by them.

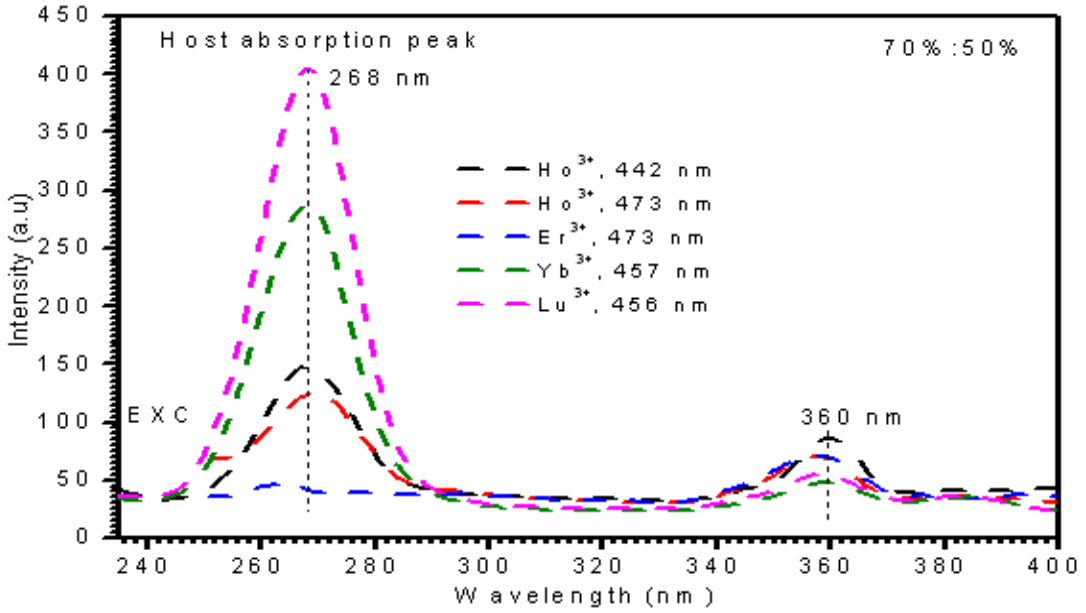

Figure 5.10 Excitation spectras of Ho^{3+},Er^{3+},Yb^{3+},Lu^{3+}-doped $CaZnGe_2O_6$ (70%:50% ZnO)

Figure 5.11 shows us the X-ray PL of all the respective 7 rare-earth dopants in 70%:50% gram-weight bulk and nano ZnO optimized sample. All the 7 rare-earth dopants still give us the usual host green 538 nm emission but with the exception of Ho^{3+}, in which it gives us two green emission, 528 nm and 553 nm. Only Nd^{3+} (114 pm) and Yb^{3+} (99 pm) give us, beside the host emission, its own infra-red emission centering on 911 nm and 978 nm. Lu^{3+} (98 pm) is believed to be occupying the calcium vacancy sites within the host matrix, thus it contributes to luminous blue emission and afterglow. Ce^{4+} (114 pm) is believed to be

occupying the interstitial sites (well trap sites) but due to its stable electronic configuration [Xe], therefore this dopant has no interesting optical properties.

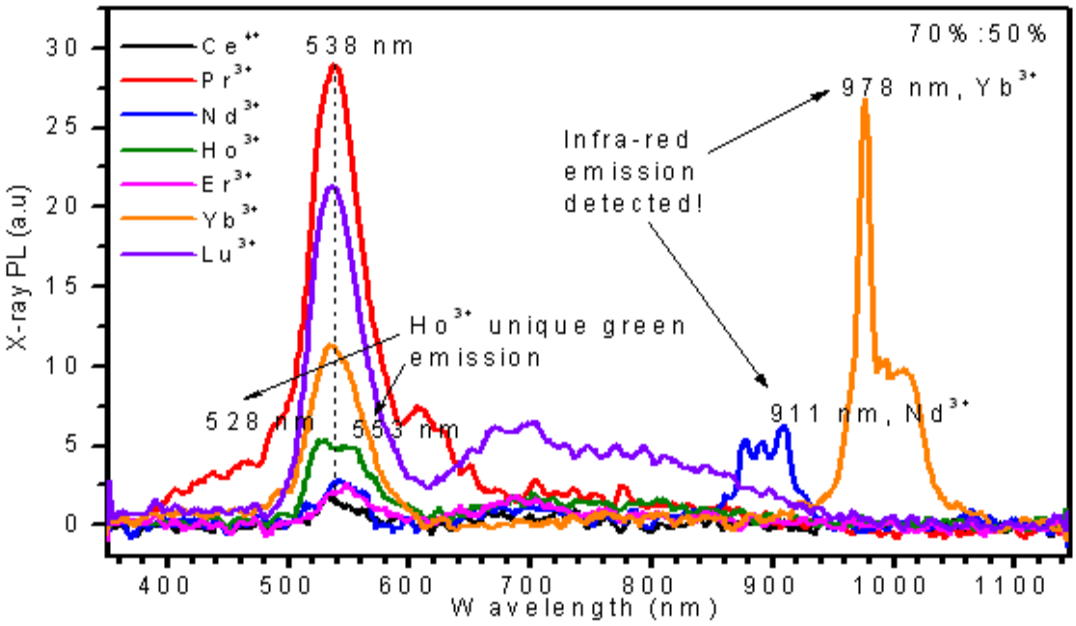

Figure 5.11 X-ray PL of Ce^{4+},Pr^{3+},Nd^{3+},Ho^{3+},Er^{3+},Yb^{3+},Lu^{3+}-doped $CaZnGe_2O_6$ (70%:50%)

5.3.4 Ga^{3+}, In^{3+}, Sb^{3+}, Bi^{3+}

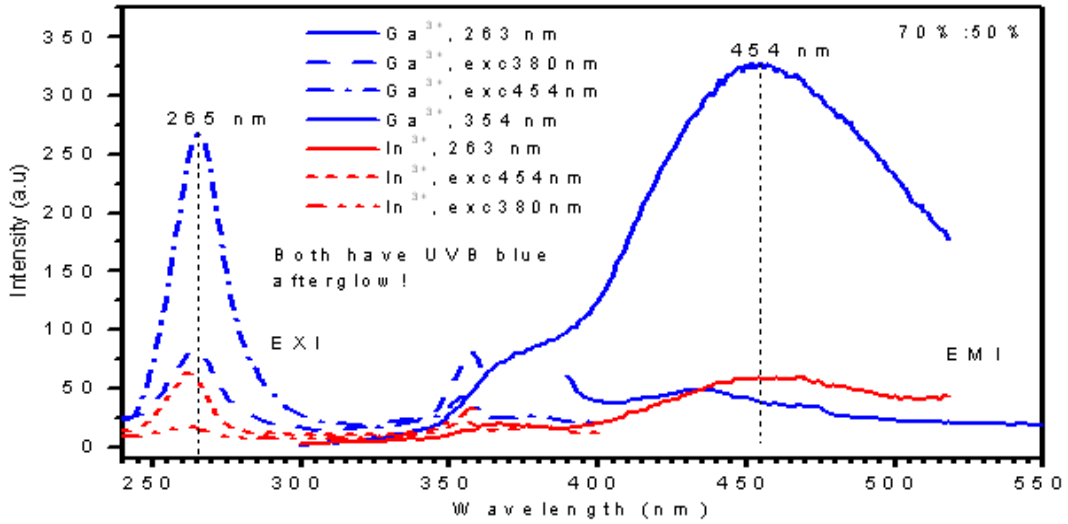

Figure 5.12 Excitation and Emission spectras of Ga^{3+},In^{3+} -doped $CaZnGe_2O_6$ (70%:50%)

Figure 5.12 shows us the optical properties of two dopants from the group IIIA, Ga^{3+} and In^{3+} singly doped into the 70%:50% gram-weight bulk and nano ZnO optimized sample. The figure clearly shows that only Ga^{3+} gives us the most intense blue emission and blue afterglow. This blue afterglow is due to dopant Ga^{3+} (62 pm) being integrated within the host matrix instead of residing within the well-trap structures. Ga^{3+} acts to provide hole trap by occupying the Zn and Ca vacancy sites. Figure 5.13 shows us the optical properties of Sb^{3+} and Bi^{3+} singly doped into 70%:50% host material. It can be seen clearly both dopant emit UV emission due to the transition $^3P_1$-$^1S_0$. The 266 nm broad peak is believed due to host absorption peak and the 300 nm and 294 nm due to charge transfer state from O^{2-} to the respective dopants or possibly, the dopant's absorption themselves.

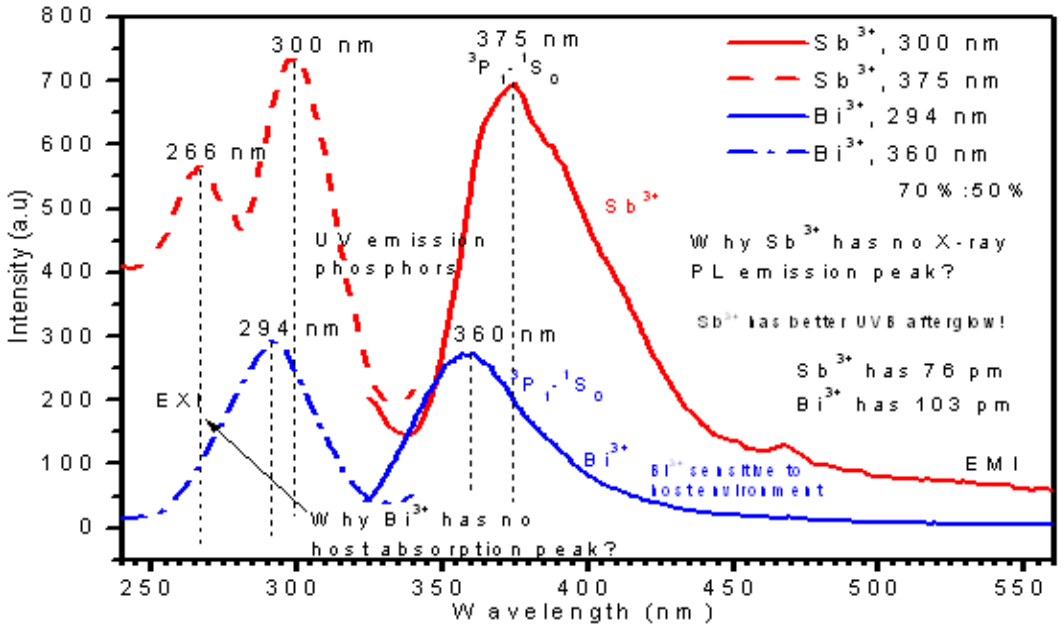

Figure 5.13 Excitation and Emission spectras of Sb^{3+},Bi^{3+} -doped $CaZnGe_2O_6$ (70%:50%)

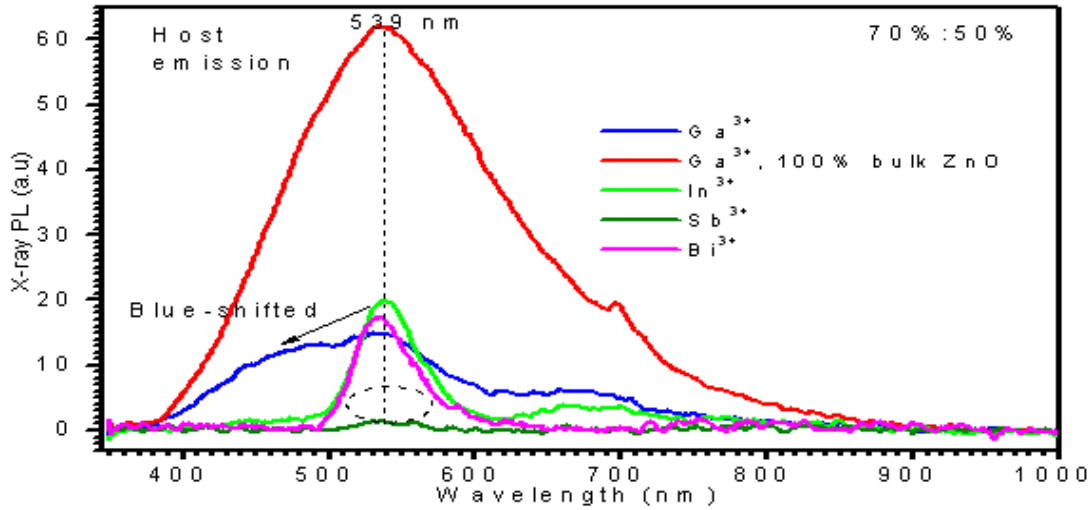

Figure 5.14 X-ray PL of Ga^{3+},In^{3+},Sb^{3+},Bi^{3+}-doped $CaZnGe_2O_6$ (70%:50% and 100% bulk)

Figure 5.14 shows us the X-ray PL of the 4 dopants, Ga^{3+}, In^{3+}, Sb^{3+} and Bi^{3+} in the 70%:50% gram-weight bulk and nano ZnO optimized sample. The introduction of dopant Ga^{3+} clearly caused the host emission of the material to be blue-shifted as demonstrated by the sample made from 100% bulk ZnO, in which it has broader emission peak as compare to other dopants. As usual, the presence of more bulk ZnO serves to strengthen and heighten

the host green 538 nm emission. Only Sb^{3+} remains the most optically inert among the rest of these dopants because both of their excitation peaks 266 nm and 300 nm which gives 375 nm emission, is forbidden under X-ray irradiation since it involves ZnO nanoparticles (has zero tolerance and zero energy capacity towards X-ray energies) to absorb more energetic X-ray energies than the bulk host material, ZnO (Photoluminescence) and GeO_2(afterglow). Moreover, the bulk host material absorption of X-ray energies prefer to emit at lower energy around 535 nm (host green emission) which does not correspond well with the 375 nm emission emitted comfortably by both the host absorption and Sb^{3+}'s absorption under UV illumination. Due to the fact that both nano ZnO and host bulk material conditions cannot be fulfilled, hence we cannot observe any X-ray PL coming from $CaZnGe_2O_6$:Sb^{3+} phosphor (70%:50% ZnO).

5.3.5 Mg^{2+}, Ti^{4+}, Cr^{3+}, Fe^{2+}

Figure 5.15 shows us the optical properties of host $CaZnGe_2O_6$ material when doped with dopant Mg^{2+}, Ti^{4+}, Cr^{3+} and Fe^{2+} into the 70%:50% gram-weight bulk and nano ZnO optimized sample. Cr^{3+} (62 pm) sample is not featured here it has non-optically active electrons under both UVA 350 nm and UVB 250 nm illumination and this sample appears in grain greenish colors. Only Ti^{4+} sample has its host absorption peak blue-shifted to 239 nm instead of the usual 268 nm. All 4 doped samples as usual display blue emission.

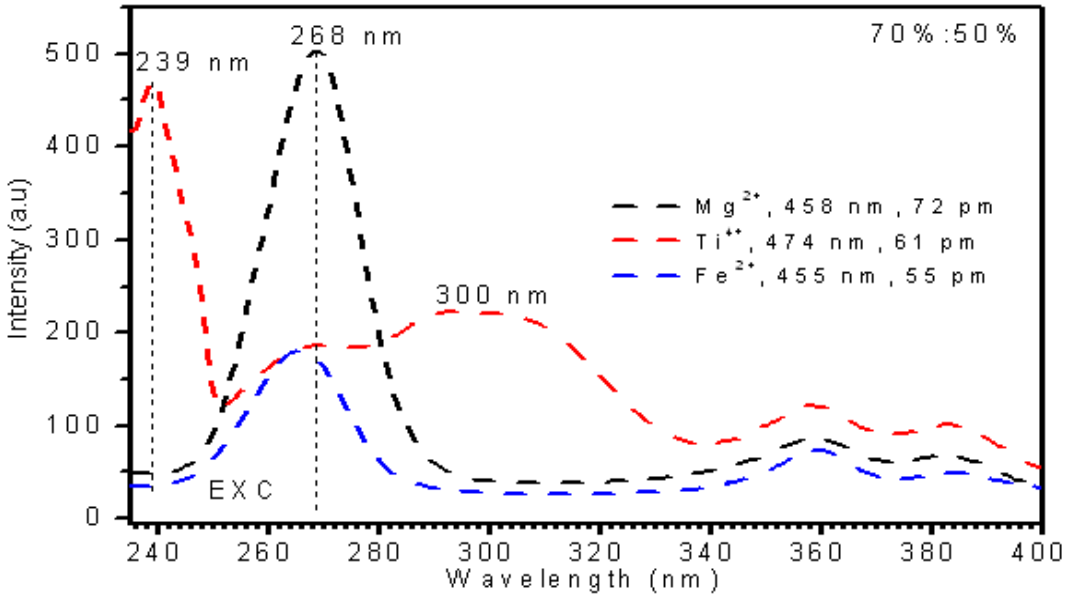

Figure 5.15 Excitation spectras of Mg^{2+},Ti^{4+},Fe^{2+} -doped $CaZnGe_2O_6$ (70%:50% ZnO)

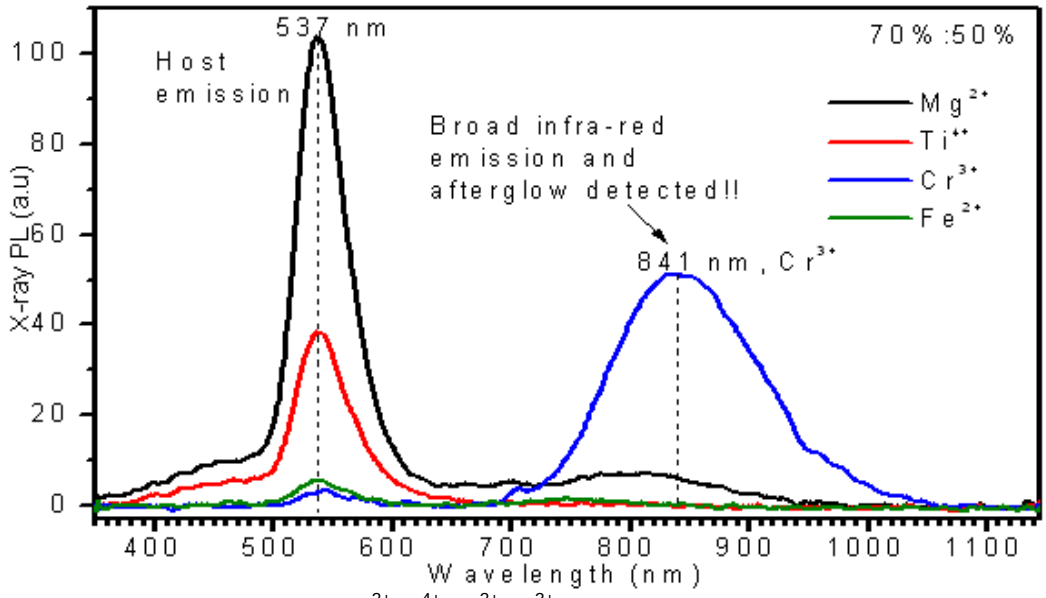

Figure 5.16 X-ray PL of Mg^{2+},Ti^{4+},Fe^{2+},Cr^{3+} -doped $CaZnGe_2O_6$ (70%:50% ZnO)

Figure 5.16 shows us the X-ray PL of 70%:50% gram-weight bulk and nano ZnO optimized samples doped with dopant Mg^{2+}, Ti^{4+}, Cr^{3+} and Fe^{2+}. Most doped samples still exhibit the

usual green 538 nm host emission in which Fe^{2+} has the poorest emission. Only Cr^{3+} doped sample has a broad infra-red emission and afterglow centering on 841 nm.

5.3.6 Co^{2+}, Ni^{2+}, Cu^{2+}

In this last section, we explored the effect of these 3 dopants doped into the 70%:50% gram-weight bulk and nano ZnO optimized samples. All these 3 doped samples exhibit very poor optical properties in which there is non-existent emission or a “dead zone” coming from them. These dopants are well known as luminescence centers quenchers. This is further verified when we measured theirs X-ray PL’s properties as shown in Figure 5.17.

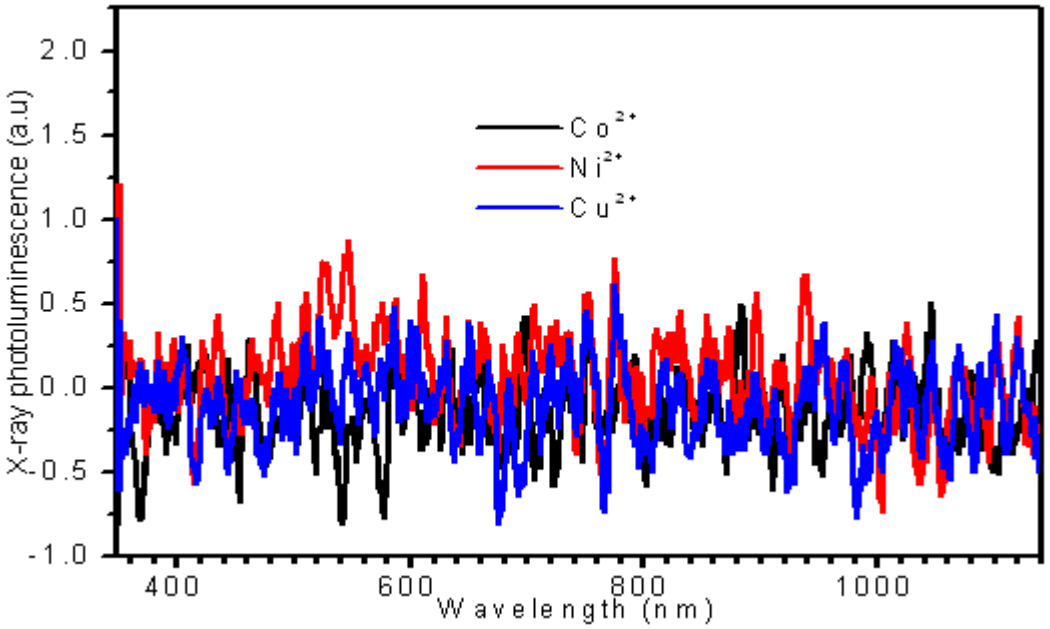

Figure 5.17 X-ray PL of Co^{2+},Ni^{2+},Cu^{2+} -doped $CaZnGe_2O_6$ (70%:50% ZnO)

5.4 Conclusions

Basically when we did the singly dopant survey studies using other dopants doped into the 70%:50% gram-weight bulk and nano ZnO optimized samples or 100% gram-weight bulk ZnO samples, we observed these 6 observations.

a) No change, the sample emits the usual blue emission under 254 nm illumination and retains its host green 538 nm emission under X-ray illumination.

b) Green emission and green afterglow due to dopant's luminescence centers as demonstrated by doping Tb_4O_7 (Chapter 3).

c) Green emission but with red afterglow in which energy transfer occurs from green photoluminescence effects onto Mn^{2+} luminescence centers in which red 670 nm afterglow is observed. This is only observed when the host material is made of 100% bulk ZnO and doped with Mn^{2+} and also 70%:50% phosphor samples doped with Tb^{3+} or Dy^{3+} with Mn^{2+}.

d) Strong red, white and blue emission but with faint afterglow due to host material in doped 70%:50% phosphor samples with dopants such as Sm^{3+}, Eu^{3+}, Dy^{3+} and Tm^{3+}.

e) Blue emission and blue afterglow due to contribution of electrons from dopant Ga^{3+}, In^{3+}, Lu^{3+} and Yb^{3+} and the hole traps they contributed when they occupied the cation vacancy sites within the host matrix. This phenomena is observed in 70%:50% phosphor samples and also for phosphor sample composed of 100% bulk ZnO doped with Ga^{3+}.

f) Dead zone in which there is none existent emission observable under both UVA 350 nm and 254 nm as demonstrated by Co^{2+}, Ni^{2+} and Cu^{2+}.

One very important conclusion is that the phosphorescence effects observed in this host $CaZnGe_2O_6$ material is actually due to physical lattice defects within the host material and not so much due to the rare earth dopant themselves with Tb^{3+} being the exception case.

The green 538 nm emission, the host emission, is believed due to combination of both bulk GeO_2 and ZnO material within the $CaZnGe_2O_6$ material. Bulk ZnO material is believed to be responsible for green photoluminescence effects while GeO_2 is believed to be responsible for host material's green afterglow effect. Dopant Mn^{2+} remains the most reactive and interesting among the manganese family in which it donates most of its optically active 3d orbital electrons onto the electron pool of the valence band. The same 3d orbital electrons are responsible for strong broad red 670 nm band afterglow observed. Other interesting visible light emissions observed are due to dopant Sm^{3+}, Eu^{3+}, Dy^{3+} and Tm^{3+} and they are accompanied with faint host material's afterglow. A few other unique dopants that contribute to interesting optical properties worth mentioning are Ga^{3+}, Cr^{3+}, Nd^{3+}, Yb^{3+} and Ho^{3+}. Dopants Ga^{3+} gives us the blue emission but no blue afterglow under UVA 350 nm illumination but it has blue emission and blue afterglow under 254 nm illumination. Dopant Cr^{3+}, Nd^{3+} and Yb^{3+} give us infra-red emission under X-ray irradiation and dopant Ho^{3+} shown us that its green luminescence centers (528 nm and 553 nm) could be more distinct over host green 538 nm luminescence centers under X-ray irradiation. Finally, dopant Sb^{3+} and Bi^{3+} with their UV luminescence centers has potential in making $CaZnGe_2O_6$ (70%:50% ZnO) ,an UV emitting phosphor.

CHAPTER 6

ENERGY TRANSFER, CO-DOPANT ISSUES AND OTHER PHOSPHORESCENCE MATERIALS

6.1 Introduction

In this chapter, we managed to conduct energy transfer studies based upon X-ray irradiation on two singly dopants to be doped into the 70%:50% gram-weight bulk and nano ZnO optimized host $CaZnGe_2O_6$ material. By doing this studies, we hope to reveal the energy transfer mechanism in between the dopants and the host material's green 538 nm luminescence centers or the migration of electrons from different luminescence centers.

6.2 Experimental details

The experiment parameters are as the same as in Chapter 4 but we decided to put in other two dopants into the optimized well trap structure made from 70%:50% gram-weight bulk and nano ZnO for our energy transfer studies. Each dopant concentration is kept at 0.16 mmole in consistent with dopant Tb_4O_7's concentration used in pinning down the 70%:50% optimized sample. The X-ray photoluminescence data are obtained at 60 kV, 5 mA after a standard reference sample is measured for set-up calibration. Mn^{2+} is chosen as the sensitizer because they are the most interesting and reactive dopant species among the manganese family.

6.3 Results and Discussions

6.3.1 Mn^{2+} and Sm^{3+}

Figure 6.1 shows us the X-ray photoluminescence comparison for all 3 samples, one doped with Mn^{2+}, another doped with Sm^{3+} and finally one that is doped with both Mn^{2+} and Sm^{3+}. The figure clearly showed that Mn^{2+} retains much of its energy or electrons and transfer some to boost Sm^{3+} red emission instead of giving them to the host material. In this case, a “Resonance” phase occurs or is defined when the activator dopant receives energy and increases its emission peaks which are in the same wavelengths as the sensitizer or donor’s red emission. Mn^{2+} acts as sensitizer with its 3d orbital electrons that are optically active and responsible for 670 nm red emission. As a result of the energy transfer between the sensitizer Mn^{2+} and activator Sm^{3+}, the host 538 nm green emission decreases.

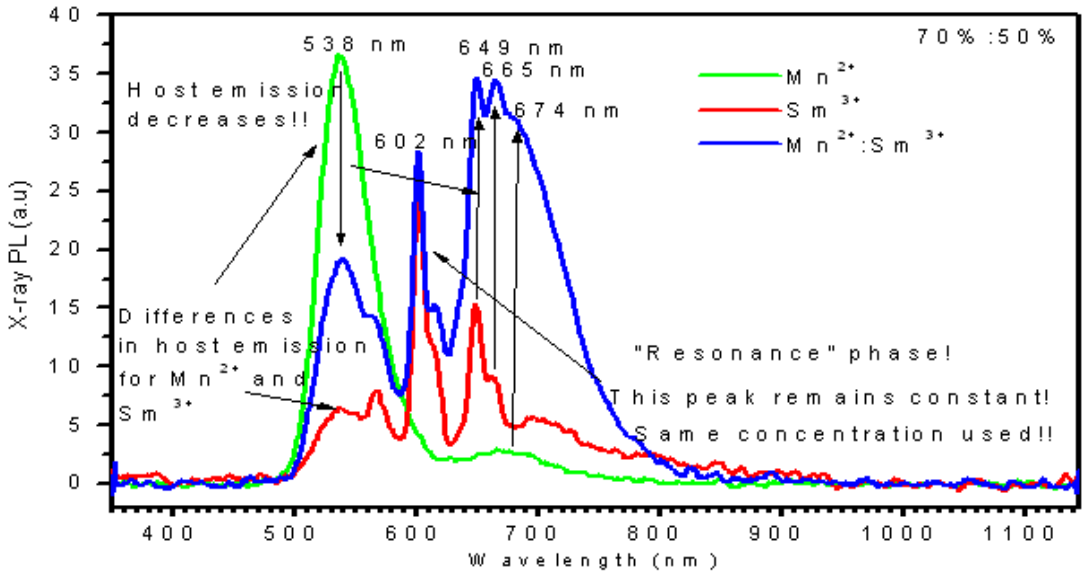

Figure 6.1 X-ray PL of $CaZnGe_2O_6$:Sm^{3+},Mn^{2+} (70%:50% ZnO)

6.3.2 Mn^{2+} and Ho^{3+}

Figure 6.2 shows us the X-ray photoluminescence comparison for all 3 samples, one doped with Mn^{2+}, another doped with Ho^{3+} and finally one that is doped with both Mn^{2+} and Ho^{3+}. The figure clearly showed an “Enhancement” phase occurrence. This phase is defined when the dopant receives energy and increases its emission peaks which are not in the same

wavelength as the donor's red emission. Under X-ray irradiation, the green Ho^{3+} emission of 528 nm and 548 nm seems to be more dominant or be the preferred pathway for the electrons than the host material luminescence centers that give green 538 nm emission. In this sample, some of Mn^{2+}'s 3d orbital electrons (red 670 nm) are retained and some are transferred to boost Ho^{3+} green emissions instead of donating them to the host material luminescence centers.

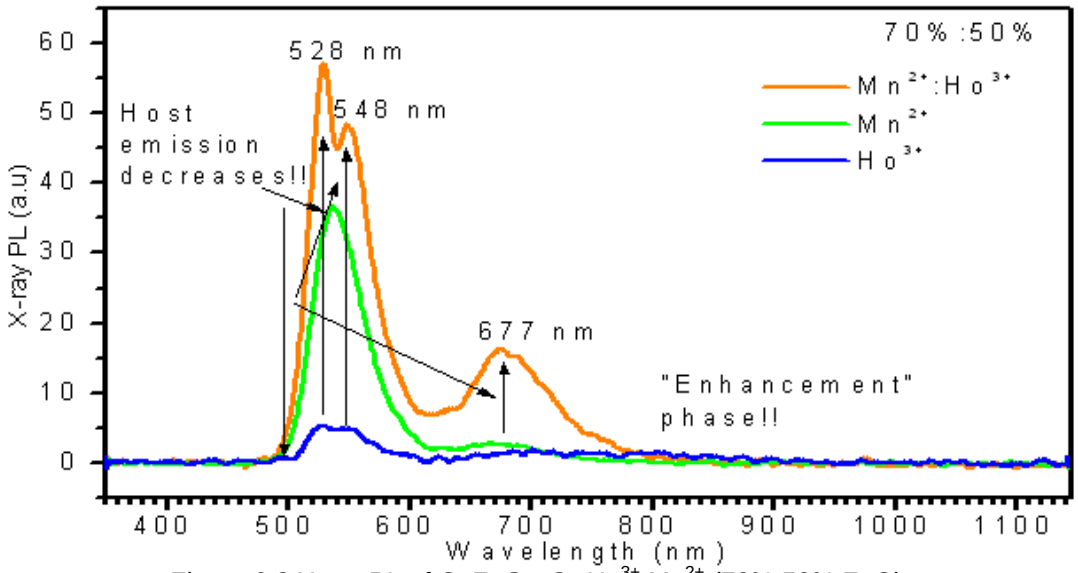

Figure 6.2 X-ray PL of $CaZnGe_2O_6$:Ho^{3+},Mn^{2+} (70%:50% ZnO)

6.3.3 Mn^{2+} and Nd^{3+}

Figure 6.3 shows us the X-ray photoluminescence comparison for all 3 samples, one doped with Mn^{2+}, another doped with Nd^{3+} and finally one that is doped with both Mn^{2+} and Nd^{3+}. The figure clearly showed an "Enhancement" phase occurrence. This "Enhancement" phase is unique since it involves boosting Nd^{3+} infra-red emissions. In this sample, Mn^{2+} red emission loses much of its energy, giving them to both host material and to boost Nd^{3+} infra-red emissions. Since the activator Nd^{3+} receives more electrons than the host material therefore the host green 538 nm decreases slightly.

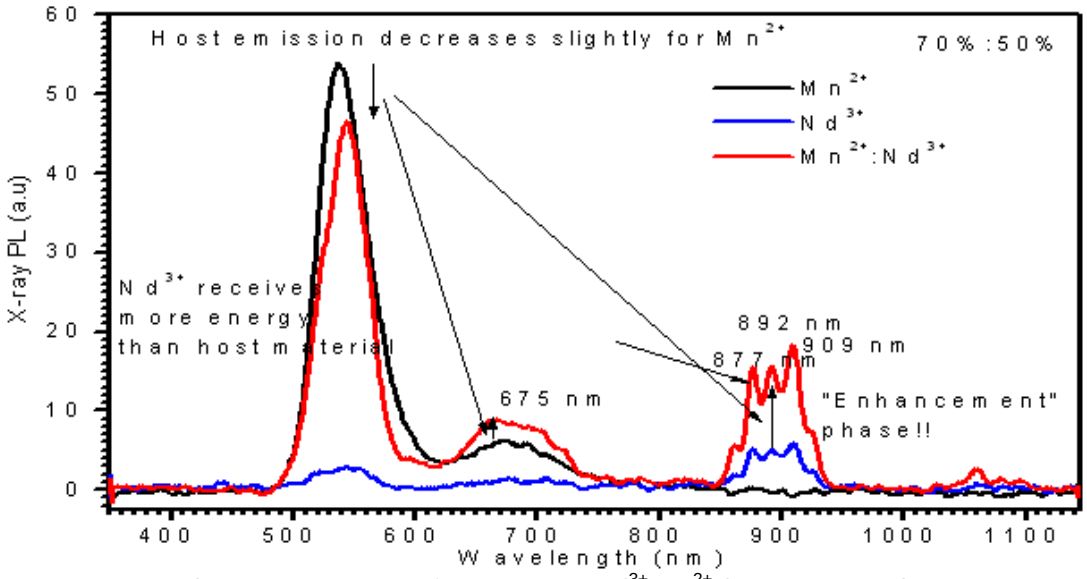

Figure 6.3 X-ray PL of $CaZnGe_2O_6$:Nd^{3+},Mn^{2+} (70%:50% ZnO)

6.3.4 Mn^{2+} and Dy^{3+}

Figure 6.4 shows us the X-ray photoluminescence comparison for all 3 samples, one doped with Mn^{2+}, another doped with Nd^{3+} and finally one that is doped with both Mn^{2+} and Nd^{3+}. In this sample, we are seeing a “Lockdown” phase occurrence. This phase occurs or is defined when the dopant loses energy and decreases its emission peaks. In this sample, the “Lockdown” phase happens to both the activator dopant and the host material. Much of Mn^{2+} red emission electrons are retained and little is given to host material, therefore the host green 538 nm decreases drastically. Some of Dy^{3+} 4f orbital electrons could be diverted to pair with Mn^{2+} 3d orbital electrons to form stable sub-shells, therefore decreasing Nd^{3+} 580 nm emission slightly.

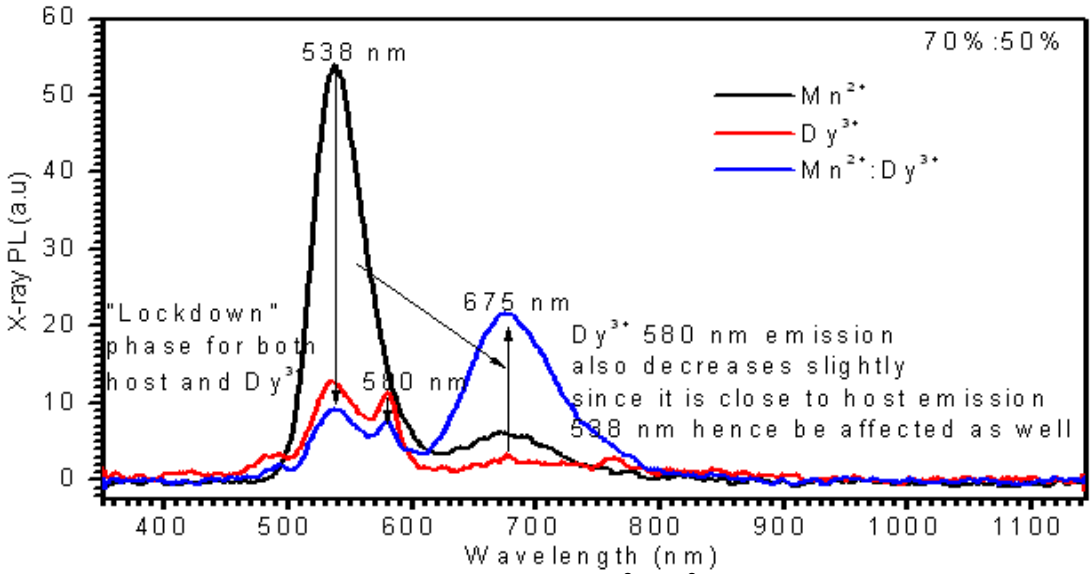

Figure 6.4 X-ray PL of $CaZnGe_2O_6:Dy^{3+},Mn^{2+}$ (70%:50% ZnO)

6.3.5 Mn^{2+} and Tb^{3+}

Figure 6.5 shows us the X-ray photoluminescence comparison for all 4 samples that involved dopant Tb_4O_7 and different manganese sensitizers like Mn^{2+}, Mn^{2+}/Mn^{3+} and Mn^{3+}. For the 3 doubly doped samples, there is a “Lockdown” phase occurrence for both Tb^{3+} and host material. Mn^{2+} has the most reactive electrons occupying 3d orbitals, retains its energy with little is given to host material hence the host green 538 nm is quenched and the the green Tb^{3+} 548 nm is dominant. Some of Tb^{3+}'s 4f orbital electrons may pair with Mn^{2+} 3d orbital electrons to form stable sub-shells therefore decreasing green Tb^{3+} 548 nm intensity. Mn^{2+}/Mn^{3+} contributes the least energy to host material and dopant terbium since it has almost none reactive electrons that contribute to red 670 nm emission to start with. Mn^{3+} contributes less energy (less than Mn^{2+} but more than Mn^{2+}/Mn^{3+}) since it has less electrons than Mn^{2+}, hence a lower red 670 nm emission intensity.

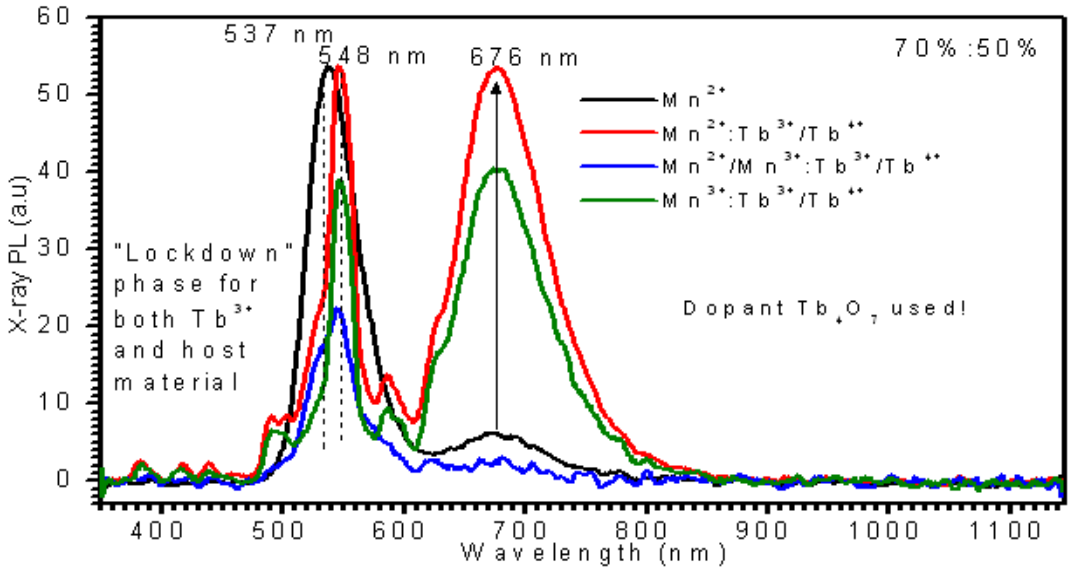

Figure 6.5 X-ray PL of $CaZnGe_2O_6:Tb^{3+},Mn^{2+}$ (70%:50% ZnO)

6.3.6 Mn^{2+} and Yb^{3+}

Figure 6.6 shows us the X-ray photoluminescence comparison for all 3 samples, one doped with Mn^{2+}, another doped with Yb^{3+} and finally one that is doped with both Mn^{2+} and Yb^{3+}. In this sample, a “Lockdown” phase occurrence happens for the dopant Yb^{3+} but not for the host material. The broad red 672 nm emission due to Mn^{2+} remains unchanged or with little changes, but still the host material luminescence centers receive more energy than dopant Yb^{3+}’s electrons responsible for infra-red emission. Some of Yb^{3+} 4f orbital electrons could be diverted to join with Mn^{2+}’s 3d orbital electrons to be avalanched onto host material, therefore decreasing Yb^{3+}’s infra-red emission.

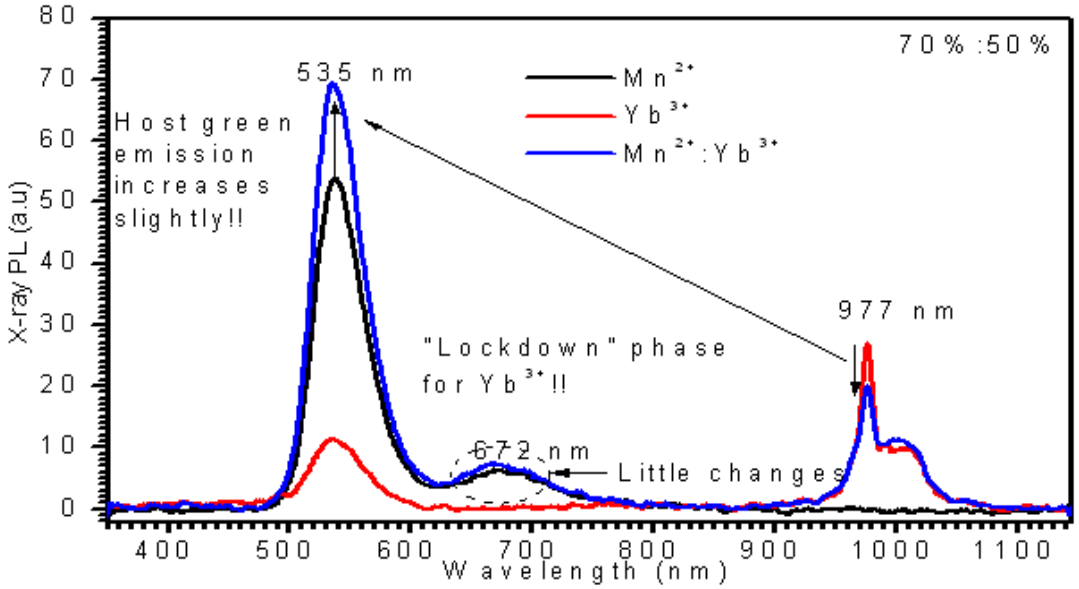

Figure 6.6 X-ray PL of $CaZnGe_2O_6:Yb^{3+},Mn^{2+}$ (70%:50% ZnO)

6.3.7 Mn^{2+} and Ga^{3+}

Figure 6.7 shows us the X-ray photoluminescence comparison for all 3 samples, one doped with Mn^{2+}, another with Ga^{3+} (62 pm) and finally one that is doped with Mn^{2+} and Ga^{3+}. The presence of dopant Ga^{3+} (within host matrix and close proximity to both bulk and nano ZnO) has induced the host material luminescence centers to blue-shifted. This is because Ga^{3+} 3d orbital has to spread and extend in order to enhance the nano ZnO species's X-ray energies absorbing property. This induction caused the host green 538 nm emission to be reduced, hence a broad blue emission band (due to nano ZnO's luminescence centers) is found with sample that is singly doped with Ga^{3+}. By doping both Ga^{3+} and Mn^{2+} together, the sensitizer Mn^{2+} retains much of its red emission 672 nm electrons, donating some to host material and through pairing with Ga^{3+}'s 3d electrons causes Ga^{3+}'s support of host blue emission electrons (nano ZnO within host matrix) ceases. Therefore we observe the normal host green 538 nm emission and the disappearance of the host broad blue emission. A "Lockdown" phase occurrence has happened to the host blue emission luminescence centers.

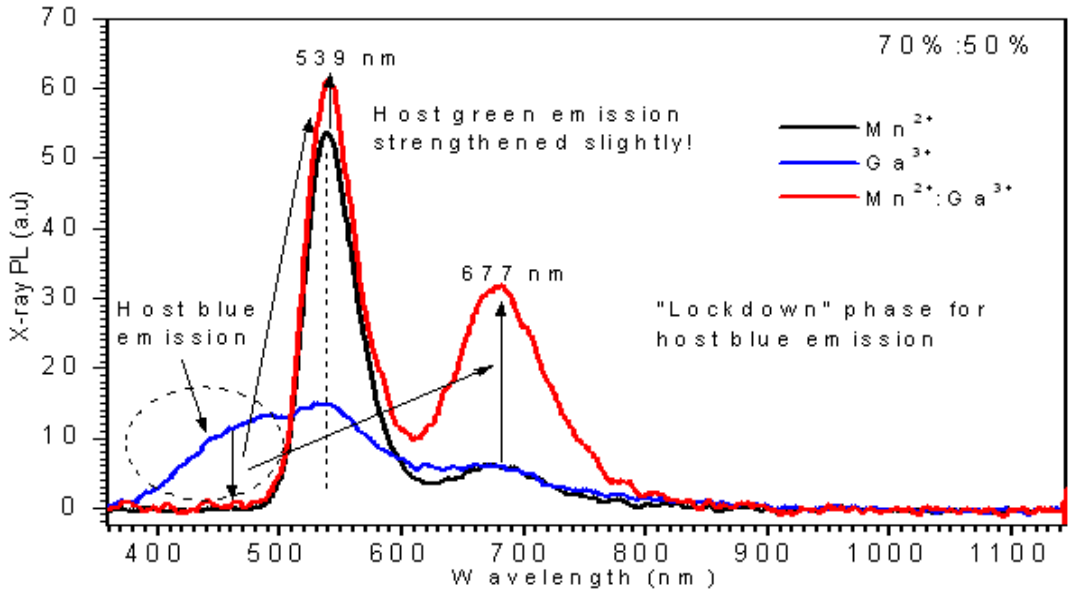

Figure 6.7 X-ray PL of $CaZnGe_2O_6$:Ga^{3+},Mn^{2+} (70%:50% ZnO)

6.3.8 Mn^{2+} and Pr^{3+}

Figure 6.8 shows us the X-ray photoluminescence comparison for all 3 samples, one doped with Mn^{2+}, another with Pr^{3+} and finally one that is doped with Mn^{2+} and Pr^{3+}. Dopant Pr^{3+} exhibits no optically interesting electrons in visible and infra-red wavelengths. Once co-doped with Mn^{2+}, the optically inert status remains unchanged. The sensitizer Mn^{2+} transfers most of its red emission electrons to host material and to fill up Pr^{3+} 4f sub-shells which are non-optically active. In the co-doped sample, we can say Pr^{3+} uses it 4f orbital space as electron traps and a “Lockdown” phase occurred for the host material. Another possibility is to increase the crystal field strength by doping Pr^{3+} into $CaZnGe_2O_6$ with (70%:108% ZnO, more nano ZnO added), this way, the dopant Pr^{3+} will feel tightly squeezed and its multiplets can be better resolved, thus enabling us to study Pr^{3+}’s blue, green and red emission or white emission..

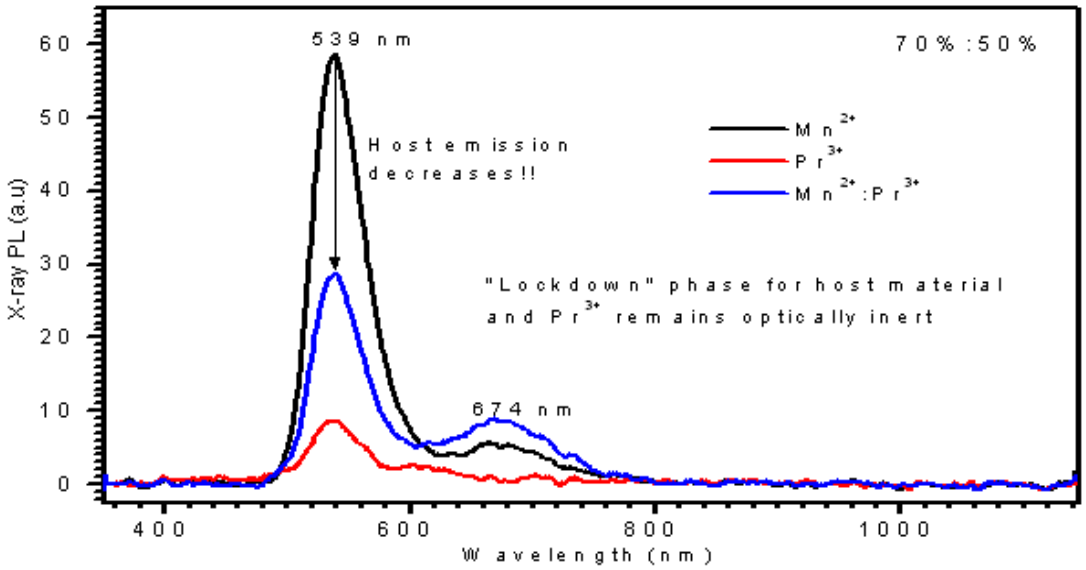

Figure 6.8 X-ray PL of $CaZnGe_2O_6:Pr^{3+},Mn^{2+}$ (70%:50% ZnO)

6.3.9 Mn^{2+} and Eu^{3+}

Figure 6.9 shows us the X-ray PL of 70%:50% samples doped with Mn^{2+} and Eu^{3+}. Due to highly protective 4f shells of Eu^{3+}, we noticed there is only slight enhancement found in 589 nm emission of Eu^{3+}. This is believed due to some energy transfer happenings from Mn^{2+} to Eu^{3+}. The emission 612 nm exhibits no changes, this meant that the energy transfer occurred between Mn^{2+} and Eu^{3+} dopants in highly symmetric sites or well trap sites.

6.3.10 Mn^{2+} and Cr^{3+}

Figure 6.10 shows us the X-ray PL of 70%:50% samples doped with Mn^{2+} and Cr^{3+}. The figure clearly shown that the infra-red emission decreases when co-doped with Mn^{2+}. This led us to believe that when Mn^{2+} and Cr^{3+} with their 3d electron shells are put near together, their orbital electrons overlap each other and strengthened each other, thus leaving less electrons involve in Cr^{3+}'s transition that emits infra-red 841 nm. A self-quenching mode has occurred for this case.

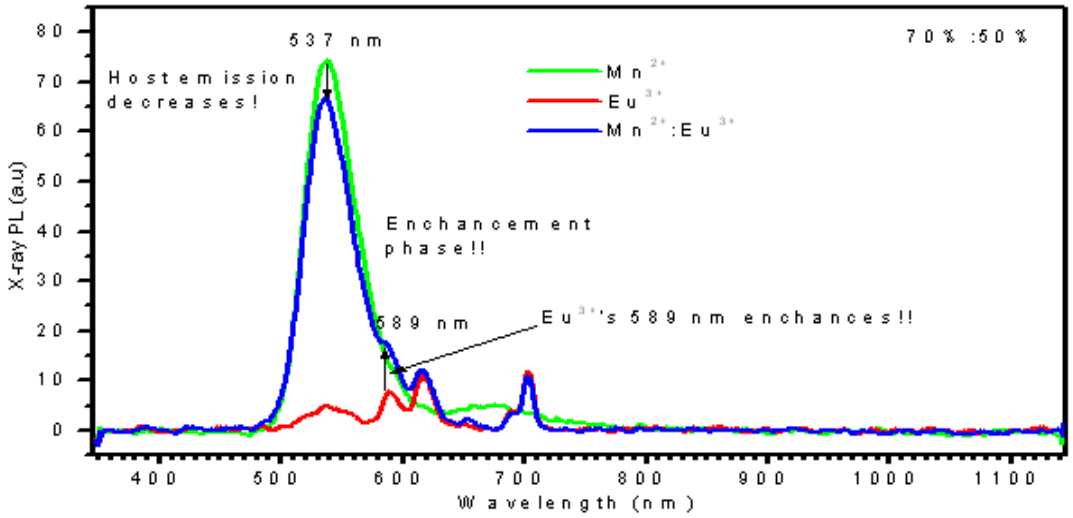

Figure 6.9 X-ray PL of $CaZnGe_2O_6:Eu^{3+},Mn^{2+}$ (70%:50% ZnO)

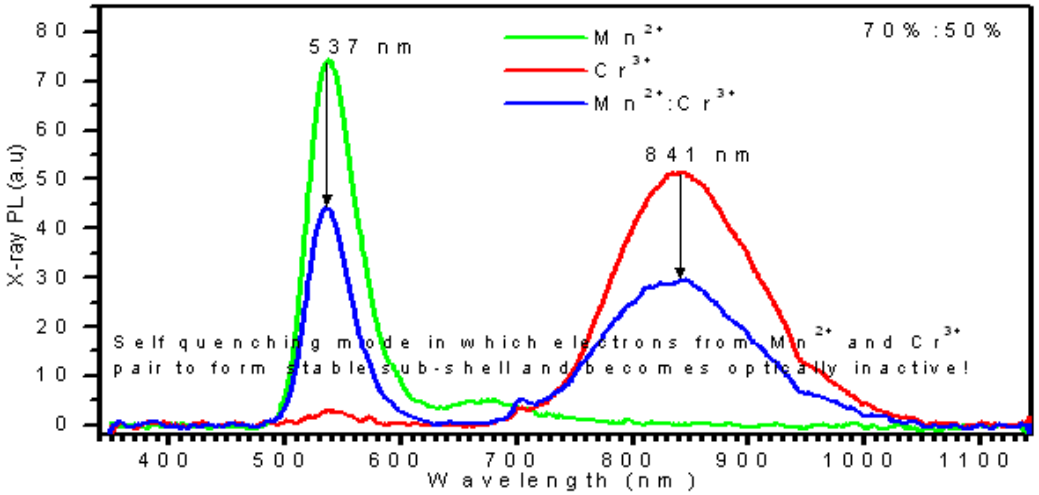

Figure 6.10 X-ray PL of $CaZnGe_2O_6:Cr^{3+},Mn^{2+}$ (70%:50% ZnO)

6.4 Other phosphorescence samples

For this section, we fabricated the well known long blue afterglow samples $CaAl_2O_4:Eu^{2+},Nd^{3+}$ and long green afterglow $SrAl_2O_4:Eu^{2+},Dy^{3+}$ for our studies. We decided to put in a small amount of organic coated luminescence ZnO nanopowder to determine what influences these nanoparticles have on the final afterglow phosphor samples.

6.4.1 $CaAl_2O_4:Eu^{2+},Nd^{3+}$

Figure 6.11 shows us the changes that took place when we doped the $CaAl_2O_4:Eu^{2+},Nd^{3+}$ phosphor with ZnO nanoparticles. The blue 444 nm emission due to Eu^{2+} luminescence centers decreased when co-doped with Nd^{3+}. Then as more and more ZnO nanoparticles are doped into the phosphor samples, the blue 444 nm decreases further until it is almost disappears and then finally, the blue emission emerges red-shifted to 473 nm, which we believed is due to ZnO nanoparticles as luminescence centers. A phosphor sample, $CaAl_2O_4:Eu^{2+},Dy^{3+}$ doped with ZnO nanoparticles was made for comparison too and it bears similar resemblances to the $CaAl_2O_4:Eu^{2+},Nd^{3+}$ doped with ZnO nanoparticles. Figure 6.12 shows us the optical properties of the same phosphor samples under mercury lamp 254 nm. The figure clearly shown that the presence of ZnO nanoparticles tend to bring out the red Eu^{3+}'s emission of 593 nm and 613 nm, while the co-dopant Nd^{3+} tends to bring out the blue 444 nm strongly and decreases the red Eu^{3+} emission. Figure 6.13 clearly shown that by doping the ZnO nanoparticles, the afterglow property of the phosphor has been diminished instead of improving them.

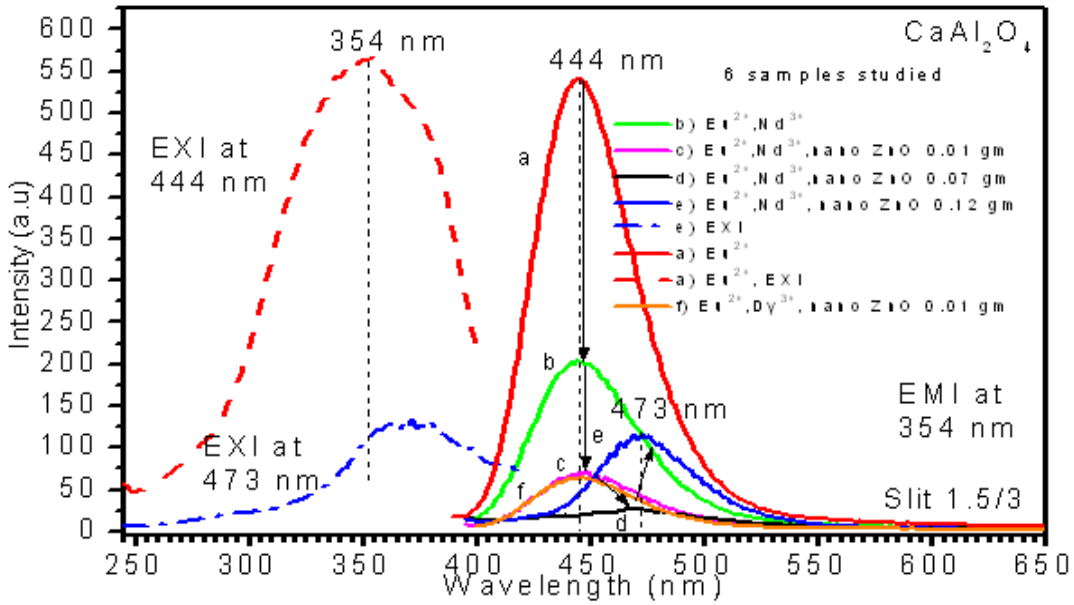

Figure 6.11 Excitation and Emission spectras of $CaAl_2O_4:Eu^{2+},Nd^{3+}$ doped with nano ZnO

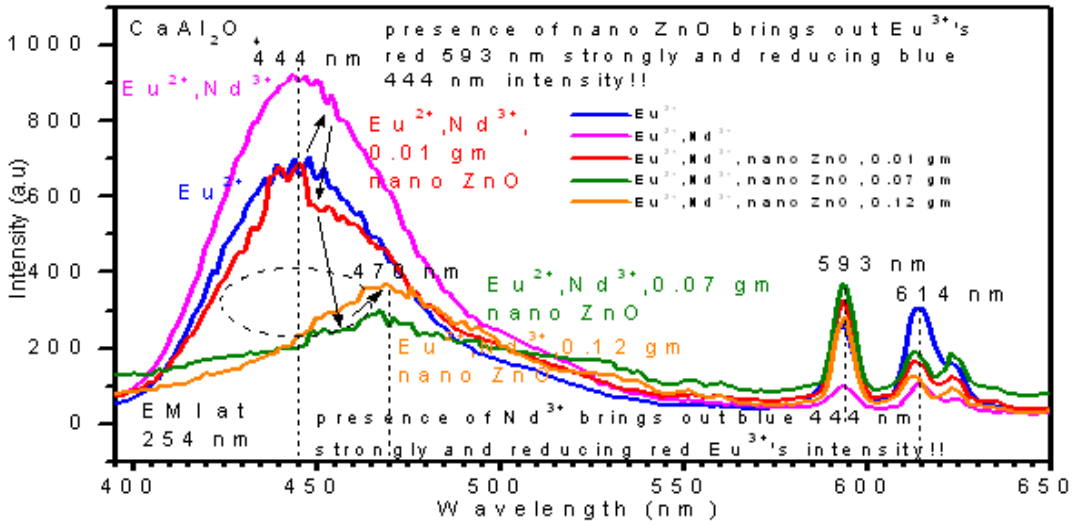

Figure 6.12 Emission spectras of $CaAl_2O_4:Eu^{2+},Nd^{3+}$ doped with nano ZnO at 254 nm

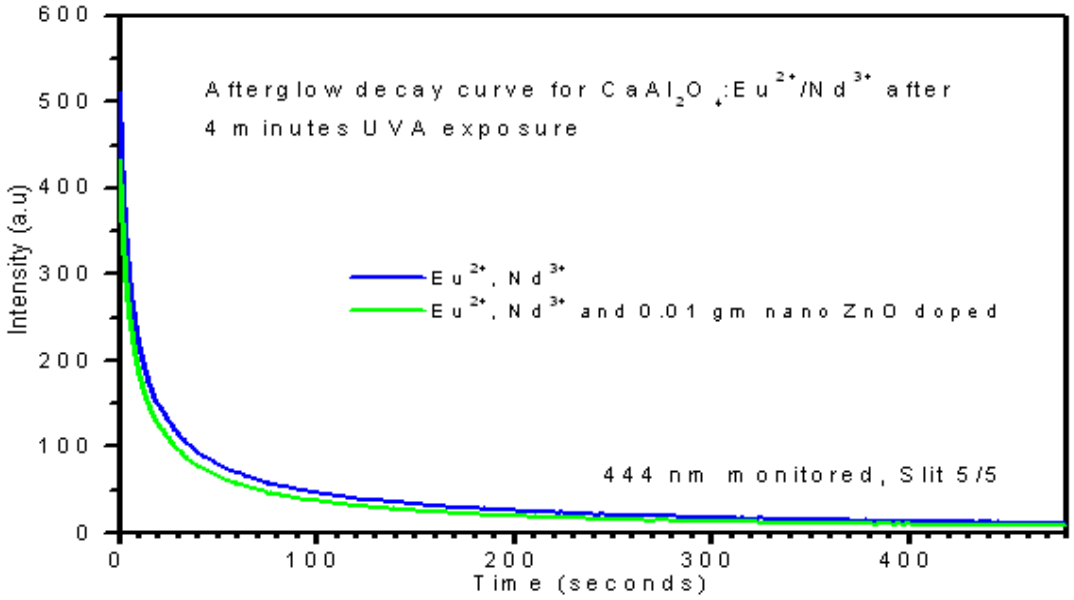

Figure 6.13 Afterglow decay curve of $CaAl_2O_4:Eu^{2+},Nd^{3+}$ doped with nano ZnO

6.4.2 $SrAl_2O_4:Eu^{2+},Dy^{3+}$

Figure 6.14 shows us the optical properties of $SrAl_2O_4:Eu^{2+}:Dy^{3+}$ doped with organic coated luminescence ZnO nanopowder. As expected, the green emission 515 nm from Eu^{2+} decreases when co-doped with Dy^{3+}. By adding a mere 0.02 gm of ZnO nanoparticles, the green emission 515 nm is found to be enchanced. More additional of ZnO nanoparticles caused the green emission to be quenched and then blue-shifted to 470 nm emission which is believed due to ZnO nanoparticles as dominant luminescence centers instead of Eu^{2+}. Figure 6.15 shows us that by adding small amount of the ZnO nanoparticles, we could improved and prolonged the green afterglow of $SrAl_2O_4:Eu^{2+}:Dy^{3+}$ long afterglow phosphor. This findings shown that by adding the ZnO nanoparticles, additional electrons trap were formed in the host $SrAl_2O_4:Eu^{2+},Dy^{3+}$ phosphor but not in the host $CaAl_2O_4:Eu^{2+},Nd^{3+}$ phosphor.

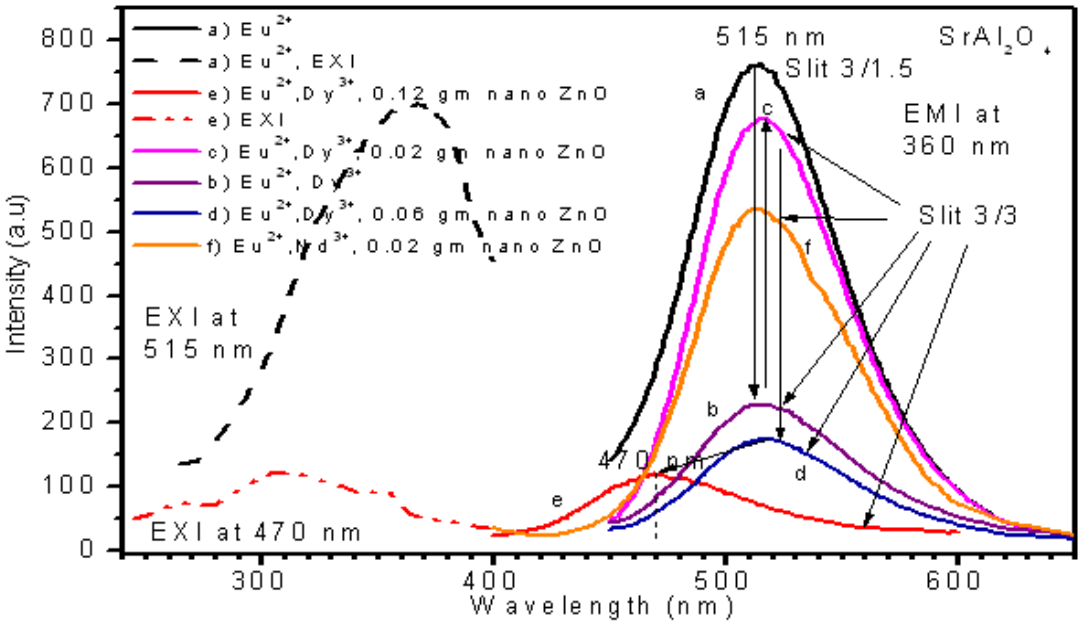

Figure 6.14 Excitation and Emission spectras of $SrAl_2O_4:Eu^{2+},Dy^{3+}$ doped with nano ZnO

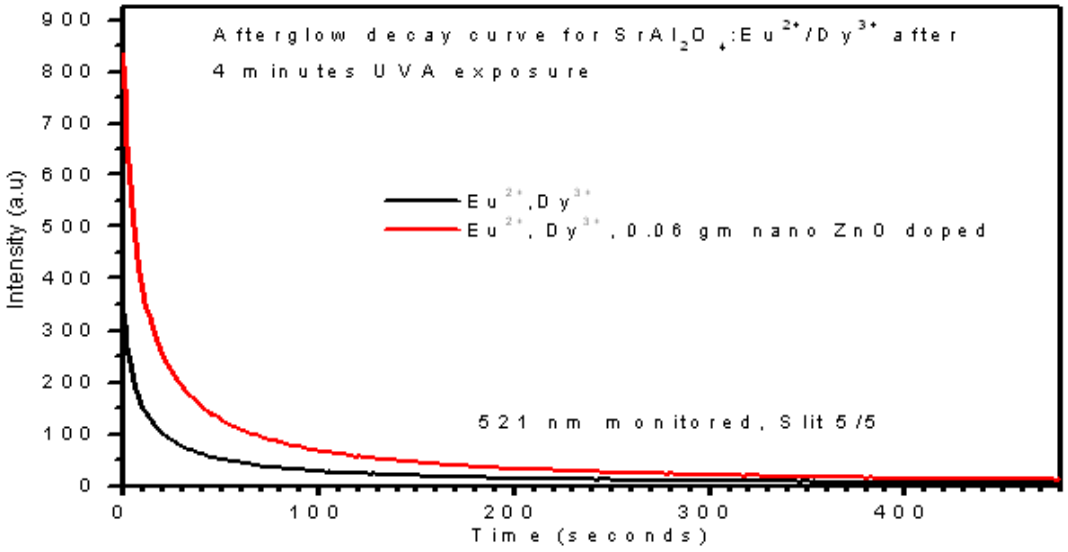

Figure 6.15 Afterglow decay curve of $SrAl_2O_4:Eu^{2+},Dy^{3+}$ doped with nano ZnO

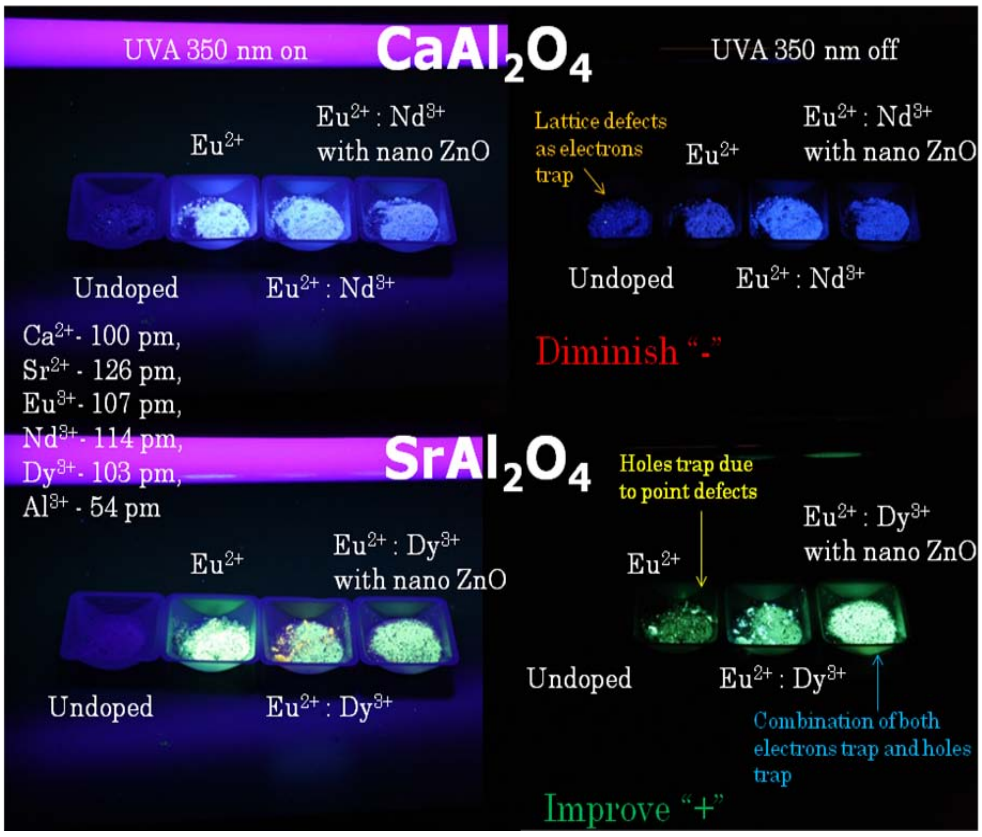

Figure 6.16 $CaAl_2O_4$ and $SrAl_2O_4$ long afterglow phosphors

Figure 6.16 best summed the effect of nano ZnO to both $CaAl_2O_4$ and $SrAl_2O_4$ long afterglow phosphors. Due to the presence of nano ZnO that repairs the internal lattice defects of $CaAl_2O_4$ phosphor, this causes the reduction of electrons trap density, hence the persistent luminescence property of this phosphor is diminished. As for $SrAl_2O_4$ phosphor, the presence of nano ZnO induced the formation of well-formed and structured internal lattice defects that act as electrons trap, hence the combination of both electrons trap and holes trap (induced by Eu^{3+} dopants occupying Sr^{2+} cation vacancy sites within the host matrix or point defects) improved the persistent luminescence property of this phosphor.

6.5 Conclusions

By co-doping various rare earth dopants with sensitizer Mn^{2+} and under X-ray photoluminescence studies, we found the followings:

a) Bulk ZnO material is to responsible for host green 538 nm emission observed as X-ray photoluminescence.

b) Mn^{2+} has the best and the most interesting X-ray energies absorption properties among the manganese family, in which it enables its luminescence centers, $^4T_1$-$^6A_1$,to give off the broad red emission band around 670 nm.

c) Positive energy transfer were seen, in which the rare-earth dopant's emission was enhanced in Sm^{3+}, Ho^{3+}, Nd^{3+} and Eu^{3+} when co-doped with Mn^{2+}.

d) Negative energy transfer were seen, in which the rare-earth dopant's emission was quenched in Yb^{3+}, Dy^{3+}, Tb^{3+}, Ga^{3+} and Cr^{3+} when co-doped with Mn^{2+}. Only Pr^{3+} which have non-optically active electrons under X-ray irradiation, remains so even when co-doped with Mn^{2+}.

e) High experimental limit for X-ray PL studies of this $CaZnGe_2O_6$ (70%:50% ZnO) phosphor material is the host green emission around 535 nm with the exception of sample doped with Ga^{3+} (70%:50% ZnO) in which the host green emission is broadly blue-shifted.

CHAPTER 7

FINAL REMARKS AND FUTURE WORK

In this thesis, we have investigated the roles of ZnO nanoparticles in improving the long persistent luminescence of $CaZnGe_2O_6$ phosphor. We carried out the host phosphor material optimization and concluded that structure lattice defects play an important role in influencing phosphorescence effects. We also established the crucial relationship in between photoluminescence and phosphorescence effects with the physical host lattice structure of the phosphor material.

From our X-ray photoluminescence studies with co-dopant Mn^{2+}, we observed some interesting energy transfer phenomena that took place. From the singly dopant studies in the much improved host phosphor material, we discovered that this newly improved $CaZnGe_2O_6$ phosphor has the potential in giving us

a) Blue, red and green afterglow phosphors.
b) White LED phosphor by utilizing the near UV-blue LED chips and dopants such as Sm^{3+}, Eu^{3+}, Tb^{3+}, Dy^{3+} and Tm^{3+}.
c) Tunable laser materials by utilizing the infra-red emission from Cr^{3+}, Nd^{3+} and Yb^{3+}.
d) UV emission phosphors (Sb^{3+} and Bi^{3+}).
e) A possibility as a Pr^{3+} doped quantum splitting phosphor by utilizing the vacuum ultraviolet wavelength as excitation source.

Future work shall be to probe deeply the co-dopant issues from the dopant concentration point of view, the investigations of bulk CaO and GeO_2 material roles on this phosphor's optical properties, the possibility of investigating ZnO:Zn phosphor material in determining its photon emission mechanism and also the possibility of designing $SrZnAl_2O_5$ phosphor material using bulk ZnO and ZnO nanoparticles.

My study of $CaZnGe_2O_6$ long afterglow phosphor by utilizing ZnO nanoparticles has been an enlightening experience. We shed new lights, new knowledge and new understanding in phosphorescence phenomena from the host phosphor material point of view. We explored the delicate relation in between the host phosphor luminescence centers and the dopants themselves under UV and X-ray illuminations. We hope our discoveries and contributions will help to advance mankind's efforts in designing future phosphor materials with superior and far better light emission's efficiency. This $CaZnGe_2O_6$ (70%:50% ZnO) has been a 21^{st} century phosphor, the first of its unique kinds. One $CaZnGe_2O_6$ phosphor down and at least a couple hundreds more to go.

APPENDIX A

LIST OF PUBLICATIONS

LIST OF PUBLICATIONS

1. *Boon Kuan Woo*, Wei Chen, Alan G. Joly and R. Sammynaiken, J. Phys. Chem. C 2008, 112, 14292–14296.
2. *Boon Kuan Woo*, Alan G. Joly, Wei Chen, Journal of Luminescence 131 (2011) 49–53.
3. *Boon Kuan Woo*, Zhiping Luo, Yang Li, Surinder P. Singh, Alan G. Joly, Marius Hossu, Wei Chen, Optical Materials, (Submitted on late 2010).
4. Jiaguang Han, *Boon Kuan Woo*, Wei Chen, Mei Sang, Xinchao Lu, Weili Zhang, J. Phys. Chem. C 2008, 112, 17512-17516.
5. Wang Ming-Wei, *Boon Kuan Woo*, Han Jia-Guang, Chen Wei, Zhang Weili, Optoelectronics Letters, Vol. 5, No. 6, November 2009.
6. Yuanfang Liu, Wei Chen, Shaopeng Wang, Alan G. Joly, Sarah Westcott, and *Boon Kuan Woo*, J. Appl. Phys. 2008, 103 (6): 063105 1-7
7. R. Schachar, Wei Chen, *B. K. Woo*, B. Pierscione, X. Zhang, L. Ma, Nanotechnology, 2008, 19, 2510

REFERENCES

1. Adrian Kittai, “Luminescent Materials and Applications”, Wiley series (2008).
2. P. E. A. Lenard, F. Schmidt and R. Tomaschek, “Handbuch der Experimentalphysik”, Vol.23 Akademie Verlagsgesellschaft, Leipzig (1928).
3. B. Gudden and R.W. Pohl, "Lichtelektrische Beobachtungen an Zinksulfiden," Zeitschrift fηr Physik, vol. 2 (1930), 181-191.
4. W. Hoogenstraaten, H. A. Klasens, “Some properties of zinc sulfide activated with copper and cobalt, J. Electrochem. Soc. (1953), 100, 366-375.
5. T. Matsuzawa, Y. Aoki, N. Takeuchi, Y. Murayama, J. Electrochem. Soc. 143, 2670 (1996).
6. V. Abbruscato, J. Electrochem. Soc. 118, 930 (1971).
7. W. Jia, H. Yuan, L. Lu, h. Liu, W. M. Yen, J. Cryst. Grow. 200, 179 (1999).
8. H. Yamamoto and T. Matsuzawa, J. Lumines. 72-74, 287 (1997).
9. W. M. Yen, S. Shionoya, H. Yamamoto, Phosphor Handbook, 2nd edition, CRC Press/Taylor and Francis, FL, USA, (2007).
10. W. M. Yen, “Inorganic Phosphors: Compositions, Preparation and Optical Properties”. CRC Press, New York, (2004.
11. W. Lehmann, “Inorganic Phosphors: Compositions, Preparation and Optical Properties”, CRC Press, Boca Raton, FL, (2004).
12. H. Ji, G. Xie, Y. Lv, H. Lu, J. Sol-Gel Sci. Technol., 44, 133-137, (2007).
13. W. Pan, G. Ning, X. Zhang, J. Wang, Y. Lin, J. Ye, J. Lumines. 128, 1975-1979, (2008).

14. F. Song, C. Donghua, Y. Yuan, J. Alloy. Compd. 458, 564-568, (2008).
15. Y. Xu, D. Chen, Ceram. Int. 34, 2117-2120, (2008).
16. W. Rui-Ping, J. Zheng-Hua, M. Jing-Xin, Z. Dong, Z. Zhi-Peng, L. Wei-Sheng, J. Alloy. Compd. 486 (2009) L17–L20.
17. G. Yu, W. Yuhua, L. Yanqin, X. Xuhui, J. Electrochem. Soc. 157, 6, (2010).
18. C. Chengkang, Y. Zhaoxin, M. Dali, J. Alloy. Compd. 415 (2006) 220–224.
19. H. Tao, L. Qun, M. Dali, C. Chengkang, Mat. Chem. Phys. 107 (2008) 142–147.
20. H. Ping, C. Cai-E, W. Seng, Opt. Mater. 32 (2009) 184–189.
21. S.R. Lukic, D. M. Petrovic, M. D. Dramicanin, M. Mitric, Lj. Dacanin, Scrip. Mater. 58 (2008) 655–658.
22. P. Tianyou, L. Huajun, Y. Huanping, Y. Chunhua, Mater. Chem. Phys. 85 (2004) 68–72.
23. T. Aitasalo, J. Holsa, H. Jungner, M. Lastusaari, J. Niittykoski, J. Physc. Chem. B, 110, 4589-4598, (2006).
24. F. Clabau, X. Rocquefelte, S. Jobic, P. Deniard, M. H. Whangbo, A. Garcia, T. Le Mercier, Chem. Mater. 18, 3212-3220, (2005).
25. P. Dorenbos, J. Electrochem. Soc. 152, H107-H110, (2005).
26. Y. Zhao-Xin, C. Cheng Kang, M. Da-Li, Y. Weijiang, J. Alloy Compd. 377 (2004) 268–271.
27. N. Suriyamurthy, B.S. Panigrahi, J. Lumines. 128 (2008) 1809– 1814.
28. H. Luitel, W. Takanori, T. Toshio, Y. Mitsunori, Res. Lett. Mat. Sci. 475074, 4, (2009).
29. Y. Lin, N. Ce-Wen, Z. Xisong, W. Junbo, W. Haifeng, C. Depu, X. Shengming, Mat. Chem. Phys. 82 (2003) 860–863.

30. F. Qin, C. Chengkang, M. Dali, J. Alloy. Compd. 390 (2005) 133–137.
31. D. Jia, W. Jia, Y. Jia, J. App. Phys 101, 023520, (2007).
32. F. Hirotoshi, J. Holsa, T. Laamenen, M. Lastusaari, J. Niittykoski, Y. Okajima, A. Yamamoto, J. Lumines. 128 (2008) 881–884.
33. L. Yuanhua, Z. Zhongtai, T. Zhilong, Z. Junying, Z. Zishan, L. Xiao, Mat. Chem. Phys. 70 (2001) 156–159.
34. T. Aitasalo, P. Deren, J. Holsa, H. Jungner, J. C. Krupa, M. Lastusaari, J. Legendziewicz, J. Niittykoski, W. Strek, J. Solid State Chem. 171 (2003) 114–122.
35. C. Guo, Q. Tang, C. Zhang, D. Huang, Q. Su, J. Lumines. 126 (2007) 333–338.
36. Z. Jun-Cheng, W. Xusheng, Y. Xi, J. Alloy. Compd., (2010).
37. Ü. Özgür,a_ Ya. I. Alivov, C. Liu, A. Teke,b_ M. A. Reshchikov, S. Doğan,c_ V. Avrutin, S. J Cho, H. Morkoc, J. App. Phys 98, 041301, (2005).
38. C. Klingshirn, ChemPhysChem 2007, 8, 782 – 803.
39. K. Senthilkumar, O. Senthilkumar, K. Yamauchi, M. Sato, S. Morito, T. Ohba, M. Nakamura, Y. Fujita, Phys. Status Solidi B 246, No. 4, 885–888 (2009).
40. H. M. Xiong, Y. Xu, Q. G. Ren, Y. Y. Xia, J. Am. Chem. Soc. (2008), 130, 7522-7523.
41. Z. L. Wang, “Nanostructures of zinc oxide”, Materials Today, June (2004).
42. K. F. Lin, H. M. Chen, H. C. Hsu, L. J. Lin, W. F. Hsieh, Chem. Phy. Lett. 409 (2005) 208–211.
43. A. B. Djurisic, Y. H. Leung, small (2006), 2, No. 8-9, 944 – 961.
44. H. Zhou, H. Alves, D. M. Hofmann, W. Kriegseis, B. K. Meyer, Appl. Phys. Lett., Vol. 80, No. 2, 14 January (2002).
45. T. Hirai, Y. Asada, Journal of Colloid and Interface Science 284 (2005) 184–189.
46. M. Iwasaki, Y. Inubushi, S. Ito, J. Mater. Sci. Lett., 16 (1997), 1503-1505.
47. Y. Inubushi, R. Takami, M. Iwasaki, H. Tada, S. Ito, J. Coll. Int. Sci., 200, 220-227

(1998).

48. S. Rakshit, S. Vasudevan, ACS Nano, Vol 2, No. 7, 1473-1479 (2008).
49. H. L. Cao, X. F. Qian, Q. Gong, W. M. Du, X. D. Ma, Z. K. Zhu, Nanotechnology 17, 3632-3636, (2006).
50. G. R. Gattorno, P. S. Jacinto, L. R. Vazquez, J. Nemuth, I. Dekany, D. Diaz, J. Phys. Chem. B, 107, 12597-12604, (2003).
51. J.A. Nelson, E.L. Brant, M.J. Wagner, Chem. Mater. 15 (2003) 688–693.
52. Z.M. Qi, C.S. Shi,W.W. Zhang,W.P. Zhang, T.D. Hu, Appl. Phys. Lett. 81 (2002) 2857–2859.
53. K. Lebbou, P. Perriat, O. Tillement, J. Nanosci. Nanotechnol. 5 (2005) 1448–1454.
54. Y.C. Kang, H.S. Roh, S. Bin Park, Adv. Mater. 12 (2000) 451.
55. Y.Q. Zhai, Z.H. Yao, M.D. Qiu, B.S. Liu, X.L. Dai, Indian J. Chem., Sect. A. 43 (2004) 71.
56. L. Xu, B. Wei, W. An, Z. Lu, H. Gao, Y. Zhang, Z. Zhang, J. Alloys Compd. 460 (2008) 524.
57. Y. Iwaka, Y. Akimoto, M. Omiya, T. Ueda, T. Yokomori, J. of Lumines. 130 (2010) 1470–1474.

BIOGRAPHICAL INFORMATION

Originally hailed from Malaysia, the author receives his early tertiary education at University of Malaya, graduated with a Bachelor of Science degree in Physics. Before leaving to pursue graduate study in United States, he obtained a Master of Science degree at the same institution, in which he did some work related to astronomical image processing. While at University of Oklahoma, Norman, the author received the vigorous physics graduate level courses and completed his Master degree in Physics through non-thesis route before coming to University of Texas at Arlington to pursue his doctoral study. The author wishes to embark on a career either in teaching or carve a career in the industry or become a businessman upon his return to his home country once his PhD study has been completed.

The author likes movies, watching TVs, electronic games, euro-board gaming, listening to 103.7 lite FM, badminton and Tichu cardgame as his favorite activities to spend on his leisure time.